RICE UNIVERSITY

Hydrogen doping and the metal-insulator phase transition in vanadium dioxide

by

Heng Ji

A THESIS SUBMITTED
IN PARTIAL FULFILLMENT OF THE
REQUIREMENTS FOR THE DEGREE

Doctor of Philosophy

APPROVED, THESIS COMMITTEE

Douglas Natelson, Chair
Professor of Physics and Astronomy

Rui-rui Du
Professor of Physics and Astronomy

Sibani Lisa Biswal
Associate Professor of Chemical and
Biomolecular Engineering

HOUSTON, TEXAS
April 2015

ABSTRACT

Hydrogen doping and the metal-insulator phase transition in vanadium dioxide

by

Heng Ji

Strongly correlated systems represent a major topic of study in condensed matter physics. Vanadium dioxide, a strongly correlated material, has a sharp metal-to-insulator phase transition at around 340K (67 °C), a moderate temperature which can be easily achieved. Its potential as a functional material in optical switches and semiconductor applications has attracted a great deal of attention in recent years. In this thesis, after a detailed introduction of this material and the methods we used to grow VO_2 in our lab (Chapter 1), I will discuss our attempts to modulate the electronic properties and phase transition of single-crystal VO2 samples. It started with a plan to use ionic liquid to apply an electrostatic gate to this material. Although modulation of the resistance was observed, we also discovered an unexpected electrochemical reaction, leading to a suspicion that hydrogen doping is the reason for the change of properties of VO_2 (Chapter 2). Next, a series of experiments were performed to systematically study the mechanism of this hydrogen doping process and to characterize the hydrogenated VO_2. Our collaborators also provided supporting simulation results to interpret these phenomena from a theoretical point of view, as well as results from synchrotron x-ray diffraction and neutron diffraction experiments. From all these studies, we

confirmed the existence of the hydrogen intercalation in VO_2 (Chapter 3), and further, plotted the phase diagram as a function of temperature and hydrogen concentration (Chapter 5). We also found that this diffusion process prefers the rutile crystal structure of VO_2 (i.e. metallic phase) and specifically, its c-axis (Chapter 4). Finally, the low-temperature electric transport properties of the hydrogenated VO2 material have been studied for the first time, and interesting magneto-resistance responses will be discussed (chapter 6).

Acknowledgments

Finishing a doctoral dissertation and getting a PhD degree is never a one-man job. To reach this point of my life, I have to thank many people for their help and support throughout my past 6 years at Rice University, and, of course, as well as the other 22 years before that. It is really hard to list all their names here, and I do not want to turn this acknowledgement into a biography. So I have to shrink the list to an appropriate length, and show my appreciation to those who significantly contributed to this dissertation, directly or indirectly.

First, I want to thank my advisor, Professor Douglas Natelson. Doug is one of nicest professor I have ever met. Under his guidance, I have never felt anxious or depressive in any moment of my research. It is not because he has a low standard or expectation on me, but because his trust and encouragement always brings me positive energy and his wisdom always leads me to the right direction. From him, I have learned more than just physics.

Second, I want to thank my parents and grandparents. My grandparents lived in a rural village in China, where my parents originated from. However, the poor living condition never stopped their paces to a higher education. They have experienced the power of knowledge, and respect it more than wealth. So, motivated by them, I had strong interest in science since I was a child, and was very certain to pursue an advanced degree. I appreciate their education and continuous support to me all these years.

Third, I want to thank all the co-authors in my publications. And among them, Dr. Jiang Wei, Dr. Jian Lin and Will Hardy helped me the most. Jiang led me into the world of VO2, and trained me on all the experimental equipment. He was basically my second advisor. Jian (Javen) and Will are like partners to me. Together, we have worked on several projects as a team.

Fourth, I want to thank all the current and previous lab mates: Dr. Daniel Ward, Dr. Jeffrey Worne, Dr. Patrick Wheeler, Dr. Joseph Herzog, Kenneth Evans, Dr. Pavlo Zolotavin, Ruoyu Chen, Yajing Li, Loah Stevens, Charlotte Evans, Panpan Zhou and Benjamin Huber. Doug's personality deeply influences us all, making this lab a welcoming and cozy home for everyone. Though working on different projects, we still discuss physics and help each other every day.

Fifth, I want to thank all the friends of mine here at Rice University. Forgive me for not able to list their names here, but I really appreciate their companion and support to entertain my graduate student life.

Last but not least, I want to thank Yanshu Fei, my girlfriend. 3 years ago, it started as a long-distance relationship when she worked as a flight attendant travelling all over the world. For me and our future, she quitted her job and applied for a master degree program in Houston, even though studying is not her favorite. Her trust and companion is the most important component of my life now.

Contents

List of Figures

Chapter 1

1. Introduction

1.1. What is VO_2?

Strongly correlated materials, a group of materials in which the electron-electron interactions cannot be ignored in condensed matter physics studies, display many interesting phenomena that result from these strong correlations (e.g. the metal-to-insulator transition and high temperature superconductivity). Properly treating such interactions presents a big challenge to the solid state theory. To fully calculate and predict the behavior of electrons in these systems is beyond the limit of current theory, and thus various models and approximations are used to describe the behavior observed in experiments. As a result, experiment remains a vital way to explore strongly correlated materials [1]. Among so many strongly correlated materials, vanadium dioxide (VO_2) is one of particular interest. VO_2 has a dramatic metal-to-insulator transition (MIT) at around 340 K, during which the conductance can change by up to 5 orders of magnitude[2]. Other stoichiometries of V-O systems, such as V_2O_3 and VO, also show similar phase transitions, but with much lower transition temperatures. The close-to-room-temperature transition of VO_2 gives it many potential applications, from field effect transistors to ultrafast optical switches[3]. Although this transition has been known for more than 50 years[2], a new method to synthesize single crystal VO_2 was introduced in 2005[4], which has drawn a lot of attention to this material again in recent years.

The phase transition of VO_2 is a first order transition. The first order phase transition occurs when both phases are local minimum points in the Gibbs free energy, while the difference between the values of these minima changes with parameters. For example, in the common water-to-ice phase transition, when $T<T_C$ (0 °C), the solid phase has the lowest free energy, so it is ice (top part of figure 1.1a). As temperature increases across 0 °C, the liquid phase becomes the new low energy state, thus ice turns into liquid water (bottom part of figure 1.1a). However, such a transition from a higher minimum free energy point to a lower one is not always smooth, due to the existence of the free energy barrier between them. This can be observed in the case of supercooled water, i.e. liquid water with temperature below 0 °C. There are two ways to overcome such an energy barrier: fluctuation, which is why simple stirring can turn supercooled water into ice immediately; and further cooling, which increases the difference between the minimum energy points, shrinking the energy barrier. In the case of VO_2, especially for nano-scale samples, fluctuations are limited, and thus superheating and supercooling always exist. This

results in a hysteresis in the resistance-temperature curve, meaning the transition temperature during heating is higher than the one for cooling. Figure 1.1b gives a typical temperature dependence measurement of a VO_2 nanobeam.

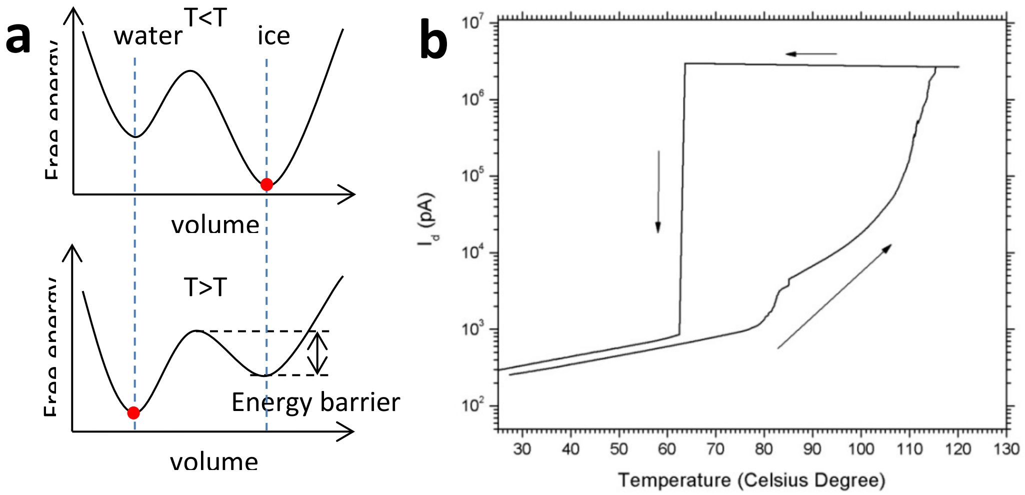

Figure 1.1 First order phase transition. (a) An example diagram of the free energy as a function of a phase parameter (i.e. volume in this case). The lowest free energy state is marked by the red dot. Below T_C, ice phase has the lowest energy, while above T_C, water phase has the lowest energy. Transition from ice to water requires overcoming the energy barrier between the two minimum points. (b) A typical measurement of temperature dependence of conductance of a VO_2 nanobeam. The x-axis is temperature in Celsius degree, and the y-axis is current in a log scale when voltage power supply is fixed at 1 mV. The big hysteresis indicates the supercooling and superheating effect.

Usually, at several degrees below 340K, VO_2 is an insulator, with a monoclinic crystal structure (M1 phase figure 1.2a) [5]. The temperature dependence of its resistance is similar to an un-doped semiconductor, in which the resistance increases exponentially as temperature decreases. In a semiconductor, this phenomenon can be explained by the temperature dependence of the free carrier density n, which follows: $n \propto e^{-E_g/k_B T}$, where E_g is the energy gap between the valence band and conduction band, and k_B is the Boltzmann constant. For VO_2, the fitting of temperature dependence of resistance gives a band gap around 0.6eV. When the temperature rises above 340K, VO_2 turns into a metal with rutile structure (R phase figure 1.2b) [5]. The resistivity of metallic VO_2 (~100 μΩ·cm) is still relatively high compared to a good metal, like copper (~1.7 μΩ·cm), but it shows linear temperature dependence with positive slope like other metals at high temperature. During the transition, the change of the crystal structure is also dramatic (figure 1.2c) [6]. The V atoms along the c-axis of the rutile structure (c_R axis) distort away from the axis, and the adjacent V atoms dimerize to form the a-axis of a monoclinic structure (a_m-axis), with a doubled unit cell. The length of the rutile structure along the c_R-axis shrinks nearly 1% from the monoclinic structure along the a_m-axis. This change is so intense that it usually cause cracks in millimeter-size VO_2 crystals. For nano-scale samples, this shortening can cause extra strain.

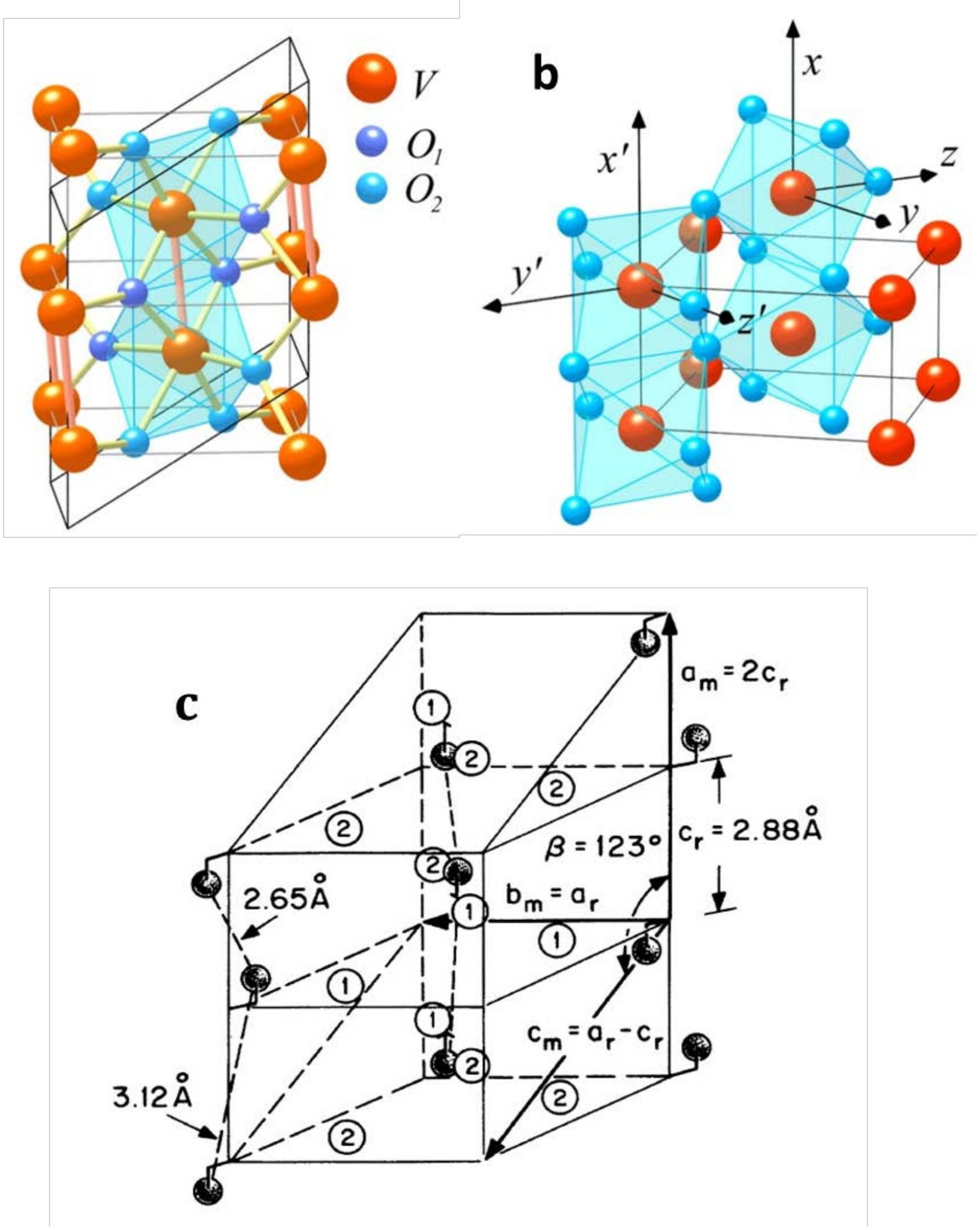

Figure 1.2 (a) Crystal structure of VO_2 in monoclinic phase. (b) Crystal structure of rutile phase [5]. (c) Transformation of VO_2 from rutile phase to monoclinic phase with dimerization and tilting of V atoms along the c_R-axis [6].

Besides temperature, pressure and chemical doping can also affect the phase transition [7, 8], and in some cases, lead to an additional phase (M2 phase)[9]. The phase diagram in terms of temperature and pressure [10], and the phase diagram in terms of temperature and doping [8] are shown in figure 1.3 (a) and (b) respectively. Such modulation of the transition temperature sheds light on the mechanism behind the phase transition, and also provides more possibilities for VO_2 as a functional material.

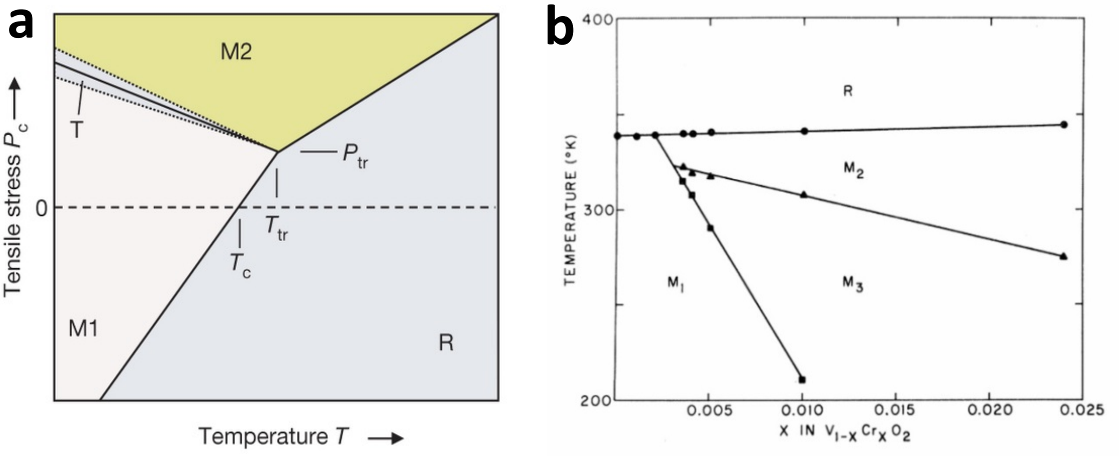

Figure 1.3 Phase diagram of VO_2. (a) Phase of VO_2 as a function of temperature and stress [10]; (b) Phase of VO_2 as a function of temperature and chromium doping [8].

As mentioned in the beginning, there is not a perfect model to describe all strongly correlated systems, including VO_2. The mechanism behind this transition is still debatable, but primarily can be described by one of two models: the Mott-Hubbard picture and the Peierls picture. The Mott-Hubbard model [11], which is applied to Mott insulators, is used to describe insulators with the following characteristics: they should be conducting under conventional band theory, which ignores the electron-electron interaction terms; however, the existence of electron-electron interactions makes them insulators in reality. The Mott model is therefore also described as a correlation-driven mechanism, and in this picture, correlations are the key to induce the energy gap. Although Mott insulators are usually anti-ferromagnetic, like V_2O_3, the absence of antiferromagnetism in VO_2 can be understood as a result of the combination of Mott insulator physics and charge ordering (of the crystal structure). In short, Mott believed that the dimerization of the V atoms in VO_2 during the transition has only a minor effect on the gap [12]. On the other hand, the Peierls model [13] attributes the formation of energy gap to the dimerization of V atoms and tilting away from the c_R-axis. It suggests that the charge ordering caused by this distortion of the crystal structure modifies the band structure, the $d_{\parallel}$ orbit to be specific, splitting it into two separate bands, with a band gap ~0.7 eV [6]. Thus, the structural change, rather than a change in the electronic properties, initiates the phase transition. Although more people tend to believe the insulating phase of VO_2 is a Mott insulator instead of a conventional band insulator [14], it is hard to distinguish these two mechanisms during the transition, because, in reality, both the resistance and the structure change simultaneously with no obvious causal relationship. Some groups claim the observation of the separation of these two mechanisms [15, 16], but much evidence from experiment and theory still indicate that both factors play important roles in driving the phase transition [17-19].

1.2. Synthesis of VO_2 nanobeams

The technique we use to grow VO_2 nanobeams is physical vapor deposition[4]. As shown in figure 1.4, V_2O_5 powder source is placed in a ceramic boat located in the center of a tube furnace setup, and a silicon (Si) substrate (1cm*4cm) with 2μm thermal oxide is placed 3 ~ 5cm away from the edge of the boat in the downstream direction. Argon flows into the tube at a constant rate as a carrier gas, and a mechanical pump maintains the tube in vacuum. Then, the furnace temperature is ramped to 900 ~ 950 °C in 30min, and is maintained for 30 min before cooling down naturally. We do not measure the accurate pressure in the chamber and the flow rate of argon, but by using the same settings for all the valves in the system, we are able to achieve a repeatable crystal growth outcome.

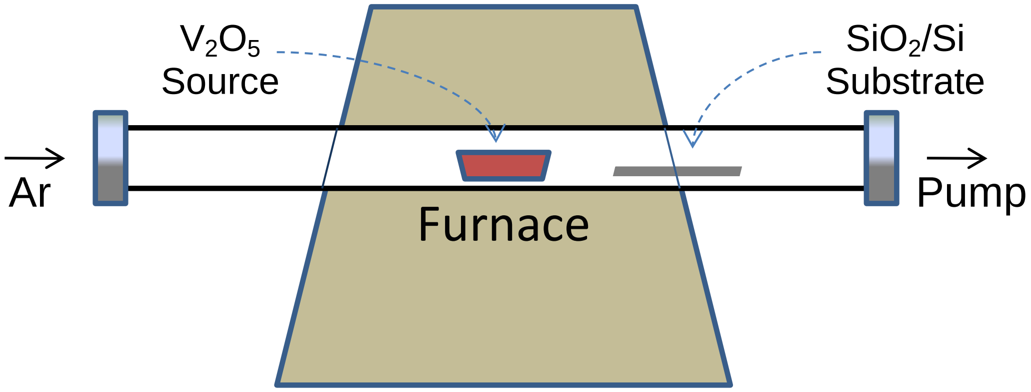

Figure 1.4 Scheme of the synthesis system setup.

By adjusting the flow rate, pressure, and distance between substrate and boat, we can obtain different kinds of VO_2 samples. Figure 1.5 shows several typical growth results: 1.5.a nanobeams; 1.5.b micron-scale flakes; 1.5.c continuous sheets; 1.5.d cantilevers. The width and thickness of nanobeams are usually from 40 nm to 2 μm, and the length can reach up to hundreds of microns. For the flakes, the lateral size can be hundreds of square microns, and the thickness is typically between 40nm to 200nm.

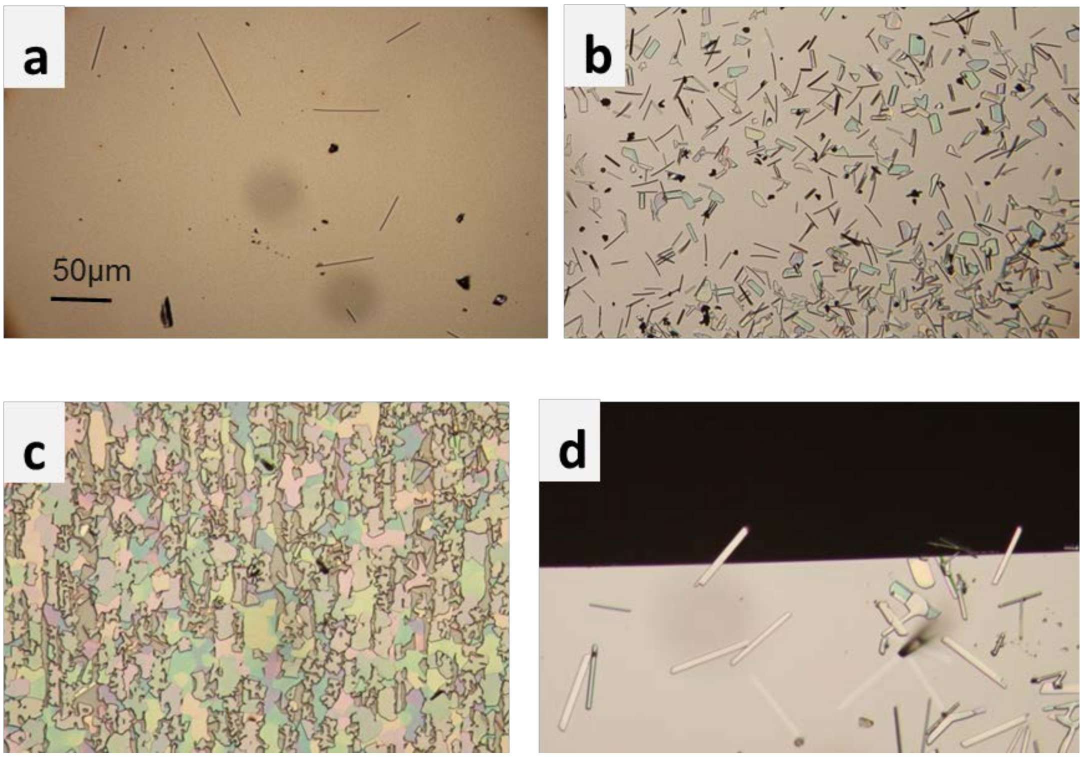

Figure 1.5 Photos of PVD grown VO_2 samples in different shapes. (a) Nanobeams; (b) micron-size flakes; (c) continuous sheets; (d) cantilever.

VO_2 nanobeams are one of the best candidate structures to investigate the transport properties of this material for several reasons. First, they are single crystals, thus exhibiting the purest intrinsic properties with the least effect from grain boundaries. Second, their flexibility, thanks to their small scale, makes the nanobeams relatively robust and repeatable compared to the bulk material, which may crack after several transition cycles. Third, the domains that can appear during the phase transition can be visibly distinguished under an optical microscope. This feature has many advantages from an experimental point of view. For example, Raman measurements on different domains in the same beam at the same temperature are now possible. VO_2 nanobeams are grown along their c_R-axis, which changes most dramatically during the structure transition, allowing the strain of the nanobeams to be easily manipulated. Notably, the phase diagram of VO_2 as a function of temperature and pressure shown in figure 1.3 is a product of the control of strain in VO_2 nanobeams [10].

1.3. Nano-fabrication

Due to the size of our samples, a nano-scale fabrication technique is necessary to make measurable devices out of the VO_2 samples. Three different methods are applied in this thesis to fabricate metallic contacts: shadow masking, photolithography, and electron beam lithography (e-beam), each with its own advantages and limitations.

1.3.1. Shadow masking

Shadow masking is the simplest technique of the three. The masks we have designed and used are usually 1 inch by 1 inch squares made of silicon or stainless steel, and are ordered from commercial suppliers. There are open windows on the mask to form certain patterns. A mask is then aligned on top of the substrate containing VO_2 samples. Sometimes, the location of the pattern must be accurate within less than 50 μm, thus an optical microscope is required to align the mask with respect to the substrate. Figure 1.6 shows a home-made aligner to perform such fine adjustment: a sample holder is attached on a manipulator with position control of x, y, and z directions, and a mask is adhered on the frame with its pattern area located on the hole of the frame. Under an optical microscope, we can see the sample chip through the open windows of the mask, and at the same time, push the sample towards the mask so that patterns will be aligned directly on top of the sample. After successfully aligning the mask on the substrate, we can then put them both in the chamber of an electron beam evaporator and deposit the desired materials (usually Ti/Au). The deposited material will form the same shape on the substrate as the pattern of the mask. If the location of this pattern on the chip is not critical, then a simple clip to hold the mask and substrate together in the evaporator chamber works, too.

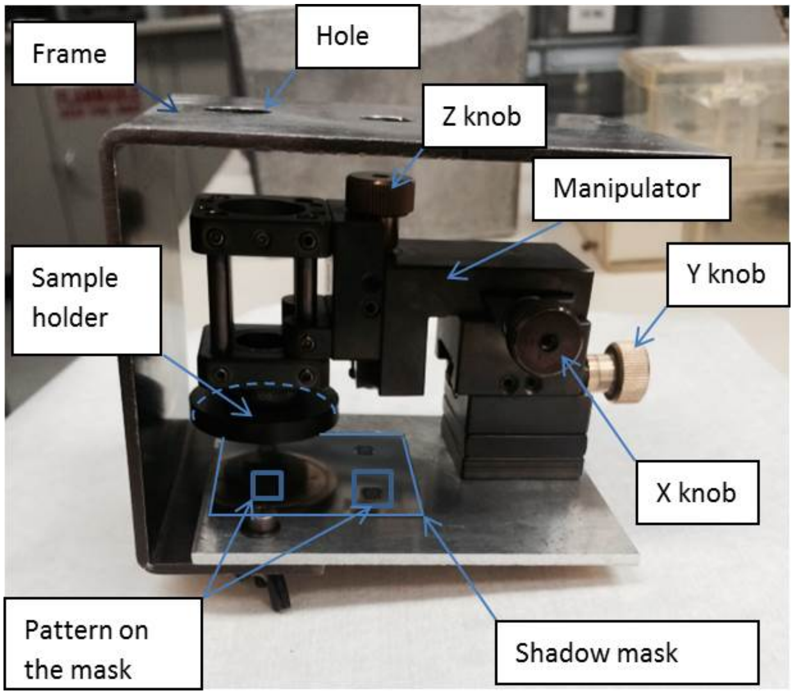

Figure 1.6 Photo of the shadow mask aligner. The surface of the sample holder is facing down, thus can be seen from the mirror image reflected by the shadow mask. There are several patterns on the mask, but only the one facing the sample holder actually works (not obvious from this angle), because there is a hole on the frame underneath it (cannot be seen in this angle, but similar to the hole on the top part of the frame), where deposition can go through.

The advantage of the shadow masking method is obvious: it's quick, convenient, and chemical-free. By avoiding certain steps, like heating, developing, and rinsing, which are required for lithography, it makes nano fabrication on certain samples possible. However, the weaknesses are also critical. First, the resolution of this technique is quite low. The pattern itself has a resolution on the order of microns, and so does the aligner. As a result, any fabrication requiring a resolution less than 10μm is difficult, if not impossible. Second, microscopically, there is always a void between mask and substrate, so that the deposition on the substrate cannot have a sharp edge. Such a blunt edge can extend as far as several microns, further affecting the resolution of the actual pattern. This problem is already significant for samples metalized in an evaporator in which particles have a straight trajectory from source to sample. In the case of sputtering deposition, in which particles are scattered in every direction, the existence of the void can completely ruin the pattern. Finally, the shadow masking technique cannot pattern closed-loop features, because anything inside of the close loop would not have support or connection to the mask. For example, a shadow mask can be used to make a closed circle "●", but not an open circle "○".

1.3.2. Photolithography

Photolithography is a common technique in the nano-fabrication field, especially in large-scale manufactoring. All the CPU chips used in our computers are made by photolithography. In industry, the technique has been optimized so well that the resolution is approaching to 10nm. However, at Rice, the UV lamp we use provides a resolution limit around 300nm, and since the magnification of the mask aligner's optical microscope is somewhat low, the accuracy for aligning the mask is around 2μm.

The procedure of photolithography is as follows: first, spin-coat primer (MicroChem MCC 80/20) and photoresist (SHIPLEY S1813 in our experiment) on top of the substrate, and cure it based on the requirements of the resist; second, align the photo mask on top of the substrate and press them together with photoresist in between; third, shine UV light through the pattern of the mask for a certain time to expose the specific area; fourth, soak the substrate in developer to chemically remove the photoresist from the exposed area; fifth, deposit material on the whole substrate; and finally, soak the substrate in stripper to lift off all the photoresist along with the deposited material on the resist, leaving only the exposed region on the substrate with the material coating.

A photomask is a square piece of glass with a chromium film on it. Certain patterns can be written in the chromium to create a transparent window for UV light to pass through. It functions similarly to a shadow mask, expect that there are no actual holes through it, allowing more complicated patterns. Also, the contact between the photomask and the soft photoresist can be microscopically void-free.

Compared to shadow masking, photolithography is much more precise, due to better resolution of patterns on the photomask and the void-free contact. It is possible to make multiple patterned substrates one by one using a single photo mask, and deposit material for all of them at the same time to reduce the consumption of materials, especially gold or other expensive elements. However, the disadvantages are also clear: more steps complicate the fabrication, and sometimes make the fabrication infeasible, such as when the samples contain something soluble or reactive in developer or stripper.

1.3.3. E-beam lithography

E-beam lithography is the technique used the most in our experiments. It is similar to photolithography, except that the photoresist is replaced by Poly(methyl methacrylate) (PMMA), with the corresponding chemicals for developing and lifting-off exchanged for those compatible with PMMA, and the UV exposure with help of a photomask is replaced by direct e-beam exposure in a scanning electron microscope (SEM). Although it is even more time consuming than photolithography, the benefit it comes with is often worth the extra effort. The pattern is designed using CAD software, and is then directly written on the substrate, allowing more flexibility in the design of the pattern, especially when frequent changes of design are required. It also provides the finest resolution of the pattern, as little as 20nm, and the most accurate alignment.

However, some intrinsic disadvantages limit the application of e-beam lithography, or require alternative steps. Besides the complicated procedures and the involvement of chemicals similar to photolithography, e-beam lithography also requires a conducting substrate to prevent accumulation of charge on the substrate during patterning. This charging issue can distort the electron beam, and thus influence the shape and location of the pattern. In cases when insulating substrates must be used, spin coating a conductive polymer (e.g. poly(3,4-ethylenedioxythiophene)-poly(styrenesulfonate) (PEDOT-PSS)), or depositing a thin layer of metal (e.g. 0.5~4nm chromium) on top of the PMMA can help dissipate the charge. Another issue caused by the mechanism of e-beam lithography is that the region of interest cannot be “seen” before lithography. In photo-lithography, the “viewing” or “locating” step, via optical microscope, is different from the exposing step, which uses UV-light. However, in the SEM, “viewing” has basically the same mechanism as exposing, expect usually a higher electron energy (30KeV) used for the latter. As a result, alignment must be done in a different way by using alignment marks.

The purpose of alignment marks is to locate the sample of interest without actually seeing it. To achieve this goal, we need to know the relative location of the sample with respect to the marks (by measuring under an optical microscope in advance) and the location of the marks (by viewing in the SEM). Anything can work as an alignment mark as long as it is visible in the SEM (meaning small enough and with sharp features) and close to the sample. The definition of “close” is determined by the size of the sample and the pattern to be written. In my experiments, two kinds of alignment marks are used. The first is an array of gold cross marks deposited all over the substrate (figure 1.7a) by photo-lithography, with the distance between marks from 200 μm to 800 μm. By taking photos of the block in which the sample is located, we can map it later in the SEM. Since the array is made by photo-lithography, it can be quickly manufactured in large scale, and the outcome is accurate. But with hundreds by hundreds of orderly indistinguishable marks, counting the coordinates becomes a new problem. Therefore, in practice, another technique uses scratch marks that are applied for relatively large sample (>10 μm). Using a needle probe attached on a micro-manipulator, we can finely scratch the

PMMA on the area near the sample of interest (figure 1.7b). The typical size of the scratches is around 50μm*500μm, so they can be easily found in the SEM even using the smallest magnification, and sometimes by bare eyes at certain angles. This method, though it sounds coarse and unprofessional, is convenient and precise enough for most of our needs.

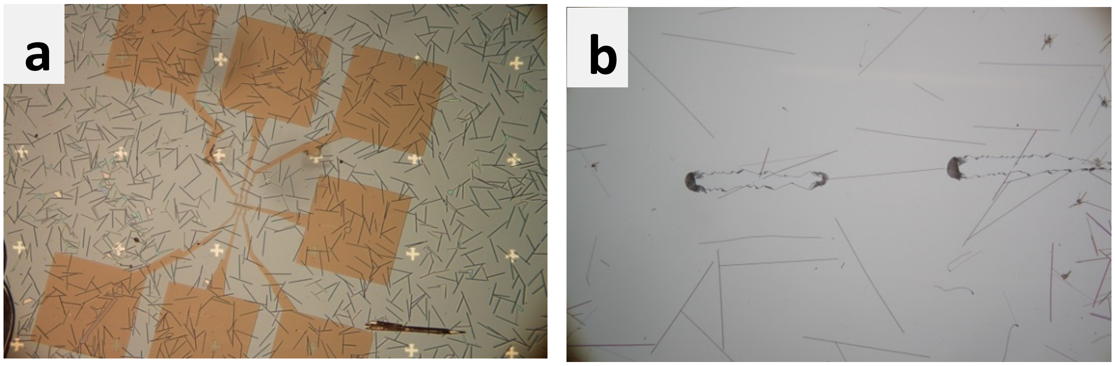

Figure 1.7 Photos of alignment marks. (a) An array of cross marks are patterned by photo lithography, and then deposited with Ti/Au. The VO_2 nanobeam of interest is then located and fabricated by e-beam lithography with the help of the alignment marks. The final device has a dark orange color, due to the relative thin Au layer (~15 nm). (b) The PMMA spin-coated on top of the sample is scratched by a probe attached on a micro-manipulator. The two scratches mark the two ends of the VO_2 nanobeam of interest.

A photo of a VO_2 nanobeam device made by e-beam lithography is shown in figure 1.7a. A 5nm adhesion layer (vanadium or titanium), and 15 to 100nm gold (V/Au) are deposited on the nanobeam as contacts, which connect the beam to large V/Au pads (typically 300*300μm^2), so that probes or gold wires can be used to interface them to the measurement equipment. A magnified side view of the center part of a similar device taken in the SEM is shown in figure 1.8. Sometimes, to ensure better contact between the gold and the nanobeam, sputtering deposition is used instead of e-beam evaporation. As mentioned above, in sputtering deposition, material particles travel in all directions, so they can form a deposition layer on the side of the nanobeam, rather than only the top surface facing the source, as is the case in evaporation. This is especially important for thick nanobeams (>300nm), where gold contacts on top of the beams and those around beams may lose connection. However, the tradeoff is the difficulty that occurs upon lift-off, because such side deposition also covers the sides of the PMMA layer, protecting the PMMA from being dissolved by stripper (acetone). Even if PMMA is able to be lifted off, the connection between the deposited material on the substrate and that on top of the PMMA can either peel off the material on the pattern area or leave some residue material which is supposed to be removed.

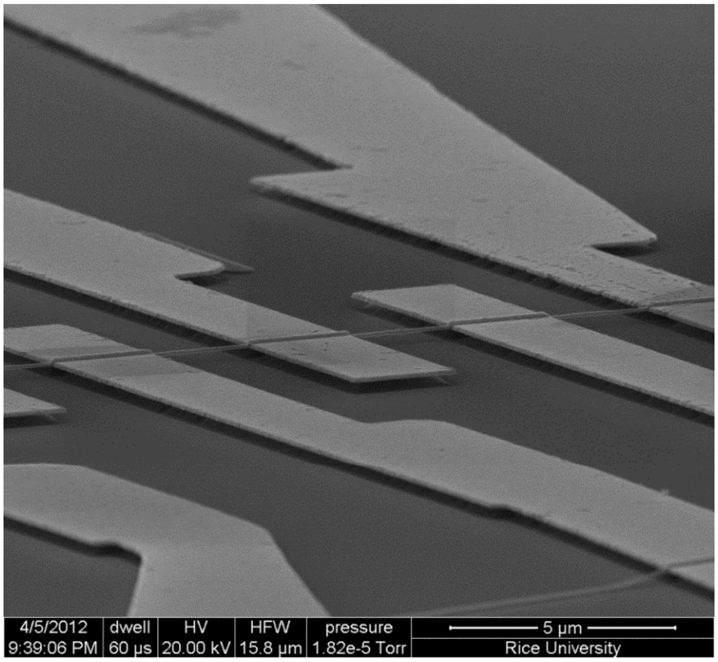

Figure 1.8 an SEM image of the center part of a VO_2 nanobeam device taken from a tilted angle. Multiple contacts are deposited on top of the VO_2 nanobeam. The nanobeam is suspended from the substrate (explained in section 1.4.2).

1.4. Characterization

1.4.1. Effect of strain

A typical plot of the temperature dependence of the resistance is shown in figure 1.1b. As is obvious, there is a huge hysteresis across the transition. The heating curve has multiple jumps, and the fully metallic phase cannot be reached until 390K, much higher than the 340K observed in the bulk. However, the transition in the cooling curve is close to 340K, and very sharp. This phenomenon can be well explained by the effect of strain. Because the nanobeams are grown at about 900 °C, the underlying SiO_2 surface becomes soft during the crystal growth, and the nanobeams are slightly embedded in the substrate. This causes a very strong bonding between the beams and the substrate, and such bonding induces a strain on the beams during the transition, which tends to maintain the beams in the monoclinic structure (insulating phase). As a result, many domains are formed during the transition to gradually overcome the strain effect (figure 1.9), and a relatively higher temperature is required for the transition to be completed.

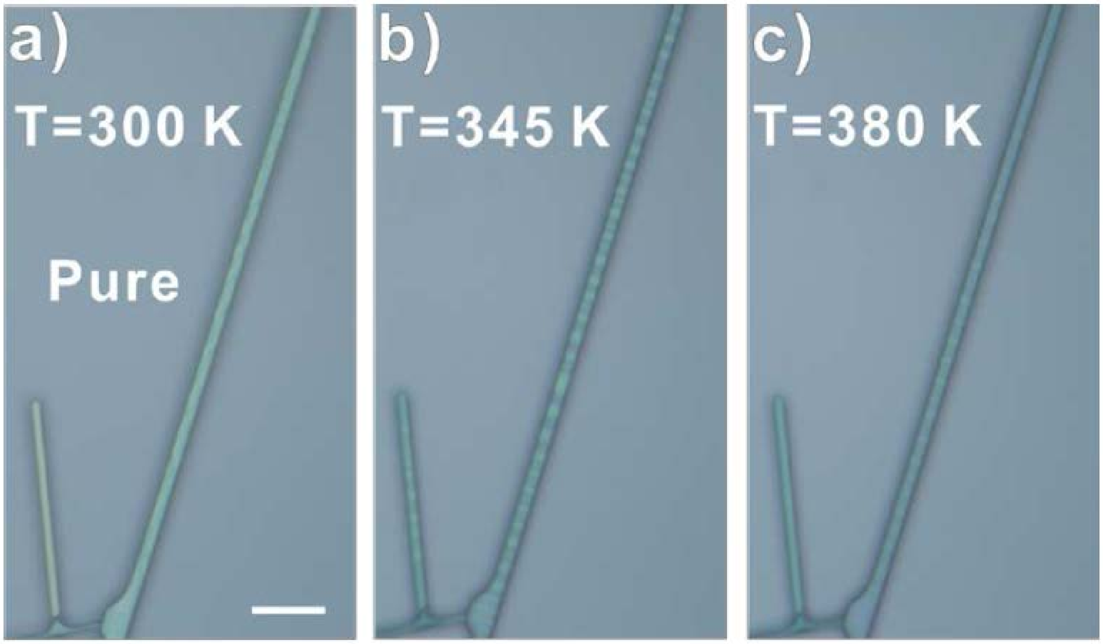

Figure 1.9 Optical microscopy of a VO_2 nanobeam across the phase transition. (a) At room temperature, the whole beam is in insulating phase. (b) At 345K, some dark-color metallic domains begin to appear, suggesting the occurrence of phase transition. (c) At 380K, the whole beam turns into nearly uniform dark color, except a few light-color stripes, meaning the phase transition is almost done [20].

1.4.2. Strain-free sample

There are two primary ways to avoid this strain effect in nanobeams. One is to etch away the substrate after putting on contacts, making a suspended beam (figure 1.10a). A buffered oxide etch (BOE) solution (6:1 volume ratio of 40% NH_4F in water to 49% HF in water) is used to fulfill this job. It can etch SiO_2 at a rate of around 70nm per minute. The use of BOE requires extreme caution, due to the presence of HF, a highly corrosive, penetrating and volatile acid, so it must be done in the fume hood with enough protection. Usually, 2 to 3 minutes are needed to fully suspend the VO_2 beam from the substrate, meaning an etching of about 200nm of SiO_2. That is also the reason why the substrate with 2μm oxide is used in this case, since we do not want to etch all the SiO_2 away, causing a current leakage from our sample to the grounded substrate in a transport measurement. These suspended beams have comparatively little strain, and can change shape during the transition from straight (shorter rutile structure) to buckled (longer monoclinic structure). However, the cost of these desirable properties is that suspended nanobeams are very fragile due to the lack of support from the substrate (figure 1.10b). To further reduce the strain, we even tried to fabricate a suspended gold contact on one end of the beam, with the other end fixed by a normal-size gold contact, so that the suspended contact can move along with the beam across the transition. However, because of mechanical weakness, this attempt was not successful (figure 1.10c).

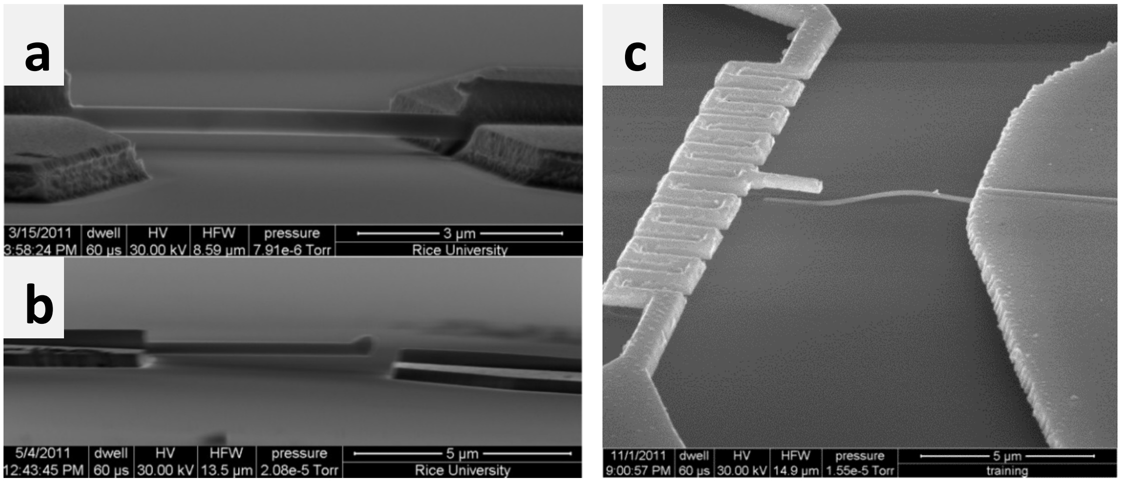

Figure 1.10 (a) An SEM image of suspended VO_2 nanobeam devices after BOE etching. (b) An SEM image of the broken nanobeam after measurement, likely due to electric shock. (c) Suspended nanobeam device with suspended contact (zig-zag shape on the left). The wire bends down due to insufficient adhesion with the left contact.

The other way to reduce the strain is to transfer nanobeams from their growth substrate to another one, thus releasing them from the embedded state. BOE is also needed to etch the SiO_2 surrounding the nanobeam, and then, the etched substrate is put on top of a fresh substrate, face to face. After tapping on the back of the top substrate for multiple times, some beams will fall onto the bottom substrate. Sometimes, we can find vertically grown VO_2 nanobeams. As for them, without the etching step, simply overlapping and tapping can transfer beams to a new substrate. The transferred beams still have some strain, due to the direct contact with the substrate, but much smaller than that of the embedded beams. Compared to suspended beams, these transferred nanobeams are more robust. After taking all these features into consideration, we ended up using the latter type of devices for most of our transport measurements.

Chapter 2

2. Ionic liquid gating on VO_2 nanobeams

Part of this chapter is reproduced from the published paper [21]:

Modulation of the Electrical Properties of VO2 Nanobeams Using an Ionic Liquid as a Gating Medium

Heng Ji, Jiang Wei, and Douglas Natelson

Nano Letters 2012 12 (6), 2988-2992. DOI: 10.1021/nl300741h

After talking so much about the special features VO_2 has, the question arises: what can we do to investigate the physical properties of this material? Our first idea was to use electrostatic gating to modify the electronic transport properties or the phase transition of VO_2.

2.1. What is electrostatic gating?

In electrostatic gating, an external electrical field is applied on a material (usually semiconductor) to modulate its conductivity. This field effect does not work on metals, due to the high density of electrons in metals which screens the external field, but for some semiconductors, it is quite efficient. The external field can penetrate into the semiconductor and bend its band structure. When such band distortion is big enough, the band can cross the Fermi level near the surface region and become partially filled by electrons, inducing a conducting channel there (figure 2.1). This idea is the foundation of field-effect transistors (FETs).

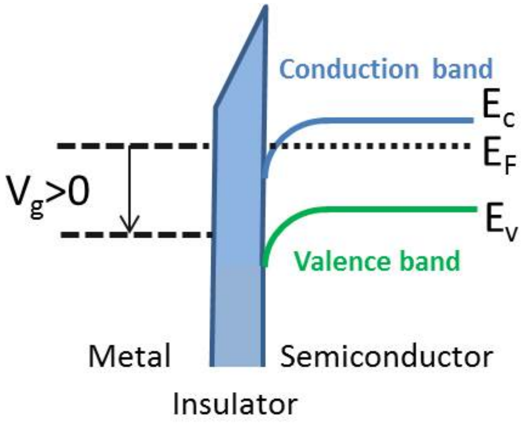

Figure 2.1 Scheme of the field effect on the band strucuture of a semiconductor.

Ideally, when a strong enough external field is applied, any semiconductor can be modified to form a conducting channel, but in reality the strength of field E has its limit. E is determined by $E=V/d$, where V is the applied voltage and d is the distance of the voltage drop. So, to form a maximum E, we want V to be as large as possible, and d as small as possible. In a typical solid gate structure, a layer of insulator (usually an oxide) is used to separate the gate contact and semiconductor. When the thickness of the insulator layer approaches 1nm, a tunneling current appears to cause a leakage current from the gate contact to the semiconductor. In extreme cases, when the voltage is beyond a certain limit, a breakdown of the insulator can occur, resulting in a large leakage current. To overcome this limit of the electric field, a group of insulators called high-κ materials are used as gate insulators. Their advantage is that they can produce higher concentration of accumulated charges (2D charge density $Q/A=\kappa\varepsilon_0 E$) for the same strength of electric field, and thus provide larger modulation. At the same time, to achieve the best quality of the insulating layer, atomic layer deposition is required to deposit a single crystal film. HfO_2 and ZrO_2 are the most common high-κ materials with $\kappa = 25$ [22].

In the past 50 years since the discovery of VO_2, people have thought about and tried electrostatic control of VO_2. Since the insulating phase of VO_2 behaves like a semiconductor with 0.6 eV band gap obtained from its temperature dependent resistance, such a proposal is reasonable, and should be feasible. However, no matter what gate insulator is used, traditional oxide or high-κ, no one has shown any convincing modulation in VO_2 of the MIT or the resistance [23, 24]. In addition, some of the asserted observations of modulation can be explained by self-heating effects induced by a big leakage current through the insulating layer. Some people attribute this bizarre phenomenon to the strong correlations, while others believe that the high carrier density observed in Hall measurements in VO_2 implies a very short screening length, similar to a metal even in the insulating M1 phase, which limit the penetration of the field effect.

After considering these previous attempts, we proposed a new way to push the field effect to the limit: ionic liquid.

2.2. What is ionic liquid?

The term “ionic liquid” describes a group of salts whose melting point is usually below room temperature, so they are in the liquid state in their function temperature. Compared to pure water and oil, whose molecules are electrically neutral, ionic liquids contain many more ions. When it is used as an electrolyte, where a voltage is applied between two electrodes inserted in it, an electrical double layer (EDL) can be formed on the liquid-metal interface. Most of the voltage drop happens at this nanometer-scale EDL, forming a strong local electric field there. Due to the high concentration of ions and small leakage current, ionic liquids are a promising material for electrolytic gating.

The ionic liquid had demonstrated its advantage as a gate material through several successful examples. A gate-driven insulator-to-metal transition has been achieved on wide band gap (~3.3eV) semiconductor ZnO transistors [25]. In the insulators $SrTiO_3$[26] and $KTaO_3$[27], superconductivity was observed in ionic liquid-gated single-crystal devices. In an example very related to our proposal, an ionic liquid gating experiment on sputtered VO_2 films[28] has shown a reduction in channel resistance at positive gate potentials in the monoclinic phase with a slow time dependence to the response. However, this experiment had a major deficiency that the VO_2 film used was polycrystalline grown by sputtering, and may not reflect the most intrinsic properties of VO_2. Also, the paper did not provide a very convincing explanation of the time dependent gate effect. So, rather than polycrystalline films, in this work we used individual single-crystal VO_2 nanobeams grown by vapor phase transport. These crystals possess a highly homogeneous surface (~1 nm roughness) and minimal lattice defects compared to conventionally deposited VO_2 films.

2.3. Modulation of conductance

The contacts for the five-terminal devices were patterned by e-beam lithography and Ti/Au (typically 5nm/100 nm) deposition via e-beam evaporation. An overlayer of Al_2O_3 was subsequently evaporated on top as a protection layer and to separate the ionic liquid from the source and drain electrodes, while a window in the center of the pattern was opened to guarantee the contact between ionic liquid and the VO_2 nanobeam. The ionic liquid N,N-diethyl-N-(2-methoxyethyl)-N-methylammonium bis-(trifluoromethylsulfonyl)-imide (DEME-TFSI) from Kanto Chemical Co. was chosen because of its large electrochemical stability window (reportedly as high as −5 to +5 V)[29] and deposited on the fabricated device by micromanipulator (see Figure 2.2a). As shown in Figure 2.2b, a small ac voltage (V_{sd} = 1 mV rms) at 13 Hz was applied between source drain electrodes and the resulting ac current (I_{sd}) was measured via lock-in amplifier. Dividing I_{sd} by V_{sd} gives the conductance, G, which is plotted in subsequent figures. Since the conductance of VO_2 is very sensitive to temperature, a small ac voltage of about 1 mV rms was used, to prevent possible Joule heating in the VO_2 and to limit transport to the linear response regime. A dc voltage (V_g) was directly applied to gate electrode, and the corresponding current (I_g) also monitored during the measurement. A total number of 20 devices have been examined with consistent results.

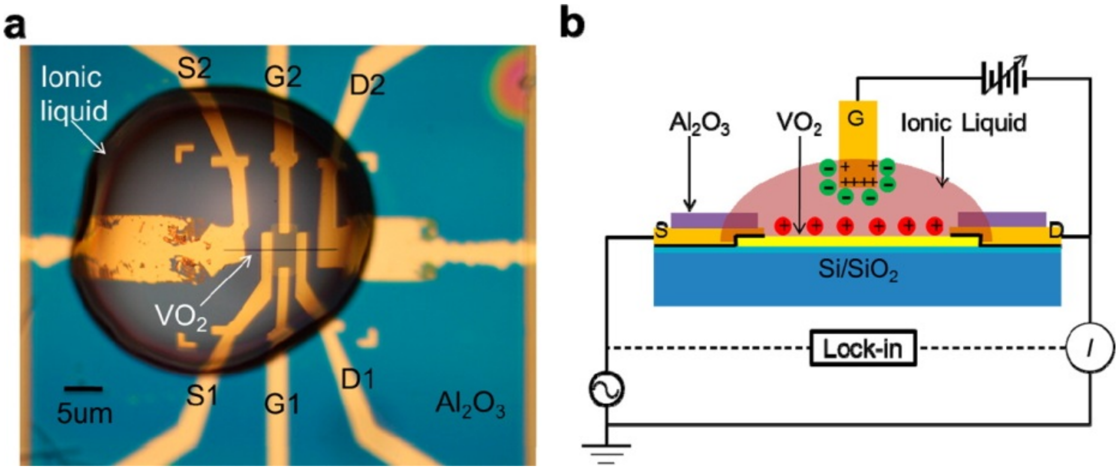

Figure 2.2 Photo and scheme of the device. (a) Optical micrograph of fabricated VO_2 nanobeam device with ionic liquid deposited. The whole area is protected by a 100 nm thick Al_2O_3 layer (apparent blue color when not covered by the ionic liquid) with a rectangular window in the center only (lighter region between leads S1 and D1) where the ionic liquid is contacting the VO_2 nanobeam. (b) Schematic diagram of the measurement circuit, where a lock-in amplifier is used to measure the source–drain differential conductance and a variable DC supply (with current measurement) can apply a bias to the gold lateral gate electrodes (G1 and/or G2) and measure gate leakage current. [21]

Prior investigations have shown that water can be easily dissolved into an ionic liquid upon exposure to ambient air[30], and in general DEME-TFSI contains trace water from its synthesis[31]. To minimize the water contamination, we baked the sample with DEME-TFSI in vacuum (10^{-5} Torr) at 110 °C for 12 h before the measurement. Figure 2.3a shows the G –Vg sweep with Vg sweeping at a rate of 2 V/min from 0 to 3 V at a set of different temperatures from 150 (where the ionic liquid is completely frozen) to 338 K, right below the metal–insulator transition. Figure 2.3b shows the simultaneously measured gate current, I_g, which is about 2 orders magnitude smaller than the source–drain bias current. I_g has two contributions. The first contribution is the Vg-independent level of I_g, which represents the capacitive charging and discharging current when Vg is swept at a constant rate, and is determined only by sweeping rate and direction. The second contribution is the sloped I_g component superimposed on top of the capacitive current, which corresponds to the leakage current when there is a possible electrochemical reaction, the Faradaic current. At each set temperature, leakage current monotonically increases with increasing V_g, and for a fixed V_g, higher temperature induces higher leakage current. At temperature below the freezing point of DEME-TFSI (200 K), both capacitive current and leakage current approach zero, as expected.

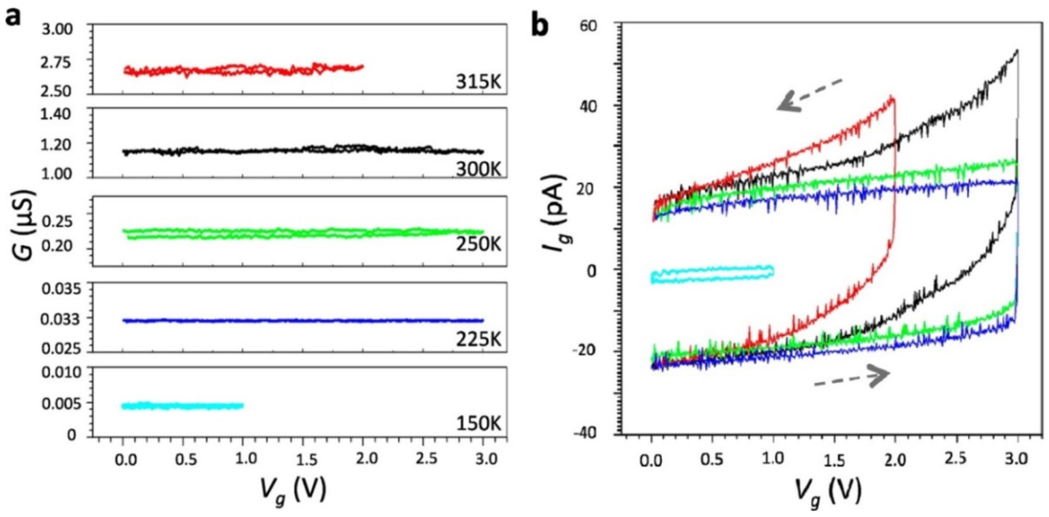

Figure 2.3 Gate dependence of (a) source–drain conductance and (b) gate current on a DEME-TFSI gated device at a set of temperatures. DEME-TFSI for this device was dehydrated by baking the device *in situ* in vacuum at 110 °C for 12 h prior to electrical measurements. Note that there is essentially no gate modulation of the conductance in this dry device. [21]

Comparatively, the leakage current is much smaller than the total I_{sd} at all temperatures. This suggests that electrochemical reactions are minimized by the baking/dehydration process. Within the resolution of the measurement setup, we can see that there is no significant gate dependence for the source–drain conductance in the temperature range from 150 to 338 K and gate sweep range from 0 to 3 V. When V_g exceeds 3 V at room temperature, apparent leakage current increases rapidly. Therefore we limit V_g to less than 3 V to minimize possible chemical reactions of the oxide during the gate sweep. (We also swept the V_g to the negative side, which will be discussed later.)

For comparison, devices with ionic liquid that was not dehydrated, that is, containing trace water, were also measured in the same setup. The transconductance data in Figure 2.4 shows that for temperatures above 200 K, conductance monotonically increases with V_g sweeping from 0 to 1 V. However when V_g is swept in the opposite direction from 1 to 0V, the conductance does not retrace the initial response. Instead, the device conductance displays a hysteresis that increases in magnitude with the increasing temperature (below the metal−insulator transition). As expected, at a temperature of 150 K below the ionic liquid freezing point the water contaminated devices behave similarly to the dehydrated devices, showing no gate dependence.

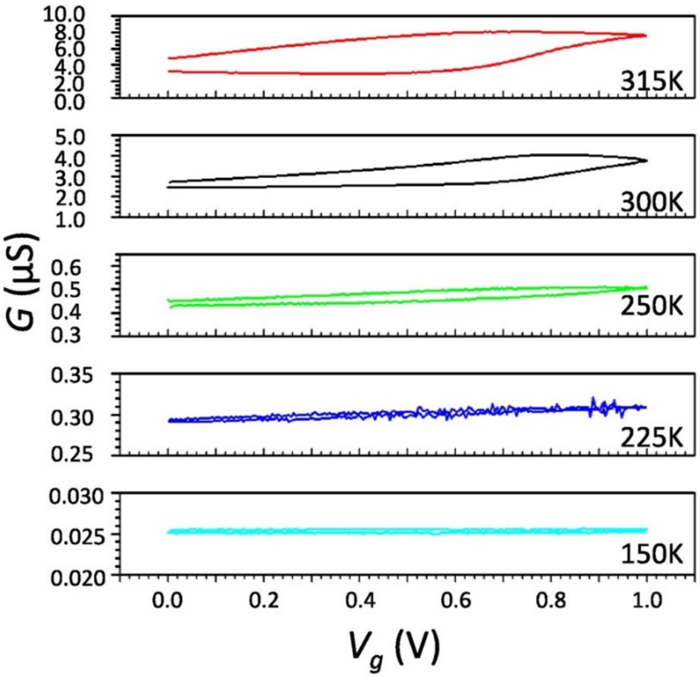

Figure 2.4 Gate dependence of source–drain conductance on a water-contaminated DEME-TFSI gated device at a set of temperatures. [21]

2.4. Water contamination and role of hydrogen

The dramatically different gate responses from devices with and without the dehydration treatment suggest that ions resulting from trace amounts of water inside the ionic liquid play an important role in modifying the conductivity of VO_2. Slow, hysteretic gate response in the presence of water-containing ionic liquids has been previously reported in ZnO based devices[32]. In that case, the very large change in source–drain conductance at positive gate potentials has been ascribed to the splitting of water and the resulting protonation of the exposed ZnO surface[32].

To verify this conjecture about the role of water, we intentionally used hydrogen-containing solutions as the electrolytic gating media, including water, neat p-terphenyl mercaptan (TPM) (a small conjugated oligomer that can dissolve some moisture when exposed to air), and a concentrated solution of phenol (C_6H_5OH, also known as carbolic acid) in polyethylene glycol diacrylate (PEG-DA) with ratio 1:6 by weight. As plotted in Figure 2.5, devices with all three solutions show strong, slow, hysteretic gate dependence in the source–drain conductance, supporting the case that water dissolved in the ionic liquid can result in apparent gating. The device using phenol exhibits the strongest gate dependence at room temperature with a change in conductance of nearly 2 orders of magnitude with 1.4V gate voltage applied. We believe that this comparatively large response results from the relatively high concentration of hydrogen ions because of the acidic character of phenol. This modulation is so large that it raises the question of whether the surface of the VO_2 nanobeam is being protonated, or whether the bulk of the nanobeam is being doped chemically via the diffusion of the hydrogen ions. Other electrochemical experiments have demonstrated that it is possible to dope VO_2 films with hydrogen atoms via electrochemistry [33], and intercalated atomic hydrogen is known to act as a donor in rutile TiO_2 [34].

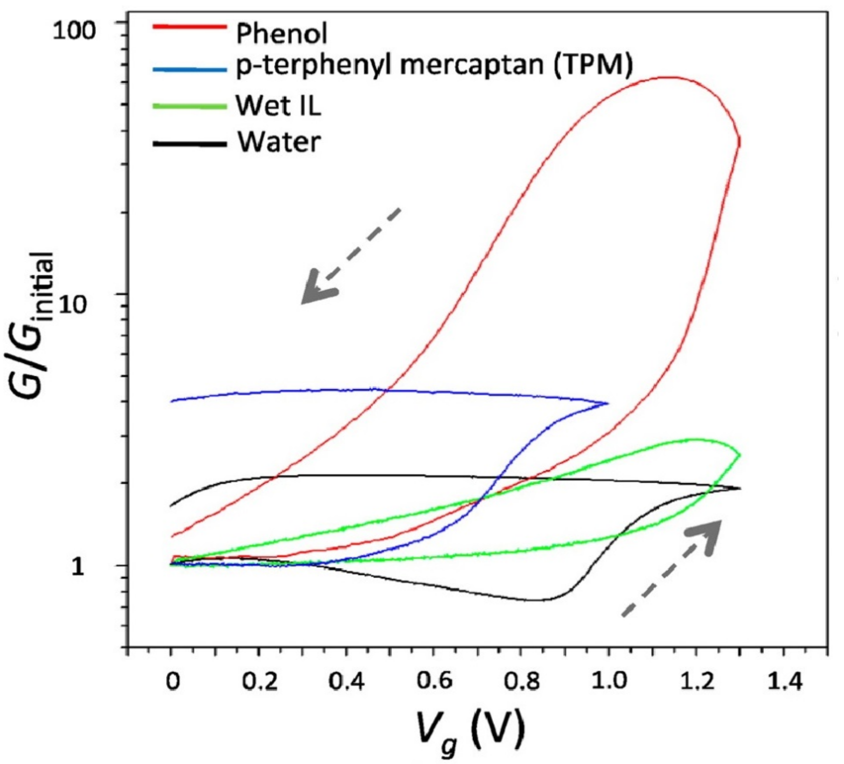

Figure 2.5 Gate dependence of source–drain conductace at 300 K on devices with other gating media: water, water contaminated DEME-TFSI, TPM, and a mixture of phenol and PEG-DA (1:6 by weight), respectively. Conductance has been normalized to the initial value for each device, so that multiple devices of different nanowire geometries may be compared. All gate sweeps are conducted at 2 V/min. [21]

2.5. Time dependence and temperature dependence

To further explore the diffusion dynamics of hydrogen ions, we repeatedly swept V_g in a loop at 2 V/min. Figure 2.6 shows the conductance response for a typical device in the presence of “wet” DEME-TFSI. With a constant V_g sweep rate of 2 V/min and range from 0 to 1.3V, conductance responds to V_g in a hysteretic fashion that drifts upward with decreasing on/off ratio, settling to a stable loop, while I_g remains steady without distinct drift. The slow evolution of the conductance suggests the process of diffusion of hydrogen ions into VO_2 nanobeam or the accumulation of hydrogen ions at the interface. We also observe that after the gate sweeping process, the increased source−drain conductance relaxes toward its original unprocessed state, but never recovers completely. Further measurements suggested that sweeping to smaller values of V_g leads to an easier recovery of the conductance. This irreversibility of the increased conductance is a characteristic sign of electrochemical doping, and is inconsistent with purely electrostatic gating.

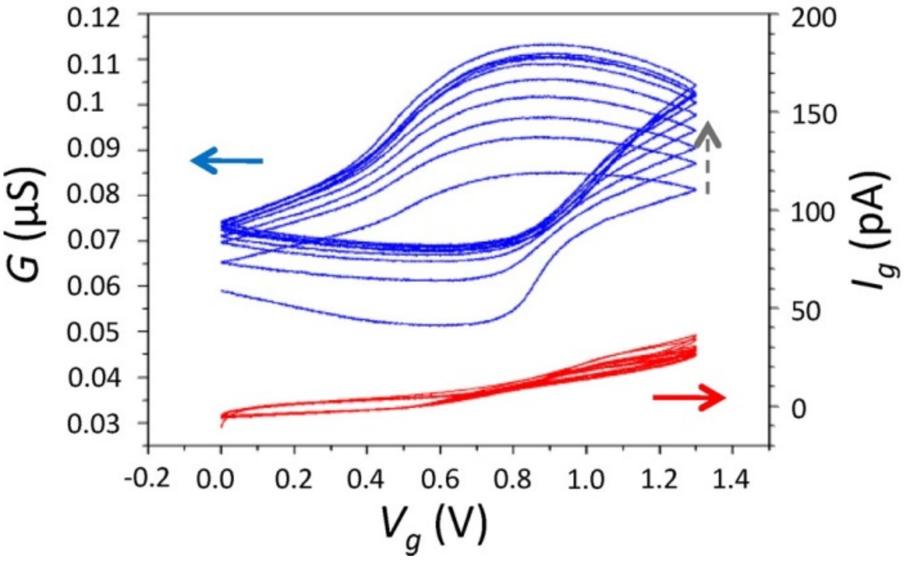

Figure 2.6 Response of source–drain conductance (blue curve, upper) and I_g (red curve, lower) with V_g sweeping continuously between 0 and 1.4 V at room temperature for a typical device gated with water-contaminated DEME-TFSI. The gate sweep rate is 2 V/minute. The dashed arrow indicates the temporal drift of the conductance. [21]

Temperature is a critical factor in this electrochemical effect. At temperatures below the metal−insulator transition (T < 340K), the conductance of VO_2 devices is increased by less than a factor of 10 by the sustained application (24 h) of 1 V gate voltage on water-containing DEME-TFSI, and after the removal of the gate voltage the conductance relaxes back down over the time scale of hours. In contrast, sustained positive gate voltage application above the metal−insulator transition results in a stable elevation of the room temperature conductance. To investigate the electrochemical doping process in the high temperature metallic phase, the device's temperature was ramped to 383 K and held for a certain time period with +1 V applied to the gate. Note that this bias is below the threshold ordinarily considered for extensive electrochemical splitting of water. Following this, the gate voltage was returned to zero and the device's conductance was measured upon cooling down to well below the transition. We repeated this process on a particular device, varying the holding period in the high temperature metallic state. With no gate voltage applied, there is no modification to the temperature dependence of the conductance relative to an untreated device. With a gate voltage of 1 V applied, while in the high-temperature metallic state there is no clear change in the conductance of the VO_2. However, after this high-temperature treatment, the conductivity of insulating phase stabilizes at a higher conductance upon cooling (figure 2.7). At high temperatures, the VO_2 still shows metallic behavior with a characteristic negative slope, dG/dT, of the temperature dependence of the conductance. We estimate that, with this sustained gate voltage application in the metallic state, the room-temperature conductance of the insulating phase can be increased by as much as 3 orders of magnitude relative to that of untreated VO_2. This large change in total conductance, comparable to that achieved in the full thermally driven metal−insulator transition in untreated beams, strongly suggests that the electrochemical doping at work here is a bulk effect, rather than just a surface accumulation layer as in ZnO.

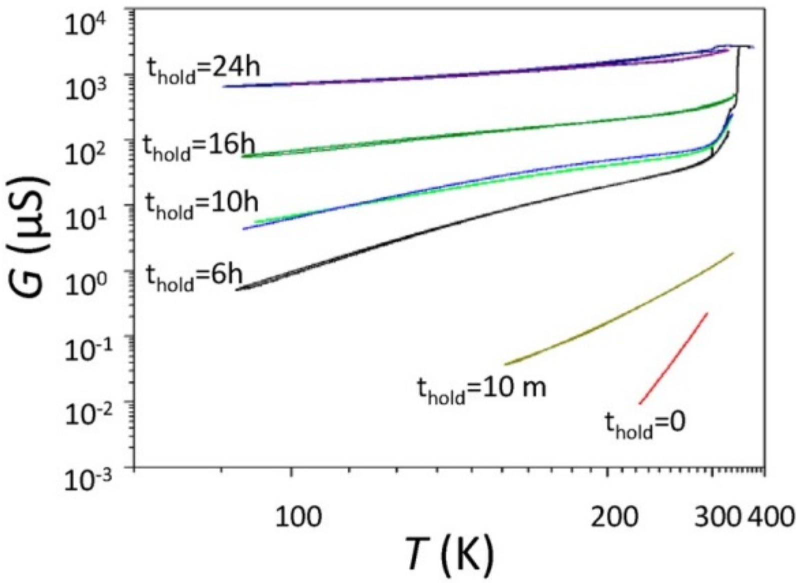

Figure 2.7 Temperature dependence of source–drain conductance at fixed source–drain AC bias voltage of 1 mV rms for an ensemble of otherwise identically prepared nanowire devices that are treated by heating at 383 K for different amounts of time (t_{hold}) with an applied gate bias of +1 V in the presence of a water-contaminated DEME-TFSI. Conductance and T are tick-marked in log scale and reciprocal scale, respectively. The red curve is the temperature dependence before any treatment. [21]

The insulating state after each thermal cycle presents a thermally activated conductance with activation energies (which can be extracted from the conductance−T data shown in Figure 2.7) that decrease with increasing hold times. Although the inferred activation energy can be significantly changed from~0.52 to 0.03 eV, it does not appear that VO_2 can be completely stabilized into the metallic phase (with negative *dG/dT*) by this method of electrochemical doping. In the insulating state, the inferred activation energy is the same upon warming as upon cooling. We also note that the increase of conductance due to this process is stable at room temperature; the high temperature treated devices do not show a time dependent relaxation of their conductance like the situation of low-temperature state displayed in Figure 2.6. A device gated in this manner in the metallic state will remain in the more conducting condition even with no gate voltage applied or with ionic liquid removed. This again indicates that it is an electrochemical doping process that changes the conductance of the VO_2 nanobeam, and the circumstances suggest that electrochemically produced hydrogen is the dopant.

The origin of the strong temperature dependence of the electrochemical doping was not immediately clear here. Possible contributions include the temperature dependence of the electrochemical splitting of contaminating water; the temperature dependence of the diffusion of dopants within the VO_2; or a special role of the high-temperature rutile structure. To answer this question, more experiments will be discussed in the following chapters.

2.6. Negative gate voltage

The reason to separate the negative gate voltage experiment from the discussion above is that these results are somewhat unrelated, though they support the hypothesis of a chemical reaction.

When a water-contaminated ionic liquid was used, sweeping the gate voltage to negative potentials relative to the source and drain near room temperature, and higher in magnitude, produced a significant Faradaic leakage current when V_g<-1 V.

If DC signal is used for source-drain measurement, such leakage current from gate electrode is large enough to affect the source-drain current (figure 2.8a). For the first several gate sweeps, the curves overlap, however, after repeating sweeps to negative V_g more than 10 times, or maintaining V_g at -2V for several minutes, the source–drain conductance gradually decreased, eventually reaching zero. An optical photo of the device after this measurement is shown in figure 2.8b (ionic liquid is rinsed off for clearer observation). The part of the beam covered by ionic liquid is dissolved, implying the presence of an electrochemical reaction. This is not surprising because it is known that VO_2 can be dissolved by chromium etchant (CR-7 from CYANTEK in this case, containing perchloric acid and ceric ammonium nitrate), a strong oxidizing solution. Although ionic liquid is chemically inert, the tiny amount of water dissolved in the liquid can play an important role here. When negative V_g is applied, an oxidization reaction occurs at the positive electrode, gradually etching the VO_2 electrode. Although the detailed chemical equation is beyond the scope of the discussion, it is almost certain that the negative gate voltage drives a redox reaction here.

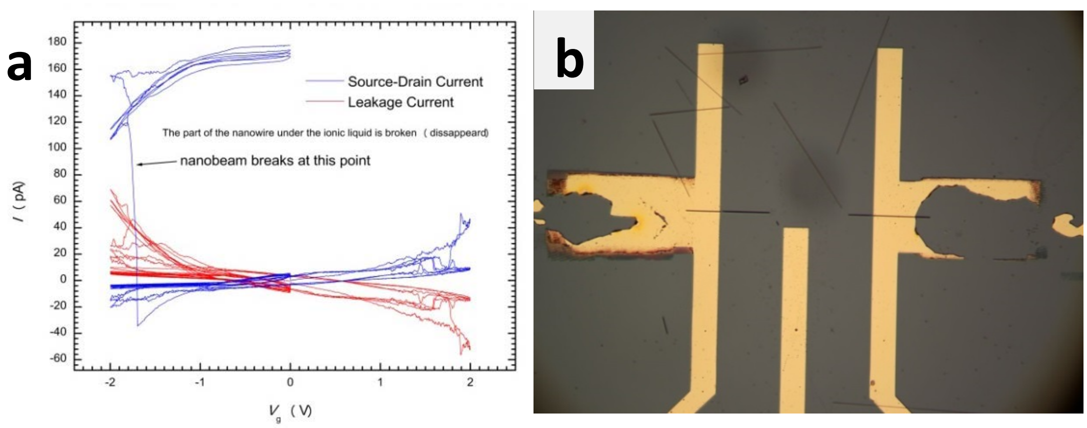

Figure 2.8 Effect of negative gate voltage. (a) Source-drain current as a function of gate voltage. The measurement starts with sweeping gate voltage on the negative side. After the source-drain current was gone, gate voltage began to be swept between -2 V to 2 V. (b) the photo of the device after measurement. Ionic liquid has been rinsed off, but the part of the beam previously covered by ionic liquid is disappeared.

2.7. Discussion and conclusion

With great care to avoid dissolved water and eliminate any electrochemical doping, we investigated the ionic liquid gating of VO_2 single-crystal nanobeam devices. Surprisingly, for devices incorporating nominally dry ionic liquid, no clear gating response in the temperature range of 340 to 150 K was observed. Using an ionic liquid as an electrolytic gating medium, induced surface charge densities of $\sim 10^{14}$ cm^{-2} at the liquid-VO_2 interface are expected. This surface charge density would correspond to an effective electric field of $\sim 10^9$ V/m in the vicinity of 1 nm at the interface. The absence of any detectable gating effect in the insulating state is surprising. Certainly some gate response would be expected for a conventional semiconductor with a band gap of ~0.6 eV, though surface states can affect the ability to induce mobile charge carriers. However, in a number of oxide systems with the carrier densities achievable with ionic liquids, surface states have not proven to be a significant problem. Near room temperature, thermally activated charge carriers are expected to lead to an extremely short electric screening length in VO_2, estimated by Ruzmetov et al. to be ~1 nm [13]. Such short-distance screening could explain the lack of a bulk electrostatic field effect within the nanobeams. However, one would expect to see some gate-driven change in the source–drain conductance if a high-density screening layer developed at the VO_2 interface, yet none is seen.

In summary, we attempted to use an ionic liquid as a gating medium for the field effect modulation of single-crystal VO_2 nanobeams. Despite what is expected to be an extremely large gated surface charge density, we observe essentially no gate response in devices using water-free ionic liquids. This was surprising and confirmed that the monoclinic, insulating phase of VO_2 should not be considered a conventional small-gap semiconductor. In contrast, in devices with gating media containing a source of hydrogen ions, we find strong, hysteretic gate dependence of the conduction with systematic that strongly suggests electrochemical doping (very likely hydrogen doping) of the bulk of the VO_2 material. While implying that a field-effect Mott transistor is not likely in this configuration of VO_2 single crystals, these results do suggest that chemical doping may be useful as a controlled means of engineering the properties of this and other oxide nanomaterials.

2.8. Similar works done by other groups following our experiment

Soon after the publication of our experiment, the group of Iwasa, who had successfully applied ionic liquid gating in other materials, published a paper in *Nature* [35], reporting a similar experiment of gating single-crystal VO_2 film grown on TiO_2 substrate. With results nearly identical to ours, the authors attributed the modulation of conductance of VO_2 to a pure field effect.

About half a year later, Jaewoo Jeong *et al.* published another paper regarding the ionic liquid gating on VO_2 in *Science* [36]. Again, they observed a very similar phenomenon with some key features mentioned in this chapter: the slow response to gate voltage, the large hysteresis loop of the Resistance-V_g curve, and the persistence of the modulation effect even after removing ionic liquid. They claimed that a field-induced migration of oxygen (oxygen vacancy) in VO_2 leads to the change of conductance of VO_2. Further, they suggested that the results of other similar experiments involving ionic liquid gating may be due to the same mechanism.

Considering the result of our experiment, we agree with the explanation of the latter paper more than that of the former. All the key features observed in the gating experiment strongly imply the presence of electrochemistry, although whether due to hydrogen doping, oxygen vacancy or both is still debatable. On the contrary, the interpretation based on field effect provided by the group of Iwasa cannot satisfactorily answer some important questions, e.g. the irreversibility of the gating effect.

Chapter 3

3. Hydrogenation of VO_2 nanobeams

Part of this chapter is reproduced from the published paper [37]:

Hydrogen stabilization of metallic vanadium dioxide in single-crystal nanobeams

J Wei, H Ji, W Guo, AH Nevidomskyy, D Natelson

Nature nanotechnology 7 (6), 357-362. DOI:10.1038/nnano.2012.70

3.1. Introduction

In chapter 2, we found the dramatic effect of chemical doping on VO_2 nanobeams, with all the evidence suggesting that hydrogen was the dopant. At the same time, we also encountered reports from other experiments that support this conclusion. The doping of VO_2 with hydrogen is similar to the intercalation of hydrogen in titanium dioxide (TiO_2) [34], which may also be accomplished by means of spillover[38], and involves the rapid diffusion of hydrogen atoms along the rutile c-axis in single crystals at moderate temperatures. Bulk vanadium dioxide hydride has been shown to be synthesized by electrochemical means, and hydrogen spillover [33, 39], using high temperature and high pressure, or by downward conversion from paramontroseite VO_2 at temperatures as high as 600 °C [40]. However, these experiments did not study the evolution of the metal–insulator transition (MIT) with doping in single crystals, the effect of strain on the resulting material, or the underlying physics behind the effect of the hydrogen atoms on the MIT. So, we decided to systematically study the effect of hydrogen doping in VO_2 nanobeams step by step, from the pristine case to the highly doped one. To achieve this goal, a new method requiring only hydrogen gas, a catalyst, and moderate temperature treatment (<200 °C) is introduced to fulfill the doping process.

3.2. Optical observation of catalytic effect

Following the ionic liquid gating experiment, we immediately realized the possible role of hydrogen. To rule out other factors which may occur in electrochemistry, we designed a treatment of VO_2 only involving hydrogen. A VO_2 nanobeam device with gold contacts, similar to those discussed in chapter 2, was put into a tube furnace setup, and baked at 180 °C with flushing forming gas (H_2:N_2 = 1:4) in room pressure. After treatment for 12 hours, the VO_2 device showed a much reduced resistance at room temperature, where it should be an insulator in the pristine state. Also, after the sample was taken out of the tube, no detectable change of conductance was observed within several hours, meaning that the enhanced conductance persisted at room temperature in air. However, on a device, which had its gold contacts deposited after the hydrogen treatment of VO_2 nanobeam, the conductance did not exhibit any enhancement compared to pristine VO_2. This implied that the order of treatment and fabrication matters, and thus led us to consider a possible catalytic effect caused by the gold contacts. To further investigate this issue, we used optical microscopy to directly observe selected wide VO_2 wide beams.

On a substrate with dense VO_2 sheets and beams grown on top, a 20-nm-thick gold film was patterned and deposited by e-beam evaporation. Among the numerous VO_2 crystals along the edge of the gold pattern, two samples partially covered by gold were selected for observation and are shown in the two rows of figure 3.1. At room temperature, they are in the monoclinic phase (figure 3.1a, d), while well above the transition temperature, they are in the fully metallic state (figure 3.1b, e). The transition can be clearly characterized from the color change and the Raman spectra in the low- and high-temperature states. This particular substrate was then treated using the hydrogenation process described above. Figure 3.1c,f shows the samples at room temperature after the treatment. In figure 3.1c, the whole sample became darker than its pristine room-temperature color, and similar to its pristine metallic state color. In figure 3.1f, a similar dark color also developed at the end in contact with the gold, but only extended to the middle of the beam, forming a sharp boundary between the dark color region and a light one. Crystals not in contact with the gold metal remain unchanged (not shown). Control experiments were performed by baking in argon, helium, nitrogen and vacuum environments, resulting in no change in the VO_2 properties. A similar change in coloration was observed for crystals contacted by copper, nickel and palladium films and then exposed to hydrogen gas at similar temperatures. The extent of the color-changed region was maximal for palladium, and was observed with hydrogen exposure at temperatures as low as 90 °C. We argue that the darker region is the result of hydrogenation of the VO_2 crystals by means of spillover. When warming the hydrogenated sample through the transition temperature, the darker regions show no noticeable transition in color contrast, but the un-contacted crystals and the brighter regions on the contacted crystals still have a phase transition with the typical optical contrast change, as before.

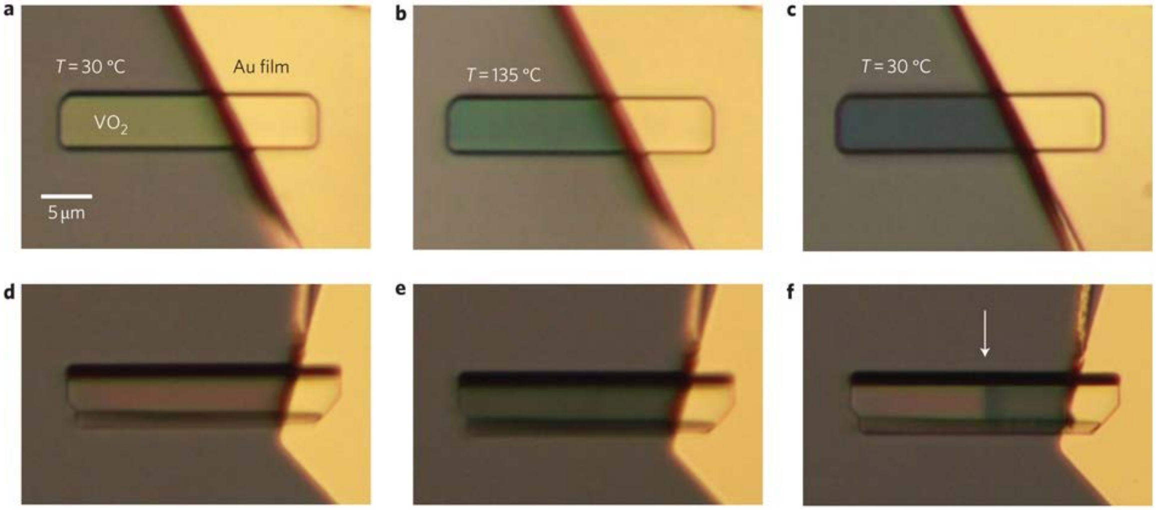

Figure 3.1 Optical images of faceted VO_2 crystals with thicknesses of ~300 nm (a–c) and ~600 nm (d–f) on an oxidized silicon substrate taken at 30 °C (a,d) and 135 °C (b,e) and at 30 °C after hydrogenation (c,f). The brighter region is a 20 nm gold film

deposited to cover parts of the crystals. The scale bar in (a) applies to all six images. All of the ~300 nm crystal is converted into an apparently metallic phase (c), and a sharp phase boundary can be seen for the ~600 nm crystal (indicated by the arrow in f). [37]

3.3. Crystal characterization

Although optical observation is a direct and convenient method to help us build a basic concept for the hydrogenation process, it cannot provide a reliable analysis for the hydrogen doped region. To examine the hydrogenated VO_2 nanobeams in detail, three characterization methods were used. (Further quantitative structural characterization through collaborative x-ray and neutron diffraction studies will be discussed in Chapter 5).

3.3.1. Raman spectroscopy

Pure VO_2 crystals at room temperature exhibit the Raman spectrum (black curve in Figure 3.2) of the monoclinic structure[41], with additional peaks at 521 and 302 cm^{-1} from the silicon substrate. At 135°C, the Raman spectrum (red curve in Figure 3.2) of untreated VO_2 is dominated by featureless luminescence[42] arising from the recombination of photo-excited carriers. The spectrum from the darker regions (green curve in Figure 3.2) of hydrogen-treated VO_2 at room temperature closely resemble that of the high-temperature, metallic, untreated VO_2.

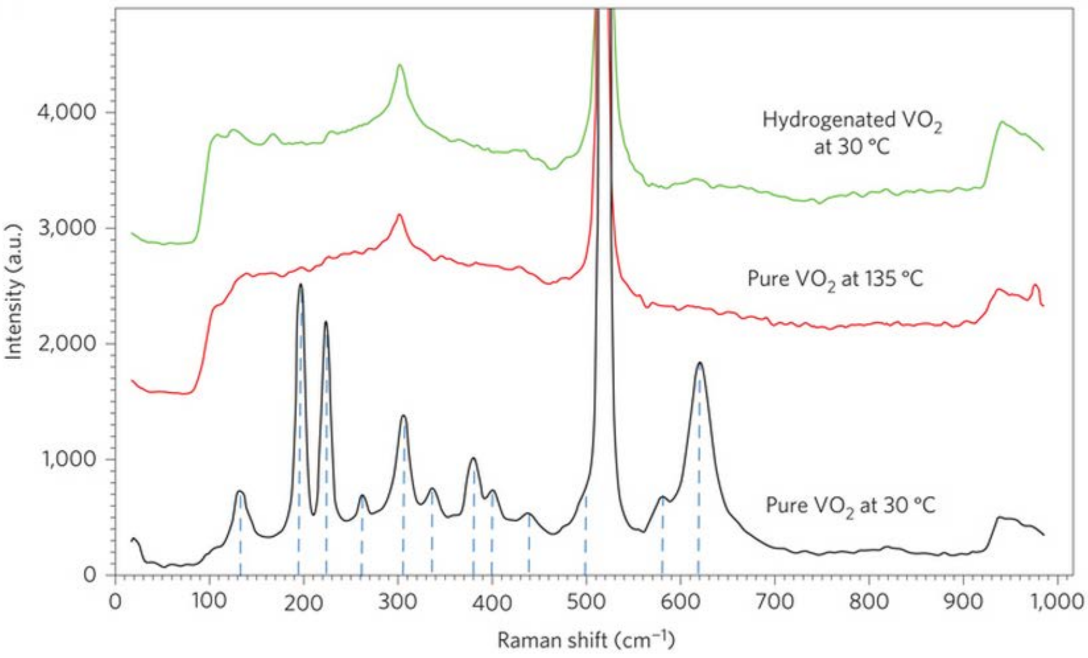

Figure 3.2 Raman spectrum of a pure VO2 crystal at 30 °C (black line) and 135 °C (red) and of hydrogenated VO2 at 30 °C (green). Raman peaks at 132, 199, 225, 305, 392, 500, 582 and 618 cm^{-1} correspond to A_g symmetry, and those at 265, 339, 400 and 440 cm^{-1} are of B_g symmetry. The strong peak at 520 cm^{-1} is the Raman line of the silicon substrate. [37]

3.3.2. SAED in TEM

To identify the crystal structure of the darker region, we performed selected area electron diffraction (SAED) on several suspended single-crystal VO2 nanobeams. We discuss a representative example here, which is grown protruding over the edge of the substrate. A layer of 5 nm palladium was then deposited on the top surface of the substrate, overlapping with the anchoring point of the beam (figure 3.3a).

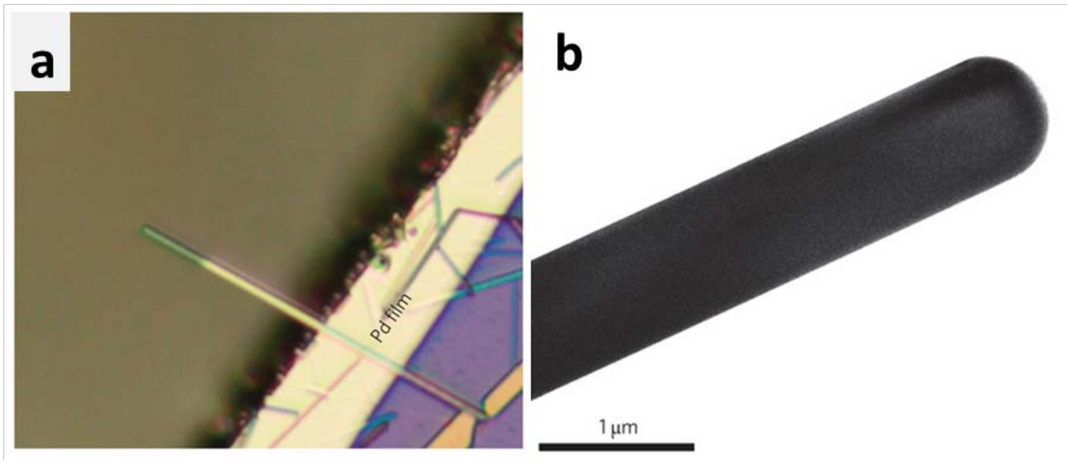

Figure 3.3 (a) Optical micrograph of a cantilevered VO_2 nanobeam partially coated with 5 nm of palladium (yellow region). (b) Bright-field TEM image of the cantilevered VO_2 nanobeam after hydrogenation. No obvious non-uniformities are seen. [37]

Bright-field transmission electron microscopy (TEM) images and SAED patterns were obtained for the nanobeam as grown, and again following exposure to hydrogen under the same condition mentioned previously. The initial SAED pattern is consistent with an incident electron beam along the $[1\bar{2}2]$ direction of the monoclinic structure and a longitudinal growth direction of the nanobeam along the rutile [001] c-axis, as reported previously[4] (figure 3.4a). Following hydrogen exposure, at room temperature the color of the hydrogenated overhanging part of the VO_2 nanobeam turns darker. Along the same incident electron-beam direction, the SAED pattern changes from rectangular symmetry before hydrogenation to a different symmetry (figure 3.4b). The post-hydrogen diffraction pattern is indexed as the [111] axis of either the rutile structure of pure VO_2 with space group P21/c(14) (tetragonal, which $a=b\neq c$), or the orthorhombic structure (also rutile, but a≠b≠c) previously reported for hydrogenated H_xVO_2 (x = 0 to 1) with space group Pnnm(58)[39]. There is not enough resolution to distinguish between the tetragonal structure of pure VO_2 and orthorhombic H_xVO_2 from these SAED patterns alone. From the bright-field TEM image (Figure 3.3b), the VO_2 single-crystal nanobeam remains crystalline after hydrogenation, with no visible amorphous structure on the surface.

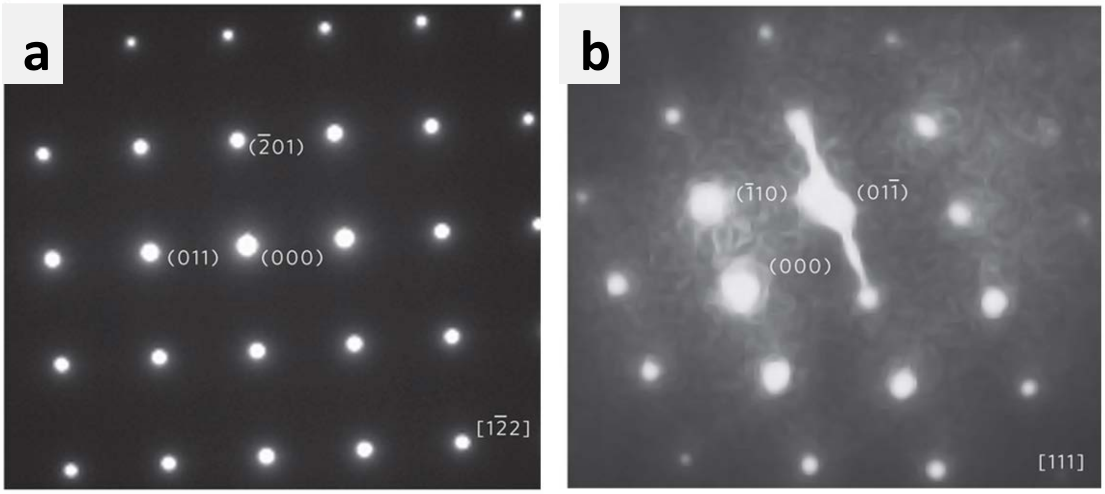

Figure 3.4 (a) SAED pattern of the pure VO_2 cantilever indexed as a monoclinic structure on the zone axis direction. (b) SAED pattern of hydrogenated VO_2 cantilever indexed as an orthorhombic structure on the zone axis [111] direction. [37]

3.3.3. X-ray photoemission spectroscopy (XPS)

Dr. Bo Chen helped on the XPS measurement in this experiment. For XPS examination, a dense film of VO_2 single-crystal nanobeams and sheets was grown directly on an oxidized silicon substrate, which was then coated with a discontinuous film of 0.5-nm-thick Pd to act as the catalyst metal for the hydrogenation process. XPS scan (using a PHI Quantera x-ray microprobe system, base pressure of 5×10^{-9} Torr, takeoff angle of 45 degrees, beam diameter of 100 μm) was conducted before and after the sample was hydrogenated at 200 °C for 2 hours. The full photoemission spectrum is shown in Figure 3.5a. On the surface of the sample, we expect elements of V, O and Pd which can be clearly identified in the spectrum. Adventitious carbon with C1s level at 285eV was used to calibrate the binding energy, to confirm that all the peak positions in the spectrum are accurate.

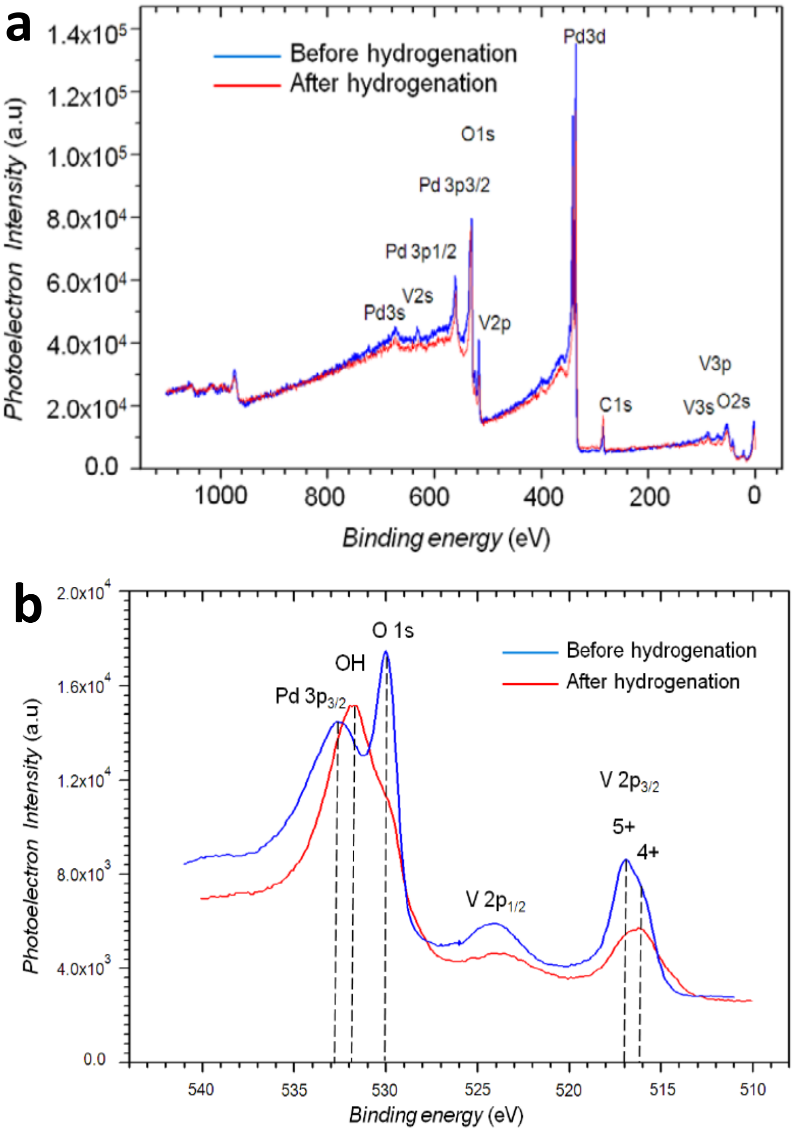

Figure 3.5 (a) Full XPS spectrum of VO_2 sample with 0.5nm Pd coating before (blue line) and after (red line) hydrogenation. (b) XPS spectrum with binding energy at range of 545 to 510 eV for a plate-like VO_2 crystal (micron-scale transverse dimensions, approximately 500 nm thickness) sample with 0.5 nm Pd coating before (blue line) and after (red line) hydrogenation. [37]

Figure 3.5b shows a magnified view of a portion of spectrum over the binding energy range from 545 to 510 eV. Before hydrogenation, the V $2p_{3/2}$ feature is a superposition of a dominant V^{+5} peak and smaller V^{+4} peak. The peak position for V^{+5} is at 517 eV, which is 0.9 eV higher than the V^{+4} peak at 516.1eV [43, 44]. The prominent V^{+5} peak indicates that the crystals have a surface layer of further oxidized V_2O_5. (We note that in other samples briefly treated with buffered oxide etch, the V^{+5} peak does not appear, consistent with etching away of the surface oxide.) After hydrogenation, V^{+4} is the dominant peak, with diminishing V^{+5} signature. There is no distinguishable peak from V^{+3} (to be expected at 515.8 eV[45]). The overall peak of V $2p_{3/2}$, which can be explained by the various configurations of the photoemission final states, originates from the core-hole 3d electrons interactions. The intensity ratio between V and O remains unchanged, and the XPS software interprets the V to O composition ratio at 1:2 both before and after hydrogenation. Comparison of the V $2p_{3/2}$ peaks before and after hydrogenation indicates that vanadium in the VO_2 crystals remains at +4 valence state.

There is a clear Pd $3p_{3/2}$ peak at 532.6 eV[46] before hydrogenation. After hydrogenation, this peak is considerably reduced, as is the O 1s peak, and a new peak appears at 531.7 eV, which is 1.7 eV higher than O1s peak position at 530 eV. According to many previous results [44, 47, 48], this 531.7eV peak is consistent with the existence of O-H bonds after the hydrogenation process. The relative intensity of this peak is much larger than oxygen O 1s peak, which argues against O-H contamination on the surface. This is strong evidence of diffused hydrogen forming stable O-H bonds, where the same situation can be found in the hydrogenated TiO_2 system [47, 48].

3.4. Transport measurements

To examine electronic transport in hydrogenated VO_2 we fabricated two-terminal nanobeam devices with gold contacts and measured the temperature dependence of electrical conductivity following different hydrogenation conditions. To minimize the effects of strain, nanobeam devices were suspended by means of substrate etching as described in chapter 1. The length of the suspended beam recovered to the natural length of the monoclinic phase, and thus expanded ~1% longer along the growth direction, i.e. c_R-axis or a_M-axis. The scanning electron microscopy (SEM) image (figure 3.6a) shows the buckled nanobeam due to release of the strain.

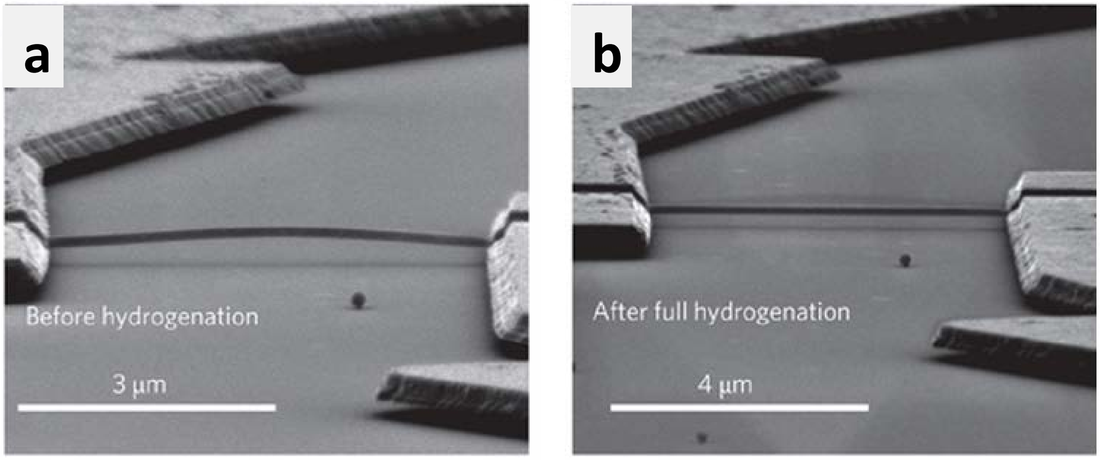

Figure 3.6 Scanning electron micrographs showing a suspended VO_2 nanobeam device (b) before hydrogenation and (c) after hydrogenation into the fully metallic state. [37]

Before hydrogenation, the electrical conductivity (black curve in figure 3.7a) shows a three order of magnitude drop at the metal–insulator transition. The energy gap extracted from the plot for the insulating phase is consistent with previously reported results (~0.6 eV). We then conducted a series of hydrogenation treatments at 150 °C, 180 °C and 190 °C respectively, measuring conductivity versus temperature after each. We found that hydrogenation has only a small effect on the transition temperature until the transition vanishes entirely. After a final hydrogenation at 190 °C for 20 min, the device became fully metallic (purple trace) at room temperature, with no sign of the MIT, and the metallic state persisted down to 4.2 K. The disappearance of the MIT and the negative temperature dependence slope of the conductivity strongly suggest the metallic nature of fully hydrogenated VO_2. At the same time, the SEM image shows that the VO_2 nanobeam becomes straight after hydrogenation to the fully metallic state (figure 3.6b). This demonstrates visually that the fully hydrogenated nanobeam has a shorter lattice constant than monoclinic VO_2 along the growth direction, identical to the unbuckling of suspended pure VO_2 beams following thermal transition to the rutile metallic. The straight lines in the conductivity versus temperature plots (the dashed lines in figure 3.7a) are evidence for simple activation behavior and suggest homogeneous electronic properties of the beam once in the low-T state. The hydrogenated highly conducting state is stable in air for weeks, however, the blue trace, taken after baking the device in air at 250 °C for 20 min, shows that the hydrogenation process is completely reversible. Another series of repetition of hydrogenation and dehydrogenation processes has been shown in figure 3.7b as supplementary information.

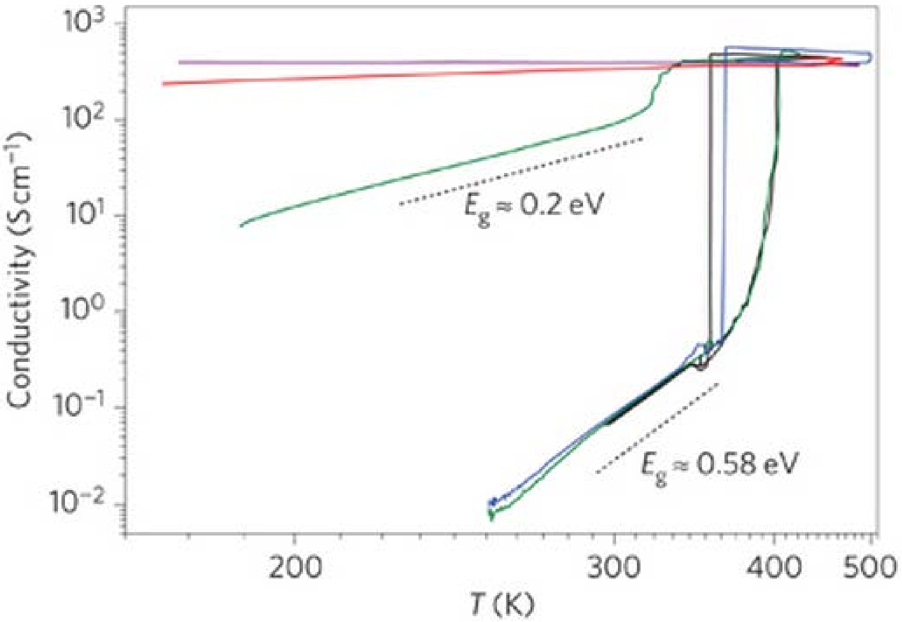

Figure 3.7 Conductivity (on a log scale) versus temperature (on a scale in which the spacing varies as 1/T) for a suspended nanobeam device. Before hydrogenation (black curve) the device shows thermally activated conduction consistent with an energy gap close to 0.6 eV. The device was then baked in flushing hydrogen gas at 150 °C for 20 min and shows an energy gap close to 0.2 eV (green). After further baking at 180 °C for 20 min (red) the energy gap is nearly zero. After baked at 190 °C for 20 min, the device is eventually stabilized in the metallic state with a characteristic negative slope (purple). Baking the device in air at 250 °C for 20 min recovered the original phase transition and temperature dependence (blue curve). [37]

We also found that, though most of the VO_2 nanobeam devices could be doped into a fully metallic state, some variation existed. Figure 3.8 shows the measurements of a group of devices after the same etching process (BOE for 3 minutes) and hydrogenation treatment (180 °C for 24 hours). There was no particular beam selection process used, beyond the basic requirement that the beams should have no obvious morphological defects and should be isolated from neighboring crystals on the substrate. Based on AFM and SEM analysis, there is no obvious difference between these beams; however, the temperature dependence of their two-terminal conductance following hydrogenation shows remarkable variability. Some show metallic temperature dependence, some show non-monotonic temperature dependence with a small change in conductance, while other devices exhibit very insulating character at low T. It is known from past work that the amount of residual strain in each crystal varies, depending in detail on how that particular beam interacted with the substrate during the growth process and subsequent cooling. With this amount of etching, some of the crystals remained unintentionally in contact with the underlying substrate, with an uncontrolled amount of residual strain. Such strain might affect the hydrogenation result by either creating an un-doped/less-doped region or modulating the properties of certain doped regions.

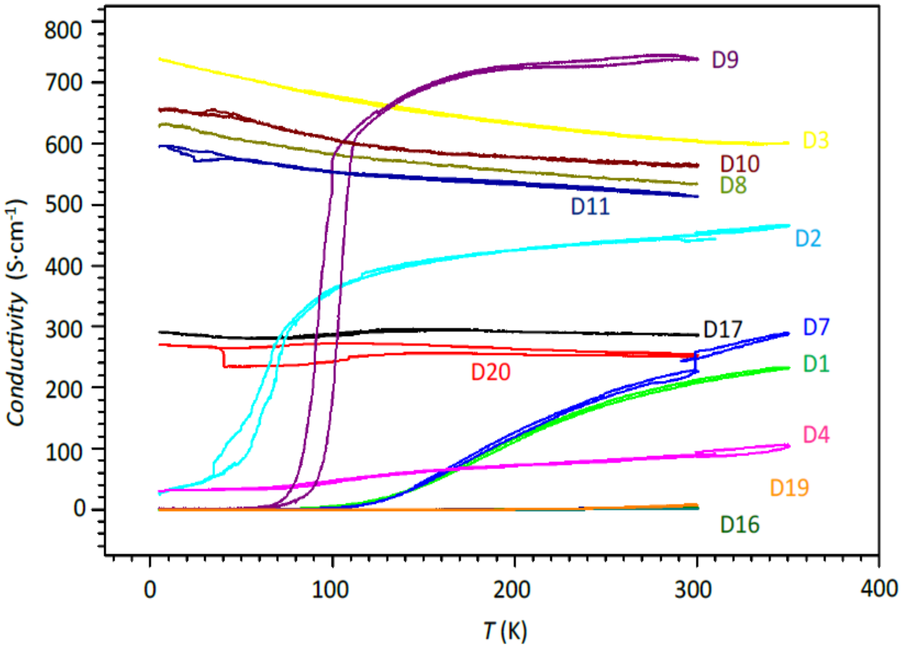

Figure 3.8 Temperature dependence of conductivity for a collection of hydrogenated VO_2 nanobeams still attached (to varying degrees from device to device) to the underlying oxidized Si surface. [37]

3.5. *Ab initio* calculations

Due to the small size of hydrogen atoms, or protons if they exist as ions, it is difficult to experimentally determine their local concentration and positions in the hydrogenated VO_2. Therefore, physical insight from theoretical electronic structure calculations is valuable. The *ab initio* calculations allow one to judge the relative thermodynamic stability of the competing crystallographic phases. Such structural and thermodynamic results tend to be reliable, even for strongly correlated charge transfer and Mott insulators such as the 3d-metal monoxides MnO and NiO [49, 50], where density functional theory (DFT) methods face significant challenges[18].

In this work, the *ab initio* calculations were completed by the group led by Professor Andriy H. Nevidomskyy, so, in my thesis, I will omit most details of the calculation method, focusing instead on discussion of the results.

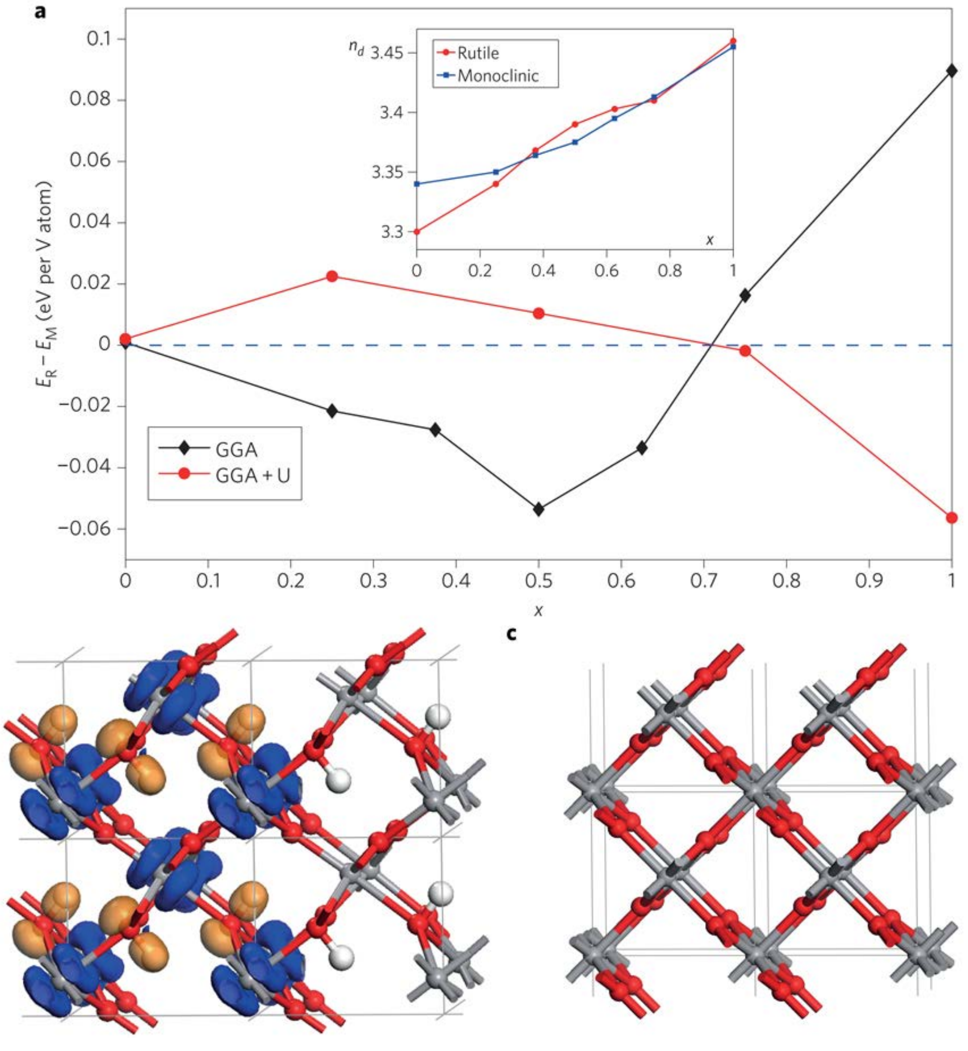

Figure 3.9 (a) Energy difference per atom between the hydrogenated pseudo-rutile phase (R) and the monoclinic phase (M) as a function of hydrogen concentration x in H_xVO_2, calculated using the GGA (black diamonds) and GGA + U methods (red circles: $U_{eff} = 3.4$ eV, see text). The lines are a guide to the eye. The inset shows the Mulliken d-orbital occupancy n_d as a function of hydrogen concentration for the GGA-optimized monoclinic (blue) and rutile (red) structures. (b) Atomic structure of the pseudo-rutile phase of $H_2V_4O_8$ ($x = 0.5$). Oxygen atoms are shown in red,

vanadium in grey and hydrogen in silver. The isosurfaces of the vanadium d-bands at the Fermi level are shown in blue, and the isosurface of the bonding H...O orbital, situated about −8.1 eV below E_F, is shown in orange. (c) Undistorted rutile structure of VO_2. [37]

Using a variety of initial hydrogen positions and comparing the total energies of optimized structures within DFT, Dr. Nevidomskyy found that the proton favors the position in the center of the open channel in the structure (shown in Figure 3.9b), forming a strong H..O bond with one of the oxygen atoms. The same conclusion was reached by a number of experimental and theoretical studies in hydrogen-intercalated rutile TiO_2 [51]. The typical H...O bond length is very short, ranging between 0.99 and 1.03 Å, and the electron density associated with this bonding orbital is plotted in orange in Figure 3.9b, maximal on the H...O bond. The resulting pseudo-rutile structure (Figure 3.9b) is distorted compared with the pristine rutile phase of VO_2 (Figure 3.9c). Moreover, the VO_2 lattice expands due to hydrogen intercalation in both the rutile and monoclinic structures.

To elucidate the experimentally observed transition towards metallic behavior in the conductivity on hydrogenation, Dr. Nevidomskyy analyzed the trends in the DFT-calculated total energy of the pseudo-rutile and monoclinic phases. These show that the hydrogenated pseudo-rutile structure is energetically favorable over the monoclinic one for a wide range of hydrogen doping ($x<0.7$ per formula unit, H_xVO_2), with the most energetically advantageous population at $x = 0.5$ (Figure 3.9a, black diamonds). The simulated diffraction patterns of this theoretical structure are consistent with those in Figure 3.4b. The generalized gradient approximation (GGA)-DFT predicts this pseudo-rutile structure to be metallic, with the density of states (DOS) at the Fermi level dominated by vanadium d-bands (Figure 3.10a), similar to the pristine rutile VO_2 (Figure 3.10b). The electron charge density of this conduction d orbital is plotted in blue in Figure 3.9b.

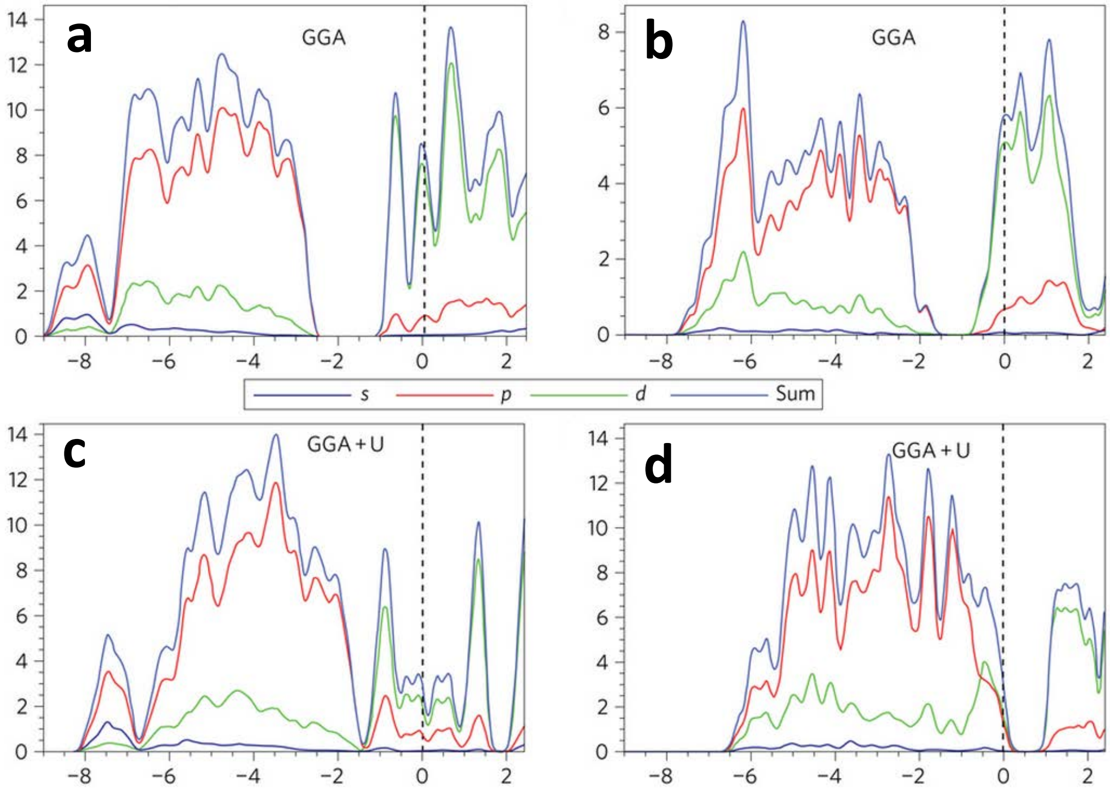

Figure 3.10 PDOS of $H_2V_4O_8$ calculated with (a) the GGA method and (c) the GGA + U method, and for pure VO_2 calculated with the same two methods (b and d, respectively). [37]

To improve the treatment of electronic correlations in our DFT calculations, Dr. Nevidomskyy has taken the Hubbard on-site repulsion U into account within the so-called GGA+U approximation. Although not exact, this captures to some extent the tendency towards interaction-driven electron localization. More sophisticated methods are not applied here due to computational complex induced by extra hydrogen atoms in large multiformula-unit supercells. The total energies of the GGA+U calculations are plotted as red circles in Figure 3.9a and show a different tendency, with a threshold of $x \approx 0.7$ above which the pseudo-rutile structure becomes energetically favored over the monoclinic one. Unlike the pristine VO_2, which is predicted to be an insulator within GGA+U (Figure 3.10d), the hydrogenated structures (both pseudo-rutile and monoclinic) are metallic, with a non-vanishing DOS at E_F dominated by vanadium d-bands (Figure 3.10c). This leads to the qualitative conclusion that for a fixed value of Hubbard U, hydrogen intercalation moves VO_2 away from the MIT, predicting the material to be a metal.

The tendency towards metallicity in hydrogenated VO_2 can be understood schematically in the following simplified picture. The formation of a strong H..O bond is accompanied by electron transfer from hydrogen onto the oxygen atom, effectively reducing the electronegativity of the latter. This in turn makes the V..O bond less ionic, resulting in higher vanadium d-level occupancy and consequently more metallic behavior. This is confirmed by the present calculations, which show that hydrogen doping changes the d-orbital occupancy by as much as 0.16 electrons at $x = 1$ (Figure 3.9a, inset). This perturbation away from half-filling would be a strong push away from the Mott MIT and would provide an explanation for the observed metallicity in the hydrogenated VO_2 on the basis of the Mott picture. Moreover, the expansion of the unit cell volume would result in a significantly reduced overlap between the electron shells of neighboring vanadium atoms, thereby suppressing the tendency towards Peierls dimerization. As a result, Dr. Nevidomskyy concluded that hydrogenation achieves metallicity by disfavoring both the Mott and Peierls mechanisms. This picture is in line with the emerging consensus from previous theoretical studies that the MIT in pure VO_2 is neither purely Mott nor purely Peierls, but is rather a hybrid correlation-assisted Peierls transition, involving both on-site interactions and dimerization between neighboring vanadium atoms [17-19].

3.6. Conclusion

We reported the hydrogenation of individual VO_2 nanobeams and other microcrystals starting from pure VO_2, and we discuss optical measurements, structural characterization and electronic transport. These experiments allowed us to examine the doping process in detail, to consider its reversibility, and to explore the evolution of the MIT. With progressively longer exposure to hydrogen, the energy gap inferred from electron transport measurements was reduced and the MIT is suppressed, without a significant shift in the MIT temperature, and the conductivity of the low-temperature insulating phase evolves from thermally activated to a fully metallic temperature dependence. Ab initio calculations and structural measurements suggest that this new metallic state has an orthorhombic structure that is similar to the original rutile structure.

Chapter 4

4. Diffusion of hydrogen in VO_2 by atomic hydrogenation

Part of this chapter is reproduced from the published paper [20]:

Hydrogen Diffusion and Stabilization in Single-Crystal VO2 Micro/Nanobeams by Direct Atomic Hydrogenation

Jian Lin, Heng Ji, Michael W Swift, Will J Hardy, Zhiwei Peng, Xiujun Fan, Andriy H Nevidomskyy, James M Tour, Douglas Natelson

Nano Letters, 2014, 14 (9), pp 5445–5451. DOI: 10.1021/nl5030694

4.1. Introduction

In the previous chapter, we confirmed the effect of hydrogen doping on the electronic properties and phase transition of VO_2. Based on the *ab initio* calculations and analogue example of rutile TiO_2, it is reasonable to infer that hydrogen exists in form of atoms or ions in VO_2. The high rate of hydrogen doping in the presence of palladium (Pd) supports this conjecture, too, because Pd is a catalyst well-known for its high efficiency of splitting hydrogen molecules into atoms in the spillover method. However, the requirement of a catalyst limits the applications of this material, and also complicates the research of intrinsic features of the hydrogenation process. For example, it remained unclear whether the elevated temperature is required to enhance the kinetics of the catalyst, to thermally enhance the diffusivity of the resulting atomic hydrogen, or to determine whether the rutile crystal structure is of critical importance to the rate of the diffusion process. Another unsolved question due to the presence of catalyst was whether the distribution of catalyst on the surface of VO_2 nanobeam affects the outcome.

So in this chapter, we will introduce a new technique, the atomic hydrogenation process, which does not require any catalyst, to eliminate unknown catalytic kinetics and allow hydrogen equal access to all crystallographic surfaces. Then we can study the kinetics of hydrogenation of VO_2, and compare the diffusion rate of hydrogen in the monoclinic and rutile phases.

4.2. Atomic hydrogenation

Figure 4.1 shows the photo and scheme of the tube furnace setup used for atomic hydrogenation process. In the tube, hydrogen gas is flown in at a rate of 100cc/min, a tungsten filament heated by a 45W power supply is located in the middle of the tube, and samples to be hydrogenated sit 1 cm away from the filament on the downstream side. A valve on the pumping side is adjusted to stabilize the tube pressure at 10 Torr. The furnace can control the ambient temperature from room temperature to 200 °C. During the process, the hot filament splits hydrogen molecules into hydrogen atoms, and if the atomic hydrogen can diffuse easily in VO_2, the direct exposure to H atoms can cause hydrogen doping driven by a concentration gradient.

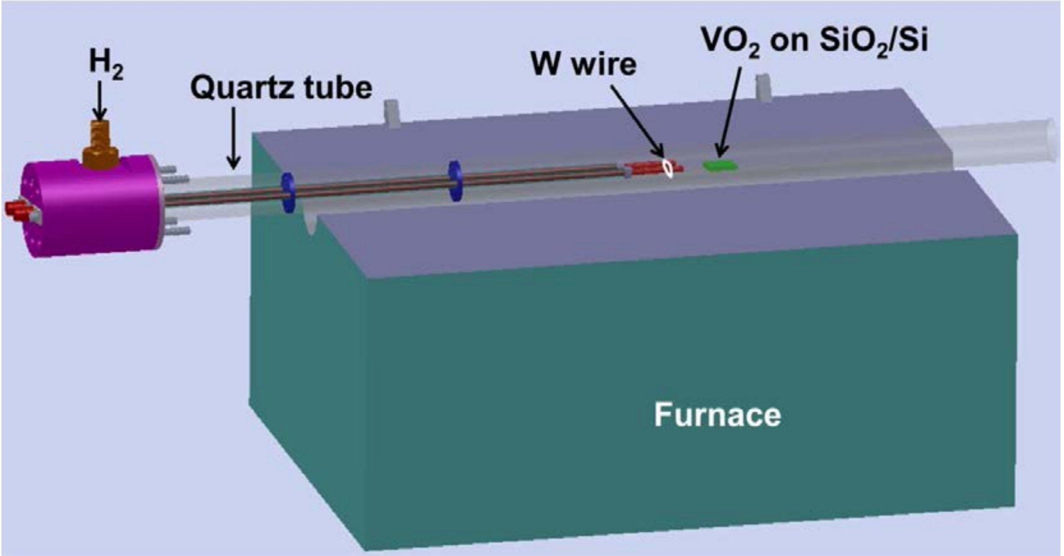

Figure 4.1 Schematic of experimental setup for the hydrogenation of VO_2 using atomic hydrogen generated by the hot filament. [20]

The VO_2 nanobeams used in this experiment are the same as before: PVD growth on silicon wafers with 2 μm thermal oxide. The growth direction is their rutile [001] direction (i.e. c_R-axis, or a_M-axis for monoclinic phase). Again, to minimize the strain, nanobeams were released from the substrate by BOE etching, and subsequently transferred to a carrier Si/SiO2 substrate. The beams exhibited the insulating state with monoclinic structure below the MIT temperature of ~340 K as determined by visual observation of the color (Figure 4.2a). When the temperature was increased (usually to 370K) the beams turned into the fully metallic state with rutile structure, as inferred from the color change in Figure 4.2b. This same sample was hydrogenated by direct exposure to atomic hydrogen generated by a hot filament for 5 minutes, with the sample temperature maintained at 373 ± 10 K, followed by being cooled to room temperature in the absence of hydrogen. Figure 4.2c shows distinct regions of darker color on both ends of the VO_2. These regions are in a hydrogen-stabilized metallic state, as observed through their differing optical contrast and Raman spectra. This partial conversion of the beams to a hydrogen-stabilized metallic state agrees well with the results seen when catalytic spillover is used to introduce hydrogen at the ends VO_2 nanobeams. In contrast to the spillover situation, in this case, atomic hydrogen had access to all exposed faces of the beam. On the basis of optical signatures of the beam state, hydrogen diffusion in directions transverse to the beam growth direction (i.e., normal to the beam sidewalls) is clearly far slower than diffusion along the beam growth direction from the exposed ends of the beam. Such anisotropy in diffusion is reminiscent of the diffusion of atomic hydrogen in the isostructural rutile TiO_2 [52]. After the VO_2 nanobeams were hydrogenated under identical substrate temperatures and gas flow for times approaching 15 min, the dark blue regions on both ends extended toward each other and fully occupied the beams (Figure 4.2d).

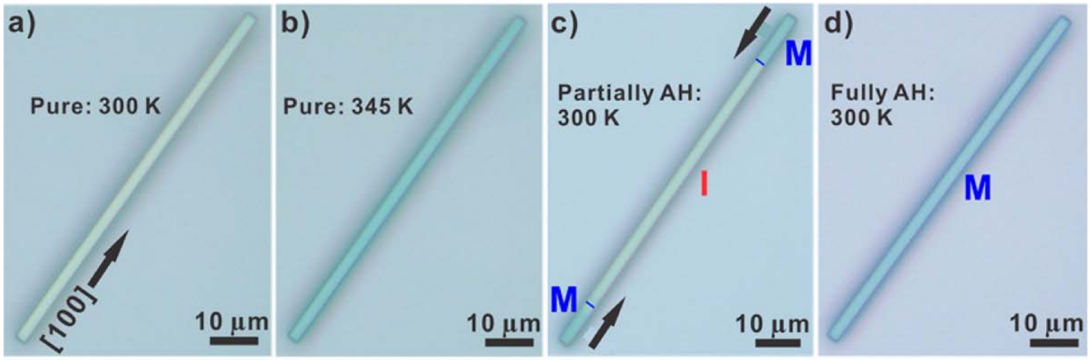

Figure 4.2 Optical photos of VO_2 nanobeams. (a) Optical image of pure VO_2 taken at 300 K. (b) Optical image of pure VO_2 taken at 345 K. (c) Optical image of VO_2 taken at 300 K after hydrogenation at 100 ± 10 °C for 5 min. Lines have been drawn to indicate clearly the boundaries between metallic domains (propagating in from the ends) and the insulating central region. (d) Optical image of VO_2 taken at 300 K after hydrogenation at 100 ± 10 °C for 15 min [20]

4.3. Characterization of hydrogenated VO_2 nanobeam

Raman spectroscopy, selected area electron diffraction (SAED), and transport measurement are again done in this experiment to characterize the properties of hydrogenated VO_2 nanobeam. All the results agree well with those in Chapter 3, so here I will simply present the data and briefly describe them.

Figure 4.3 gives the Raman spectrum data. The Raman spectrum of the as-grown VO_2 (black curve) exhibits distinct peaks at 196, 222, 262, 337, 379, and 623 cm^{-1} with additional peaks due to the silicon substrate at 302 and 521 cm^{-1}, indicating the stable monoclinic phase (M1) at room. The full width at half-maximum (fwhm) of the particular peak (indicated by an asterisk) at 623 cm^{-1} is 23.4 cm^{-1}. When the VO_2 nanobeam was partially hydrogenated as shown in Figure

4.2c, the Raman spectra from the distinct regions show different characteristics. The Raman spectrum taken from the light colored central region of the beam (red curve) is similar to that of the M1 phase. However, the indicated peak shifted to 637 cm^{-1} and its fwhm increased to 46.8 cm^{-1}. This expansion of certain peak was not seen in the result in Chapter 3, and thus may be an indication of a light doping on the surface, which could not happen in the previous experiment due to lack of contact to the metal catalyst. The Raman spectrum from the dark colored regions of the hydrogenated VO_2 nanobeam (blue curve) is dominated by weak and broad bands, resembling spectra of VO_2 in the rutile phase. Baking a previously fully hydrogenated VO2 nanobeam in air at 250 °C for 20 min restores its Raman spectrum to be nearly identical to that of the as-grown monoclinic state, indicating excellent reversibility of the atomic hydrogenation.

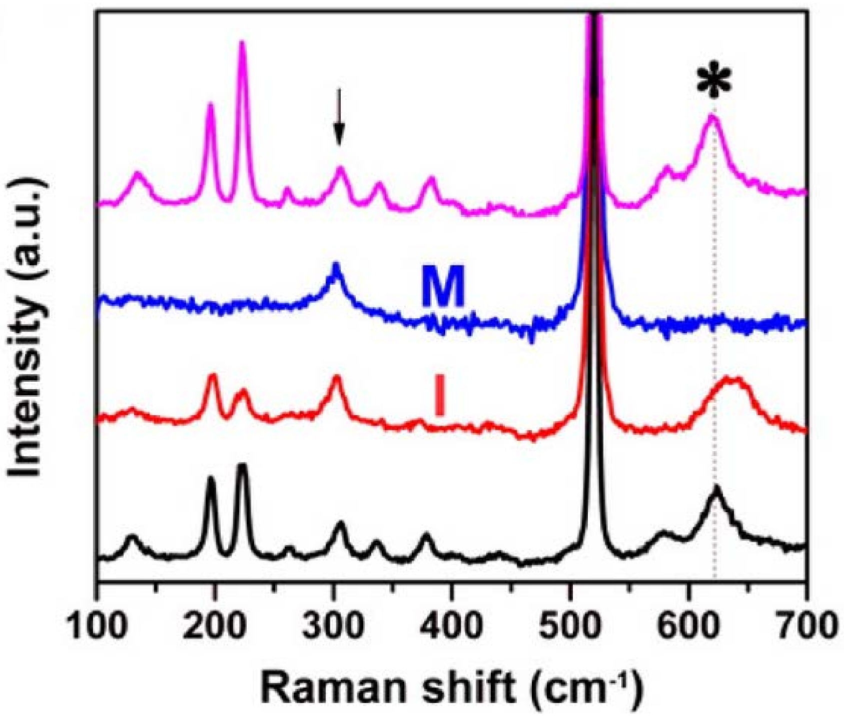

Figure 4.3 Raman spectra of pure VO_2 crystals (black); of the light-colored regions of the hydrogenated VO_2 (labeled as “I” in figure 4.2(c), red); of the dark-colored regions of the hydrogenated VO_2 (labeled as “M” in figure 4.2(c) and figure 4.2(d), blue); of hydrogenated VO_2 after baking in air at 250 °C for 20 min (magenta). All of the spectra were taken at 300 K. [20]

TEM images and corresponding SAED patterns of VO_2 nanobeams before and after hydrogenation are shown in Figure 4.4. They all agree well with the result in Chapter 3, exhibiting highly crystalline with no visible nonuniformity.

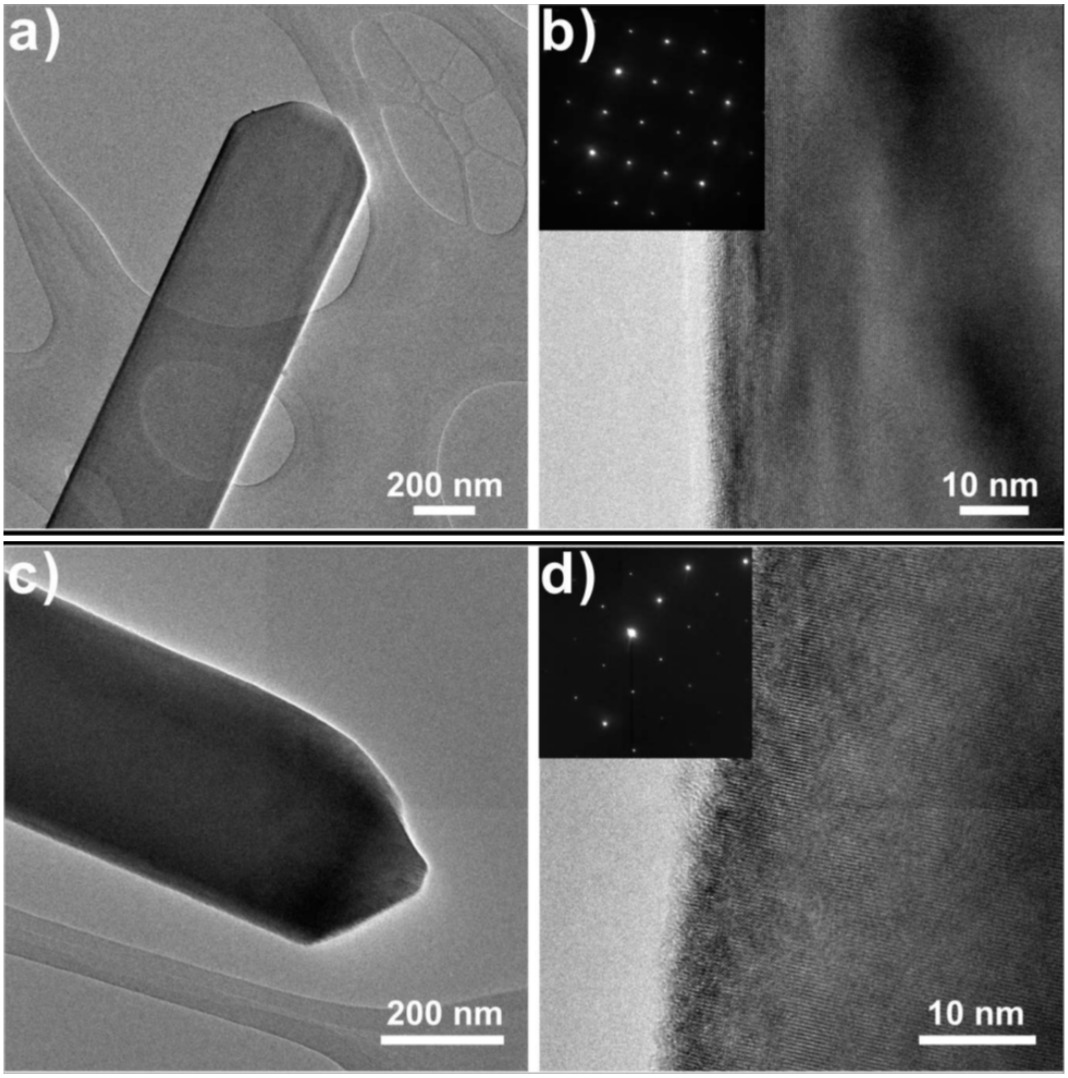

Figure 4.4 (a) Low-magnification TEM image of a pure VO_2 nanobeam. (b) High-magnification TEM image of a pure VO_2 nanobeam. Inset is the corresponding SAED pattern. (c) Low-magnification TEM image of the hydrogenated VO_2 nanobeam. (d) High-magnification TEM image of a hydrogenated VO_2 nanobeam. Inset is the corresponding SAED pattern. [20]

To measure the electrical conductance of the hydrogenated VO_2, four-terminal electron devices are fabricated on an on-substrate nanobeam (figure 4.5a). Before hydrogenation, a phase transition with conductance changing by 3 orders of magnitude is observed, and a fully metallic state is reached at ~395 K due to strain. After being hydrogenated above the MIT temperature for 15 min, the phase transition vanishes, and the devices show comparatively high conductivity down to 5 K (figure 4.5b, blue curve). Though the slope of resistance-temperature curve is not metallic, this can be expected due to the high strain as explained in Chapter 3.

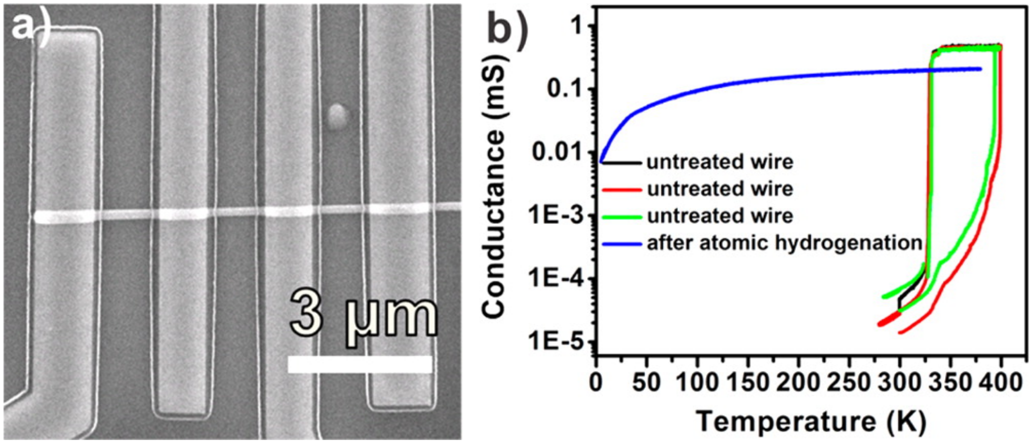

Figure 4.5 Electronic transport measurements of VO_2 nanobeam devices. (a) Optical image of a four-terminal VO_2 nanobeam device. (b) Conductance (log scale) versus T for pure VO_2 nanobeams (black, red, and green curves) and a typical one that was hydrogenated above the phase transition temperature for 15 min (blue curve). [20]

4.4. Preferred rutile structure

We now consider the effect of substrate temperature on hydrogen diffusion. Figure 4.6a shows pure VO_2 nanobeams lying on and strongly mechanically coupled to their growth substrate. Strain-induced metal−insulator domains when heating the materials above 340 K can be distinguished (Figure 4.6b). Domain structures persist up to 380 K, above which the material is fully in the metallic state (Figure

4.6c). If the same samples were hydrogenated above phase transition temperature (380 K) for 20 min, the phase transition disappears and the metallic state is stabilized when cooling down to room temperature (Figure 4.6d–e). On the other hand, the room temperature hydrogenation process is much slower, if not completely forbidden. The same VO_2 beams have been reused after baking in air at 250 °C for 30 min to recover the phase transition. Following hydrogenation at substrate temperatures below the phase transition temperature (e.g., 300 K) even for 3 h, the nanobeams still have no visible boundary or color change (at least under 100 nm resolution) caused by hydrogenation, and when heated up through the transition, they exhibit phase domain patterns similar to those seen in the unexposed pure beams. The Raman spectrum also confirms that the VO_2 nanobeams exposed to atomic hydrogen below the phase transition temperature have the same characteristics as pure beams, suggesting that the beams remain in the monoclinic phase after attempted hydrogenation below the phase transition temperature.

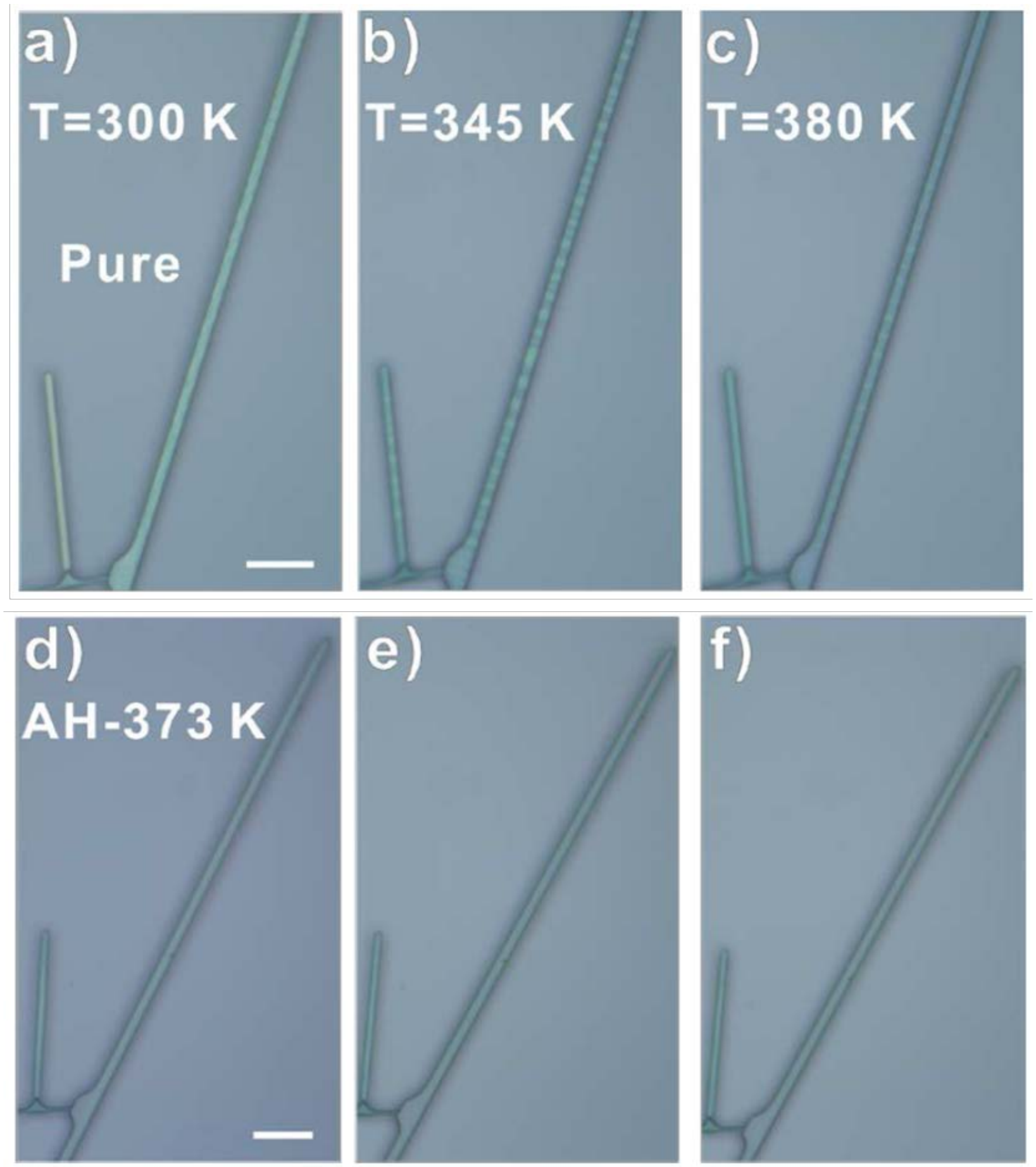

Figure 4.6 Optical images of VO_2 beams on Si substrate with 2 μm thermal oxide taken at 300 K, 345 K, 380 K respectively. (a-c) Pure VO_2 beams. (d-f) VO_2 beams with atomic hydrogenation at 100±10 ºC for 20 min. All of the scale bars are 10 μm. [20]

Because these experiments were performed without any catalyst, the temperature-dependent kinetics observed here should reflect that of the H−VO_2

system. It is true that impurity diffusion in solids is generally thermally activated. However, the significant differences observed for the motion of hydrogen-stabilized phase boundaries when the diffusion process takes place in the rutile vs the monoclinic state strongly suggests that the structural phase of VO_2 has an enormous impact on the rate of hydrogen diffusion. Empirically, hydrogen diffuses much faster along the c-axis of the rutile phase than along the (equivalent) a-axis of the monoclinic phase; attempts to diffuse H into beams in the monoclinic structure produce no observable hydrogen intercalation.

4.5. Diffusion constant

Based on these observations, to quantify the diffusion process we systemically studied the hydrogen diffusion rates of VO_2 nanobeams by exposing the nanobeams to atomic hydrogen while in the monoclinic and rutile phases for various durations. Experiments to estimate diffusion kinetics were restricted to transferred nanobeams that did not show large effects of interfacial strain. Figure 4.7a–c show the nanobeams exposed to atomic hydrogen while maintained in the rutile phase for 2.5, 5 and 10 min, respectively. As in Figure 4.2c, metallic domains indicated by darker color form at both ends and expand toward the beam centers as the exposure duration increases. Figure 4.7d shows the distance traversed by the boundary between the H-stabilized metallic domains and the monoclinic state, following various durations of exposure to atomic hydrogen while in the rutile state. Figure 4.7e shows that the average diffusion length is approximately linearly proportional to square root of time, as expected for diffusion, where a typical diffusion path distance scale is $L = (D\tau)^{1/2}$ after a time τ, and D is the diffusion constant.

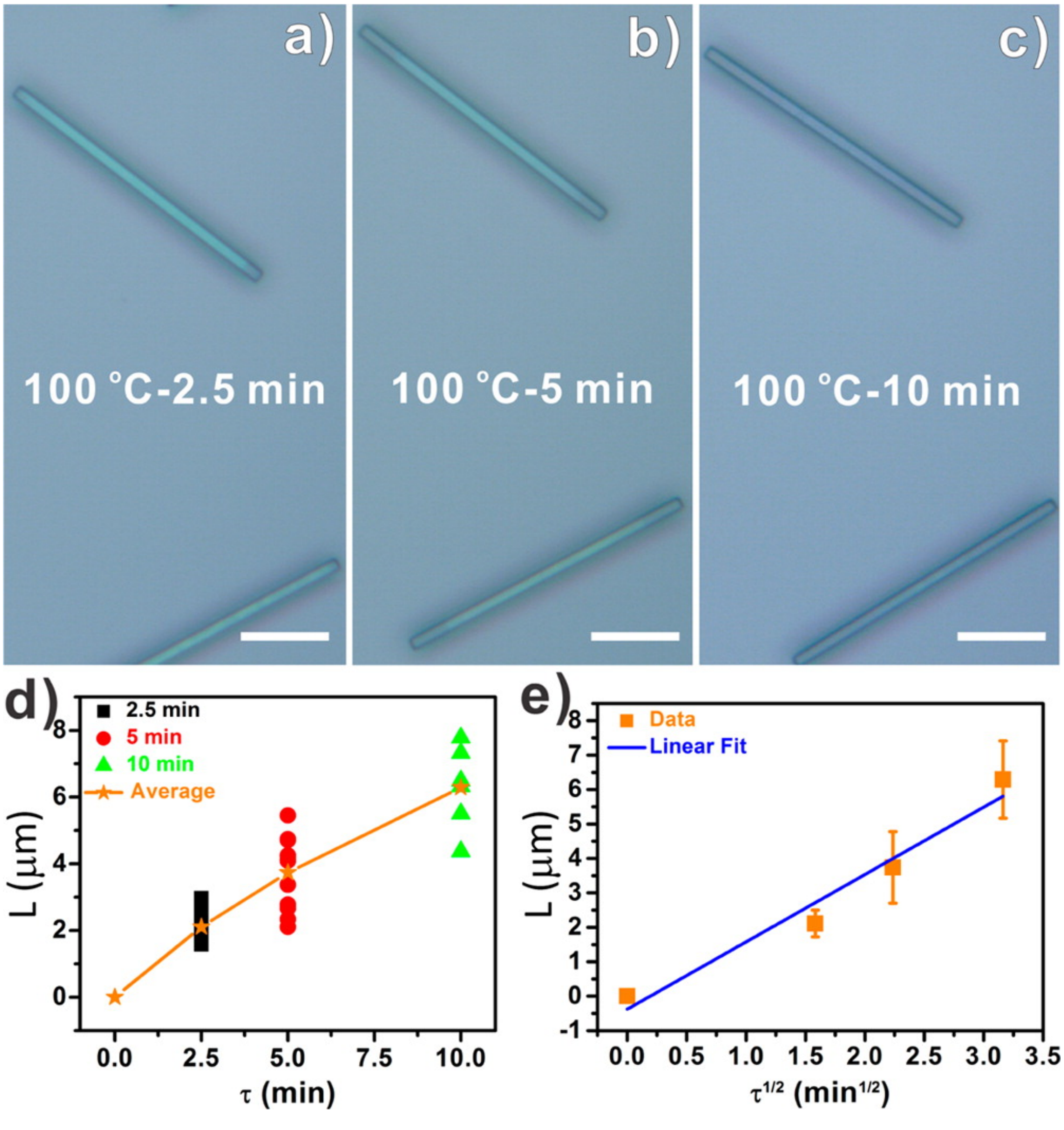

Figure 4.7 Hydrogen diffusion in VO_2 beams. (a–c) Representative optical images of a VO_2 beams following atomic hydrogenation at 100 ± 10 °C for 2.5, 5, and 10 min; scale bar, 10 μm. (d) Plot of diffusion length ($L_{Diffusion}$) (estimated from the size of the stabilized metallic regions) versus hydrogenation time (τ) of rutile phase VO_2 beams. (e) Plot of average $L_{Diffusion}$ versus $\tau^{1/2}$ of rutile phase VO_2 beams. [20]

Assuming an effective 1d diffusion problem and that the domain boundary is a proxy for reaching a critical level of hydrogen concentration within the material, the slope of the linear fit in Figure 4.7e allows us to determine the diffusion constant for H along the c-axis in rutile VO_2. With an uncertainty of a few percent from the fit, we find $D \approx 6.7 \times 10^{-10}$ cm^2/s. For comparison, extrapolating the expression of Johnson et al. [53] for the diffusion constant for H along the c-axis of isostructural rutile TiO_2 at 373 K, we find $D \approx 1.8 \times 10^{-11}$ cm^2/s. Thus diffusion of H along c in rutile VO_2 is around 38 times more facile than in rutile TiO_2. Note that Johnson et al. report for TiO_2 that the H diffusion constant transverse to the c-axis direction at 373 K is lower by a factor of $\sim 10^7$, so it is not surprising that we observe no evidence of H diffusion from the sidewall of VO_2 nanobeams.

On the other hand, the motion of the boundary of the H-stabilized metallic region is less than 100 nm in three hours when hydrogenation takes place in the monoclinic state, suggesting that the corresponding diffusion constant D_M must be orders of magnitude smaller than that when the beam is exposed in the rutile state (D_R). An alternate possibility is that the solubility of hydrogen in the monoclinic state is so poor that it is never possible for the monoclinic phase to accommodate enough hydrogen to trigger the transformation into the stabilized metallic structure. We also note that there is large beam-to-beam variability of the length of these domains (seen as the vertical spread in the data points in Figure 4.7d); we believe that this could be a manifestation of different strain conditions in the various beams modulating diffusion rates.

Overall, the trends are clear: (1) Atomic hydrogen diffuses rapidly along the c_R-axis, with no detectable diffusion transverse to the c_R-axis; (2) The diffusion constant for atomic hydrogen along the c_R-axis is at least 1000 times larger than that along the equivalent a_M-axis, even though the temperature difference between the rutile and monoclinic experiments was only tens of Kelvin.

4.6. *Ab initio* calculations

To further understand the physical mechanism of the difference in hydrogen diffusion rates between two phases, our colleagues Michael Swift and Professor Andriy H. Nevidomskyy performed *ab initio* structural calculations to estimate the energy scales associated with hydrogen diffusion. Again, I will skip the calculation details, and focus on the results.

The intercalation of atomic hydrogen into the atomic lattice of VO_2 is modeled as a diffusion process. In solids, the diffusion constant D is well modeled by the Arrhenius equation [54]

$$D = D_0 e^{-E_{diff}/k_B T} \qquad \text{Equation 4.1}$$

, where D_0 is the infinite-temperature diffusivity and E_{diff} is the energy barrier associated with diffusion of the impurity from site to site. Equivalently, the hopping frequency Γ is given by

$$\Gamma = \frac{D}{d^2} = \nu e^{-E_{diff}/k_B T} \qquad \text{Equation 4.2}$$

where d is the average jump distance and the $\nu = D_0/d^2$ is the attempt frequency [54].

Calculation of D would require detailed knowledge of the conditions outside the VO_2 lattice, an investigation of the vibrational modes of hydrogen ions within the lattice, and vibrational fluctuations in the vanadium and oxygen atomic positions. Such calculations are beyond the scope of this work, so instead, they consider the ratio of the diffusion rates between rutile and monoclinic phases

$$\frac{D_{rutile}}{D_{monoclinic}} = \frac{D_{0,rut}}{D_{0,mon}} e^{(E_{diff,mon} - E_{diff,rut})/k_B T} = \frac{D_{0,rut}}{D_{0,mon}} e^{\Delta E/k_B T} \quad \text{Equation 4.3}$$

To estimate the diffusion energy barrier *E_{diff}* for hydrogen ions in the two different phases of VO_2, they need to move the hydrogen in small steps to a periodically equivalent point further down the c_R-axis or a_M-axis, computing the total energy of the system at each point. The difference between the maximum and minimum energies is the energy barrier for this path. Two approximations are made here. First, the presence of hydrogen within the lattice is at relatively low concentrations, and thus only a small perturbation on the lattice structure in both the monoclinic and rutile phases. Second, hydrogen motion is sufficiently fast that no structural relaxation takes place. They note that the energy barrier along the true path is actually a saddle point in three dimensions: a maximum along the channel direction but a minimum in the plane transverse to the channel direction.

Swift and Nevidomskyy made an educated guess at the form of the path the hydrogen takes, which was then optimized. A straight-line path between two equilibrium hydrogen positions was perturbed with two orthogonal $\sin^2$ paths scaled by tunable parameters A and B, which were optimized to give the minimum energy barrier (Figure 4a). The $\sin_2$ form was chosen based on the observation in the structure calculations that hydrogen in VO_2 tends to form an H··O bond with the closest oxygen, so hydrogen will "swing" from oxygen to oxygen down the channel, with the swing amplitudes fixed by adjustable parameters A and B. The A direction is toward the oxygen bonded with hydrogen in the equilibrium (minimum energy) position, and the B direction is orthogonal to the lattice, toward the closer wall of the channel. The magnitude is normalized to the length of the H··O bond in the equilibrium position (1.02 Å). The path shown is the optimal one found for the rutile phase, with $A = -0.44$ and $B = 0.63$ (figure 4.8a). The path for the monoclinic phase had $A = -0.25$ and $B = 0.60$ (figure 4.8b).

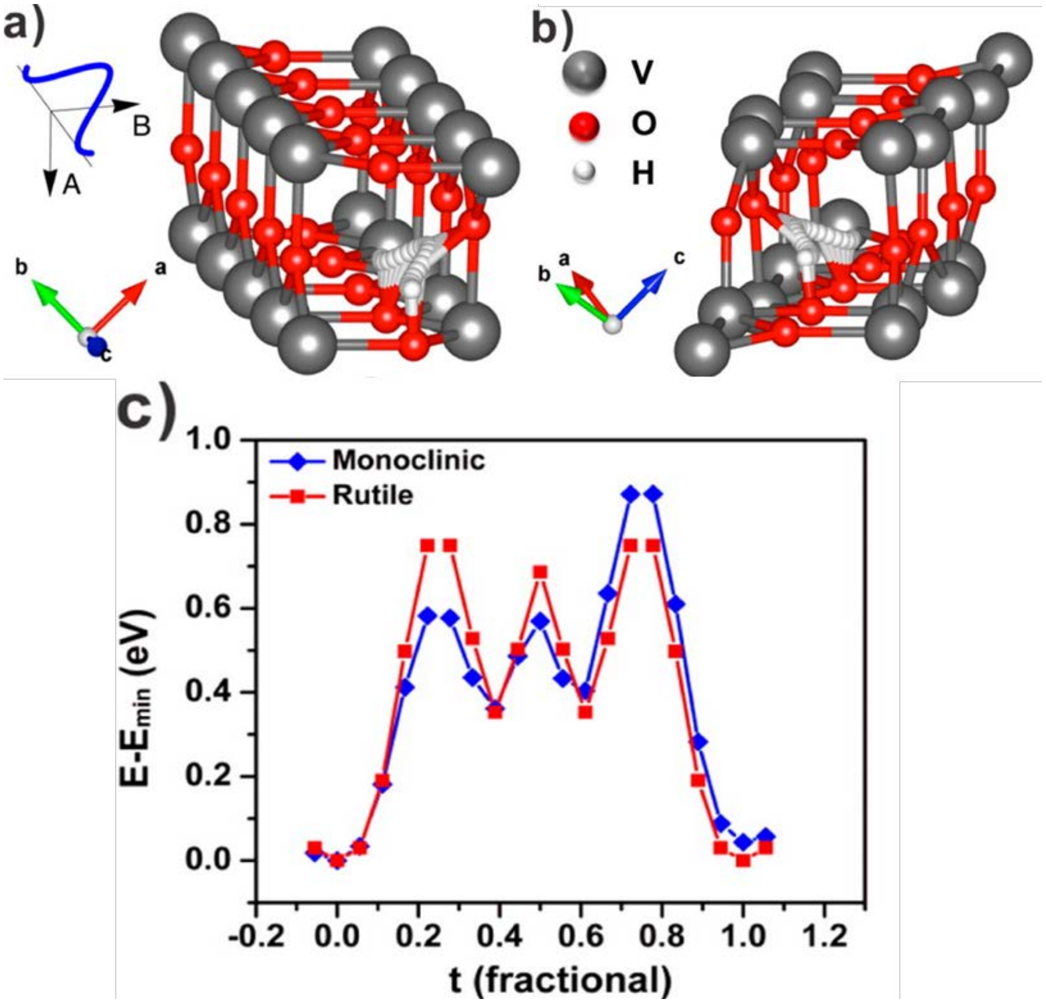

Figure 4.8 Ab initio calculations. (a) Lowest-energy path found for a hydrogen atom diffusing into rutile VO_2. The inset to subfigure a illustrates the $\sin^2$ perturbation from a straight-line path scaled by parameters A and B. (b) Lowest-energy path found for a hydrogen atom diffusing into monoclinic VO_2. Several positions of the hydrogen atom at different points along the path are superimposed, showing the path stroboscopically. (c) The energy of the hydrogen as it travels through the channel along the optimized path. t is a parameter that shows the fractional progress along the path. Note that lattice positions (e.g, the vanadium sites), which had been equivalent in the rutile phase, are no longer equivalent in the monoclinic phase because of the unit cell doubling. [20]

Figure 4.8c shows the energy of the system as the hydrogen is considered at various points through the channel along the optimized path. Here, t is a parameter which shows the fractional progress along the path. Note that lattice positions, which had been equivalent in the rutile phase, are no longer equivalent in the monoclinic phase. This is a result of the unit cell doubling in the monoclinic phase, and explains why the peak structure in Figure 4.8c is symmetric about the middle of the path as a function of t in the rutile phase, but asymmetric in the monoclinic phase. The numerical results for the diffusion barriers are

$E_{diff,mon} = 0.8717 \pm 0.0027$ eV

$E_{diff,rut} = 0.7494 \pm 0.0053$ eV

$\Delta E = 0.1223 \pm 0.0059$ eV

The activation energy for hydrogen diffusion in TiO_2 is ~0.6 eV [52], confirming that the results found here are reasonable. They will then compare the diffusion rates at the transition temperature, T = 340 K. At this temperature, following equation 4.3, they predict that the ratio of the diffusivities between the rutile and monoclinic phases should be $(D_{(rut)})/(D_{(mon)}) = (D_{0,rut})/(D_{0,mon})\ e^{\Delta E/k_B T}=65 \pm 13$, if the prefactors are assumed to be identical. These calculations show that on energetic grounds alone, one should expect hydrogen diffusion to be much faster along this favored direction in the rutile state than in the monoclinic structure. They stress that their calculation provides an upper bound on the diffusion barrier. The fact that the experimental ratio inferred from the motion of the boundary of the hydrogen-stabilized metallic region is much larger suggests that there is additional physics at work beyond what has been included in the calculation, presumably enhancing diffusion in the rutile structure. A large difference in the prefactors seems unlikely, given that the attempt frequency for hydrogen hopping is likely set largely by the H··O interaction, which should be similar in the two structural phases. A likely candidate would be vibrational dynamics known to lead to greatly enhanced diffusion rates in TiO_2 [54]. A recent ab initio molecular dynamics calculation indeed finds the diffusion barrier in rutile VO_2 to be ~0.4 eV [55], significantly lower than the one found here.

4.7. Conclusion

In summary, the atomic hydrogen generated directly from a hot filament was used to stabilize the metallic phase of the VO_2 nanobeams. The phenomenon that hydrogen diffuses preferentially along the c_R-axis was observed, consistent with past studies of hydrogen motion in rutile TiO_2. The diffusion constant for hydrogen along this direction in rutile VO_2 is even larger than that in TiO_2. Notably, the propagation of the front of hydrogen-stabilized metallic phase along the c_R-axis is at least 3 orders of magnitude faster than along the equivalent a-axis of monoclinic VO_2. Zero-temperature theoretical calculations are consistent with the idea that the activation barrier for hydrogen diffusion is considerably lower along this direction in the rutile structure than in the monoclinic phase. However, the enormity of the difference in apparent diffusion kinetics between the two phases suggests that the zero-temperature calculations underestimate the diffusion rate in the rutile structure. The contrast in hydrogen diffusion rates between the two structural phases suggests that VO_2 could be used as a switchable semipermeable membrane for hydrogen transport. Moreover, hydrogenation of VO_2 through direct exposure to atomic hydrogen demonstrates another effective way of modulating the electrical, chemical and optical properties of the VO_2, potentially paving the way for VO_2 devices with new functionalities.

Chapter 5

5. *In situ* diffraction study of H_xVO_2 powder

Part of this chapter was quoted from the published paper [56]:

In Situ Diffraction Study of Catalytic Hydrogenation of VO2: Stable Phases and Origins of Metallicity

Yaroslav Filinchuk, Nikolay A. Tumanov, Voraksmy Ban, Heng Ji, Jiang Wei, Michael W. Swift, Andriy H. Nevidomskyy, and Douglas Natelson

Journal of the American Chemical Society, 2014, 136 (22), pp 8100–8109. DOI: 10.1021/ja503360y

5.1. Introduction

To further study the concentration of hydrogen atoms intercalated in VO_2, and the corresponding modulation to the crystal structure, a systematic diffraction study is required. In this chapter, I present synchrotron and neutron diffraction studies of this material system, mapping out the structural phase diagram as a function of temperature and hydrogen content. In this work, hydrogenated VO_2 powders were prepared by our group, diffraction studies were performed by Professor Yaroslav Filinchuk's group in Université Catholique de Louvain, and the *ab initio* calculations were done by Michael W. Swift and Professor Andriy H. Nevidomskyy. I participated in the analysis and interpretation of the experimental results.

5.2. Sample preparation

5.2.1. VO_2 powder

Pure vanadium dioxide powders were prepared starting with commercially supplied VO_2 material (Alfa Aesar). As-supplied material was further purified by annealing under mildly reducing conditions (5 mbar of Ar) at 900 °C for 30 min to remove any V_2O_5 contamination. The resulting crystallites, tens of micrometers in diameter, were examined by optical microscopy and confirmed via their change in color and shape to undergo the MIT near the conventional transition temperature. These crystallites were mechanically ground using mortar and pestle to a finer powder with typical grain size ~10 μm. After mixing with a small amount of pure Si as an internal standard, a representative sample of this powder was examined at room temperature via conventional powder XRD (Rigaku DMAX Ultima II), and the resulting diffraction pattern was an excellent match with established lattice parameters for M1-phase VO_2, as determined by JADE 9.4 analysis software.

5.2.2. VO_2/Pd

Due to the limit of the experimental facilities, we could not perform the atomic hydrogenation process introduced in Chapter 4, so a catalyst was required for the hydrogen doping process. The VO_2 powder was thoroughly mixed with a solution of palladium (Pd) nanoparticles suspended in water (Sciventions Pd nanoparticle suspension 1.5 mg/mL), such that the mass fraction of Pd relative to VO_2 was 1%. The mixture was then heat-dried and vacuum-desiccated. From the studies in previous chapters, we had found that diffusion of atomic hydrogen proceeds most rapidly with help of Pd catalyst. The sample preparation was intended to increase the likelihood that most if not all VO_2 grains were in contact with multiple sources of catalytic spillover, while still maintaining a mass fraction for structural characterization dominated by the VO_2. Powder XRD measurements of the VO_2/Pd material indeed showed patterns identical to those produced with pure VO_2 powders, with any Pd signal falling below the detection threshold.

5.2.3. H_xVO_2/Pd, low pressure doping (O1)

Some of the VO_2/Pd material was then exposed to molecular hydrogen by annealing under flowing forming gas (20% H_2 and 80% N_2, total 1 bar) at 190 °C for 10 h in a tube furnace before being cooled to room temperature. Additional material was prepared by sealing this material under ~6 bar of forming gas in stainless steel tubing and baking at 190 °C for 1 week in an oven. For the rest of this chapter, we refer to this material as H_xVO_2/Pd. The resulting material exhibited powder XRD data consistent with an orthorhombic Pnnm phase (defined as O1 phase) previously assigned as isostructural to β-HCrO2 (Figure 5.2a).

5.2.4. H_xVO_2/Pd, high pressure doping (O2)

To investigate the high hydrogen content limit, we performed high-pressure autoclave hydrogenation. About 100 mg of VO_2/Pd sample was placed inside stainless steel autoclave tightly connected to a gas dosing system. In order to avoid a possible reaction between the sample and steel, the former was placed inside a glass tube, open on one end. The autoclave was placed inside an oven and the system was evacuated to $\sim 10^{-2}$ mbar for 2 h. Then 15 bar of hydrogen was loaded and the autoclave was heated to 468 K within 1 h, and kept at this temperature for 2 days. After this period, the power was cooled down to room temperature under 15 bar of hydrogen pressure. The autoclave was opened a day later, and the sample was quickly (within 1 h) characterized by powder XRD. The data revealed a different orthorhombic phase (O2 phase) from the one of the previous sample treated in 1 bar hydrogen gas. We note that these samples, sealed in a glass bottle under air, are stable at room temperature.

5.2.5. D_xVO_2/Pd, high pressure doping (O2)

Finally, to prepare samples for neutron powder diffraction, Dr. Filinchuk performed manometric high-pressure autoclave deuteration. A large (1.83 g) D_xVO_2/Pd sample was prepared by exposing VO_2/Pd sample at 468 K to 5 bar of deuterium pressure for 30 h and then to 17 bar D_2 for another 4 days. Pressure measurements were done continuously using 300 bar Keller pressure gauge with 30 mbar precision. The deuterium uptake took nearly 3 full days, and then the pressure stabilized. The autoclave was slowly cooled to the room temperature. Powder XRD showed that the sample was very similar to the one obtained by high-pressure hydrogenation (O2 phase).

5.3. *In situ* synchrotron powder X-ray diffraction (XRD) experiments

Two rounds of experiments were completed by Dr. Filinchuk in two facilities respectively. The data of the first one has relatively low quality, so all the results shown below, as well as the discussion, are based on the second round of experiment done at Swiss-Norwegian Beam Lines (SNBL) of the European Synchrotron Radiation Facility (ESRF, Grenoble, France) using a pixel area detector PILATUS 2M. Dr. Filinchuk found that hydrogenation of the hydrogen-free VO_2/Pd sample was slow even at higher pressures. Heating such a sample in a 1 bar hydrogen environment and holding for 20 min at 486 K was not sufficient to complete the hydrogenation, leading to an inhomogeneous material. Therefore, the analysis in this chapter is largely focused on the structural evolution under different temperatures and hydrogen pressures of the pre-hydrogenated (treated for more than 10 hours) H_xVO_2/Pd material, rather than monitoring the hydrogenation process of a pristine VO_2/Pd sample. Diffraction patterns were acquired as the sample temperature was ramped in different protocols. Here we select some representative protocols and analyze their patterns after refinement.

5.3.1. Measurement in air

Figure 5.1 shows the diffraction patterns between 27° and 35° in 2θ for an H_xVO_2/Pd (O1) sample measured under 1 bar of air in a closed capillary as the temperature is ramped. The ambient temperature is increased from 316 to 468 K, held at 468 K for 20 min, and decreased to 80 K. In Figure 5.1, the beginning of the experiment corresponds to the pattern on the top. It shows the monoclinic $P2_1/c$ H_xVO_2 phase (M1) in a mixture with an orthorhombic *Pnnm* H_xVO_2 phase (O1). This O1 structure is a derivative of the tetragonal cell formed by an orthorhombic distortion, and corresponds to the *Pnnm* phase originally put forward by Chippindale et al. [39]. The refined mass fractions of the two phases are close to 1:1 in the initial trace. The slightly larger formula volume of the orthorhombic cell suggests this phase is hydrogenated.

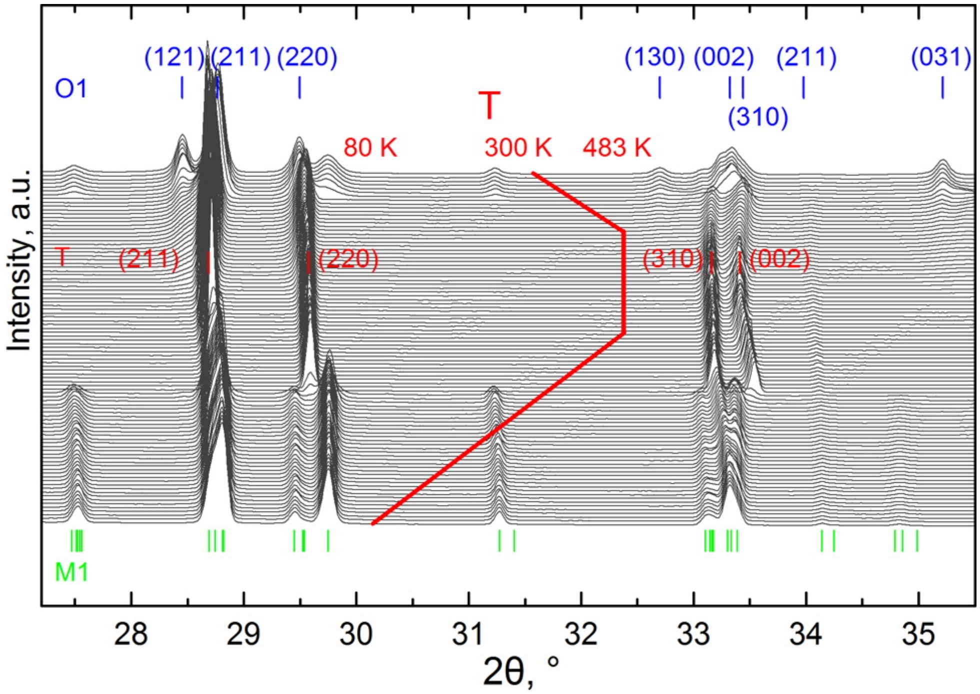

Figure 5.1 Waterfall plot of a fragment of diffraction pattern for H_xVO_2/Pd sample in 1 bar air, over the temperature cycle shown in red. Initially (topmost trace) the sample is a mixture of the orthorhombic O1 phase and the monoclinic M1 phase. As the sample passes through ~332 K on warming, the M1 phase transitions to the T phase. The pattern evolves with time during the high-temperature part of the cycle, as hydrogen leaves the sample. Upon cooling through ~327 K, the entire sample volume converts to the M1 phase as the temperature is further reduced. λ = 0.82257 Å. [56]

Upon heating, The M1 component transforms to the tetragonal H_xVO_2 (T) at ~332 K; the reverse transition from the tetragonal VO_2 to the monoclinic VO_2 occurs at 327 K on cooling. The last pattern is made only of the monoclinic phase, containing apparently a very small (or no) amount of hydrogen (as determined by comparison with diffraction from the non-hydrogenated, pure VO_2 material). No signal from crystalline palladium or its hydrides was observed in any of the diffraction patterns. At the highest temperature of 468 K, a pure tetragonal $P4_2/mnm$ H_xVO_2 phase is obtained.

Figure 5.2 shows the structures of these three phases, omitting the hydrogen positions. The structures are visualized looking just slightly misaligned from the monoclinic a-axis direction (the tetragonal and orthorhombic c_R-axis). The dimerization of the V atoms that leads to the unit cell doubling of the M1 phase is readily apparent. And in all of the X-ray data collected, there is no evidence of detectable oxygen deficiency (put forward as a concern mentioned in section 2.8).

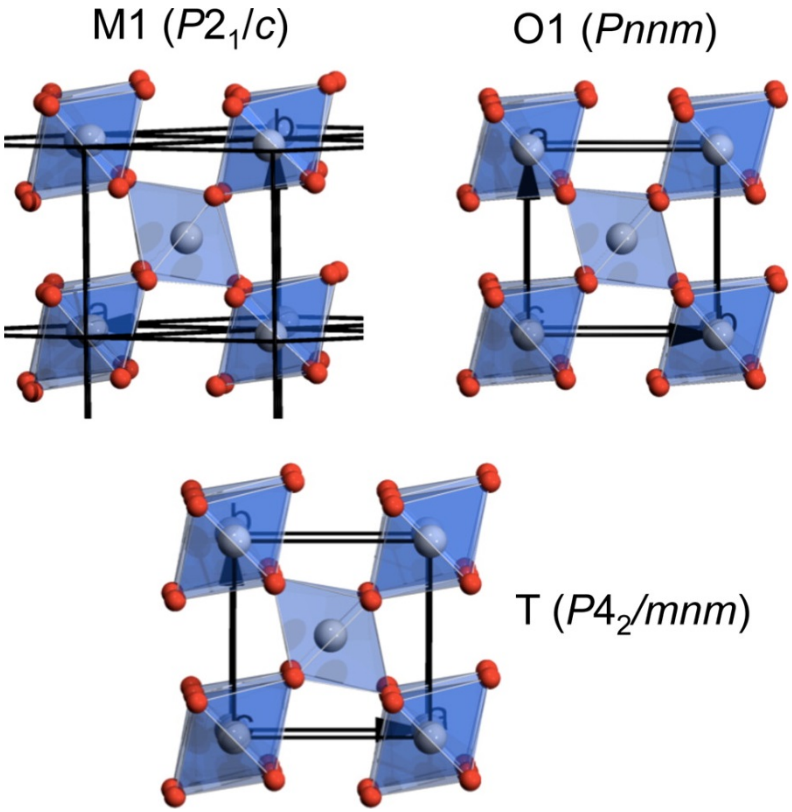

Figure 5.2 Structures of the three phases observed in the experiment of Figure 5.1. Oxygen atoms are in red, vanadium atoms are colored gray. Structures are visualized from a vantage point slightly misaligned with the conventional a direction

for monoclinic. The orthorhombicity (inequity of the a and b lattice parameters) of the O1 phase is difficult to resolve by eye at this scale. [56]

Having determined the base structures of the relevant phases, it was possible to analyze all of the data in that context, yielding variation of cell parameters and phase fractions as a function of temperature and hydrogen pressure. Figure 5.3a traces the evolution of the H_xVO_2 formula unit volume with temperature for Figure 5.1. The unit volume generally increases with increasing temperature due to thermal expansion, and also increases with hydrogen concentration due to the intercalation of hydrogen atoms. This explains the positive slope for all curves in figure 5.3a. And the decrease of volume of the T phase with time while temperature is fixed at 468 K suggests the loss of hydrogen from the T phase. Figure 5.3b shows the gradual conversion of O1 phase into T phase at high temperatures, also implying the loss of hydrogen from the O1 phase. Below 327 K, the hydrogen-depleted tetragonal phase transforms back to the monoclinic phase. There is some evidence of limited hydrogen re-absorption in the residual T phase before the last of the T phase transforms into M1, since the sample was in a sealed capillary.

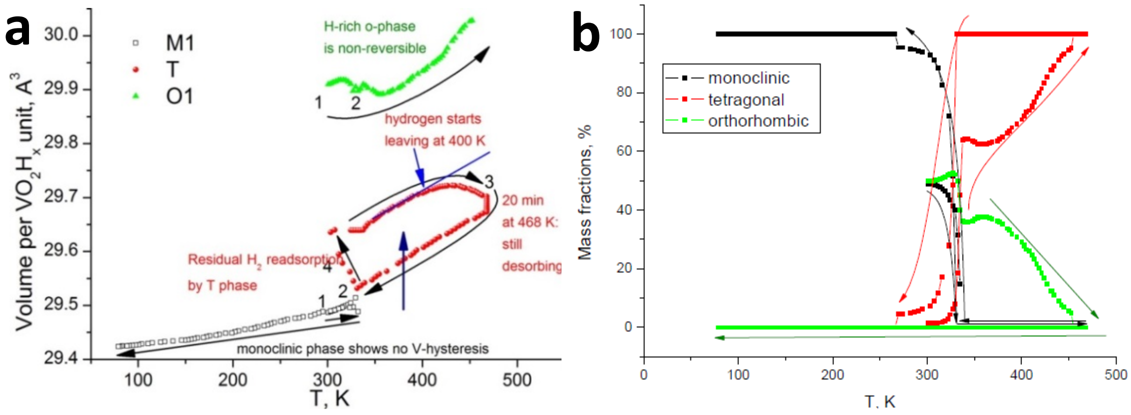

Figure 5.3 (a) Evolution of formula unit volume throughout the heating cycle shown in Figure 5.1. Initial composition (1) is a 50/50 mixture of M1 (gray) and O1 (green) phases at 300 K. Upon warming (2), the M1 phase transforms into the T phase (red) at 332 K. At higher temperatures, the O1 phase gradually transforms into the T phase (3). Upon cooling, the T-phase material transforms back into the M1 phase. The conversion of O1 into T and the decrease in T formula unit volume at the high temperatures are consistent with the loss of hydrogen from the material. (b) Phase fractions for the M1, T and O1 phases in the *in situ* experiment. [56]

5.3.2. Measurement in H_2

As a control experiment, a similar H_xVO_2/Pd (O1) sample was measured under 25 bar of H_2 at temperatures from 319 to 468 K, held at 468 K for 20 min, and cooled to the room temperature. Figure 5.4 traces the formula volume of the tetragonal phase for this sample (black squares) and for the sample measured in air (red squares). In the hydrogen-rich environment, the volume of the T phase increases irreversibly upon cycling to the high temperature, consistent with enhanced hydrogen uptake. It is clear that the tetragonal phase has a large concentration range of hydrogen solubility. At the higher hydrogen pressures the tetragonal phase absorbs more hydrogen during the heating/cooling cycle to 468/291 K, expanding its formula unit volume by 1.3% (relative to the monoclinic phase at room temperature). Upon cooling, this hydrogen-enriched tetragonal phase remains stable regarding its transformation into the monoclinic phase, down to at least 291 K. This is consistent with the observations of H_xVO_2 prepared by thermal decomposition of paramontroseite [40], where Wu et al. found a room-temperature-stable T phase for x > 0.003.

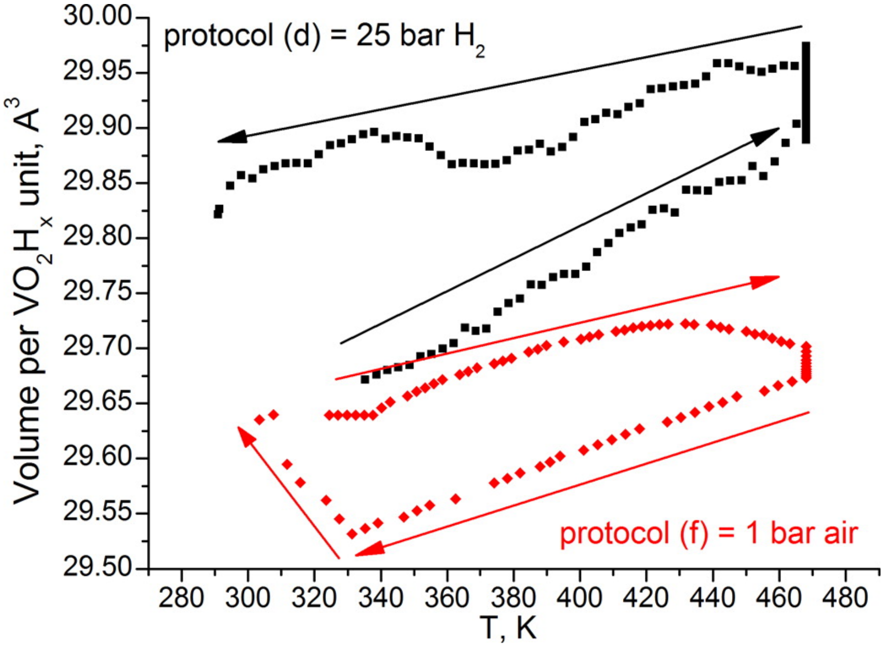

Figure 5.4 Evolution of T phase formula unit volume with temperature for different gas environment. Red squares (lower trace) correspond to measurement in air and the data from Figures 5.1 and 5.3. In a closed capillary with 1 bar air, the T phase expands due to thermal expansion. However, the same T phase contracts as a function of time due to hydrogen loss, while held at constant temperature of 468 K. Upon cooling, volume contracts as expected, with an upturn as T phase is converted to M1 phase, likely due to hydrogen re-uptake. In contrast, black squares (upper trace) correspond to measurement in 25 bar H_2 gas. The T phase increases its

volume upon warming due to a combination of thermal expansion and hydrogen uptake. [56]

In addition to the volume expansion of the T phase, the sample measured at 25 bar of hydrogen gas reveals that hydrogenation induces a conversion of the tetragonal phase into a more hydrogen-rich orthorhombic *Pnnm* phase, O1. This is the same O1 phase that was already present in the as-prepared H_xVO_2 material (as in the initial trace in Figure 5.1). During the 20 min at 468 K, roughly 40 wt% of the T-phase H_xVO_2 is transformed from the $P4_2/mnm$ to the O1 *Pnnm* phase. Longer exposure to hydrogen at this temperature allows obtaining pure *Pnnm* phase.

5.3.3. O2 phase

Even higher hydrogen content leads to another orthorhombic phase, O2 phase. Sample preparation described in the section 5.2.4 results in the formation of a more hydrogen-rich H_xVO2/Pd phase, characterized by the increased unit cell volume. Laboratory XRD on the autoclave-hydrogenated sample shows a powder pattern similar to the one of the *Pnnm* phase, but with significantly different refined cell parameters: a = 4.4795(12), b = 4.7372(11), and c = 2.8944(5) Å. The b parameter is notably increased, as compared to a = 4.5061(1), b = 4.6300(1), and c = 2.86721(8) Å for the O1 *Pnnm* phase, thus augmenting the orthorhombic deformation. This sample has been studied in detail by diffraction on single crystals. Indexing of the reciprocal lattice unequivocally shows doubling of the orthorhombic

Pnnm cell in all three directions. The resulting cell is F-centered. The systematic extinctions give only one option for the space group: the non-centrosymmetric *Fdd*2.

Examination of the powder diffraction data revealed that the *Fdd*2 phase (O2) is a distinct new phase forming at higher hydrogen concentrations, and it is not identical (though closely related) to the *Pnnm* phase observed previously at lower hydrogen concentrations. The final results (a and b directions are swapped in order to get a conventional cell) from this analysis indicate cell parameters a = 9.4285(19) b = 8.9309(13), c = 5.7652(6) Å. In this cell there are two inequivalent V⋯V distances, V1–V2, of 2.783(2) and 2.982(2) Å. They are significantly different from the average 2.867 Å in the O1 structure at room temperature. The shorter of the two is longer than 2.6139(8) Å in the monoclinic phase at room temperature, which suggests that Peierls dimerization is less pronounced in the hydrogenated samples. Remarkably, the shorter V⋯V distance forms within V_2O_2 diamonds formed by H-free oxygen atoms, while the longer V⋯V distances appear in $V_2(OH)_2$. Thus, the separation of V⋯V distances fully supports localization of the H atom only on one of the two oxygen sites. In other words, it would appear that the hydrogen positions in the O2 phase are spatially ordered. The graphical presentation of the hydrogen ordering on the transition from O1 to O2 phase is shown in Figure 5.5.

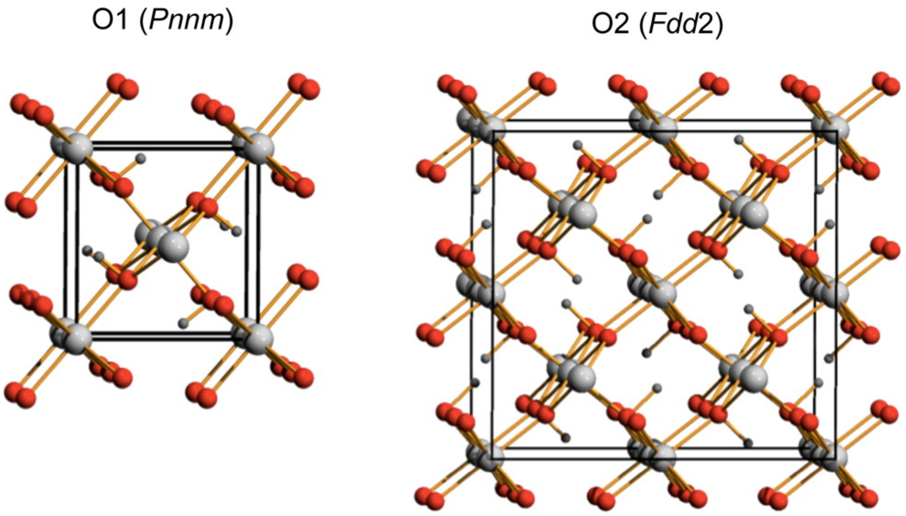

Figure 5.5 Structures for the O1 and O2 phases, as inferred from synchrotron diffraction measurements, looking nearly down the respective c-axes. Oxygen atoms are red spheres, vanadium atoms are large gray spheres, and hydrogen atoms are small gray spheres. In the O1 phase, the hydrogen atom positions are generally not ordered, and are only shown here in an ordered pattern for illustrative purposes. In the O2 phase, the hydrogen atoms are spatially ordered as shown. [56]

5.4. Neutron powder diffraction and phase diagram

To reliably determine the hydrogen atom position and hydrogen content, Dr. Filinchuk performed neutron powder diffraction on the corresponding deuteride D_xVO_2 (deuterium is used instead of hydrogen to avoid the large inelastic neutron scattering of the latter). The *Fdd*2 structure and hydrogen ordering in the O2 phase were fully confirmed, giving the refined composition $D_{0.460(8)}VO_2$. The refined atomic positions show O1–D1 distance of 1.021(8) Å, typical for a hydroxyl group. The O–D group is capping three V atoms by oxygen, with O–D vector perpendicular to the V triangle. The nearest D–D distance exceeds 3 Å. Notably, refinement of the anisotropic atomic displacement parameters for the deuterium atom leads to the reasonable 50% probability ellipsoid (see Figure 6). This anisotropy suggests a hydrogen hopping path from O1 to O2 atom, shown by the blue dashed bond (D1⋯O2 = 2.553 Å). An analogous site-to-site path [52] is thought to apply to diffusion of hydrogen within tetragonal TiO_2.

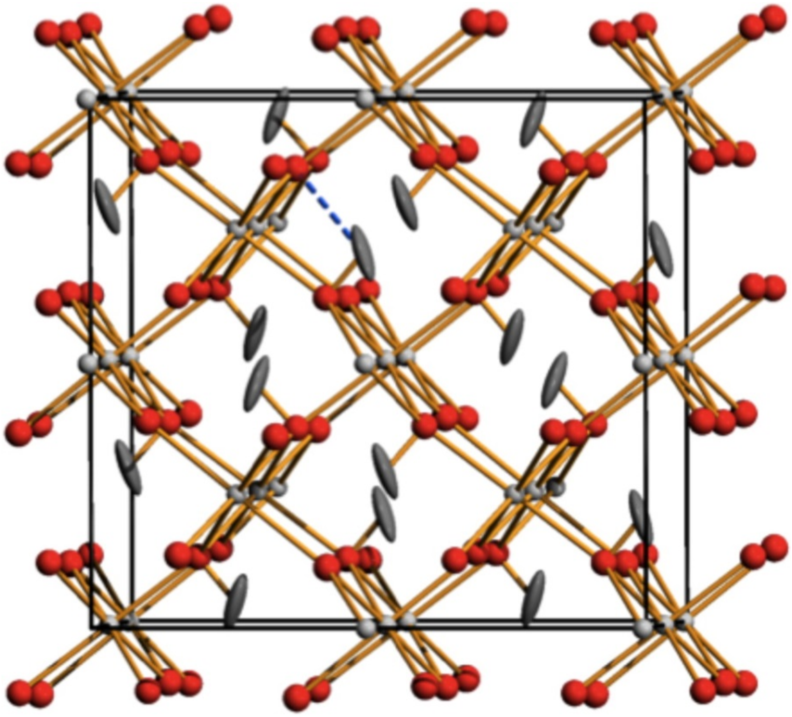

Figure 5.6 Structure of the O2 phase as determined by neutron powder diffraction. Gray 50% probability ellipsoids show the locations of the (ordered) deuterium atoms. Again the structure is drawn looking nearly down the c-axis. The anisotropy in the probabilistic D positions suggests the dashed blue path as a likely trajectory for site-to-site diffusion of hydrogen within the lattice. [56]

In the end, Dr. Filinchuk combined the results and data from Chippindale et al. [39], and constructed a phase diagram (Figure 5.7) for the VO_2–hydrogen system.

The tetragonal phase is stable at elevated temperatures only. Its stability range increases with hydrogen concentration. However, at lower temperatures, a two-phase mixture of the H-poor monoclinic and relatively H-rich O1 phase is observed.

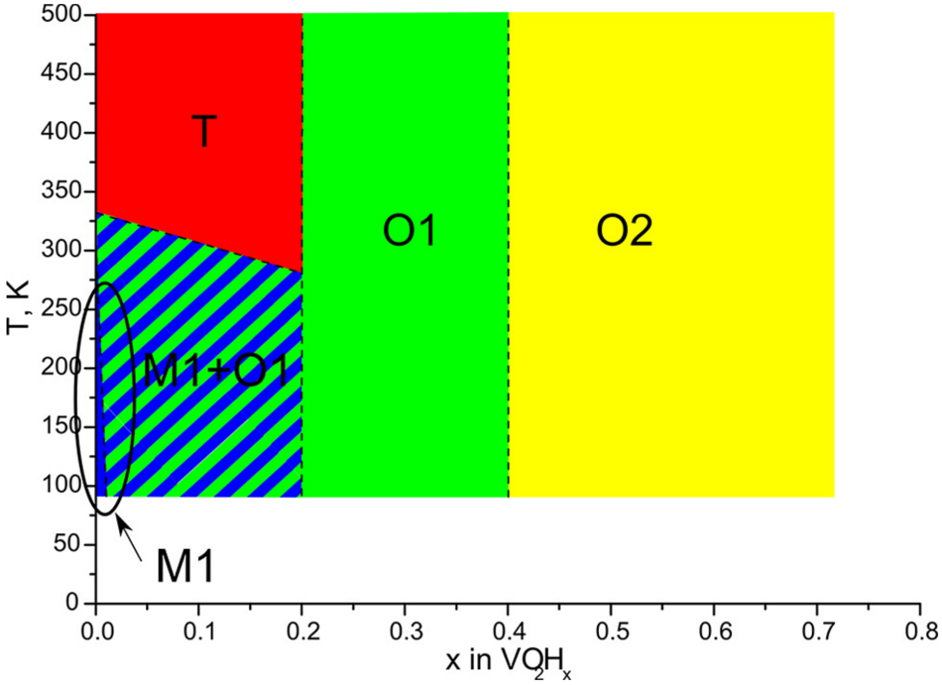

Figure 5.7 Phase diagram of the hydrogen–VO_2 system, deduced from the data presented in this work. The boundaries of the O1 phase are conjectural. [56]

5.5. *Ab initio* calculations

To gain further insights into both the O1 and O2 phases, *ab initio* calculations based on the two determined structures have been performed by our collaborator Michael Swift and Dr. Andriy Nevidomskyy. Again, I will omit the calculation details, but focus on the results and discussion.

It is worth noting that traditional DFT methods have a notoriously difficult time reproducing both the relative energies of candidate structural ground states (M1 vs T) and the lack of magnetic ordering in VO_2 [18]. However, given the experimentally determined structures, DFT methods have been very successful in giving insights into the underlying physics.

The theoretical results comparing the energies of the O1 and O2 structures are shown in Figure 9c. The binding energy of the O1 structure is lower for small hydrogen concentrations $x \leq 0.25$, however at higher concentrations, the O2 structure is energetically favored, which agrees well with the experimental findings presented earlier.

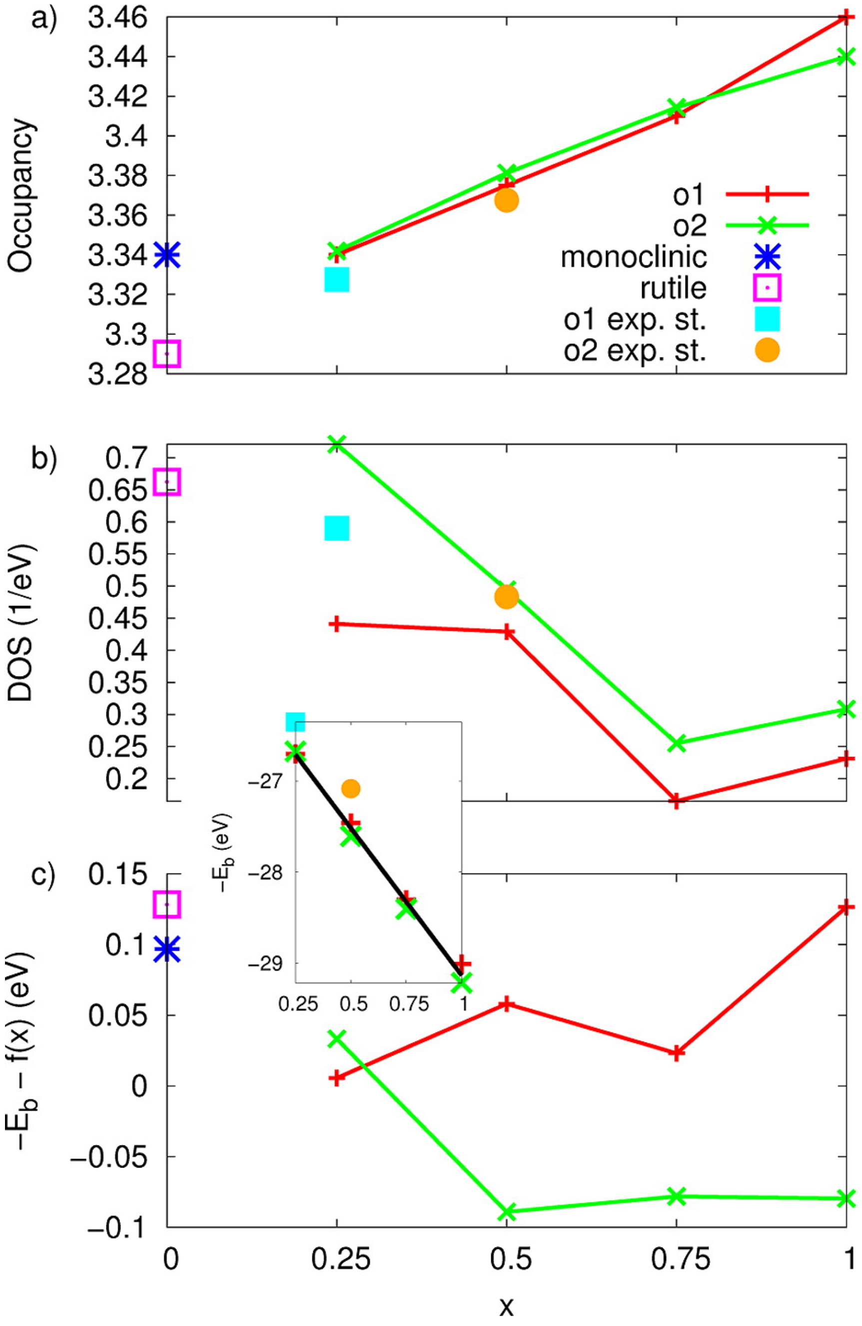

Figure 5.8 Results of ab initio calculations comparing the various structural phases at different hydrogen concentrations. (a) Average occupancy of the vanadium 3d orbitals as calculated by Mulliken population analysis, plotted as a function of hydrogen concentration x. Values calculated from the experimental structure without geometry optimization are also included. (b) Density of states at the Fermi level, calculated with a smearing width of 0.1 eV. Inset: minus binding energy, $-E_b$,

per VO_2 formula unit, in eV, plotted as a function of hydrogen concentration x. Linear fit, $f(x) = -3.235x - 25.898$, superimposed in black. (c) Binding energy with the linear trend removed to show the differences between phases. Note that the O1 phase is favored at x = 0.25, and the O2 phase is favored at higher values of x. [56]

In order to address the issue of metallicity, it is instructive to examine the occupation of vanadium d-levels. As Figure 5.8a shows, the average d-level occupancy grows with hydrogen content, as discussed in prior work. This can be easily understood as follows: the binding of the hydrogen to the oxygen shifts the electron density on oxygen away from the V–O–V bonds, as illustrated schematically in Figure 5.9. Effectively, this is equivalent to the oxygen on site “B” being less electronegative, and as a result, the V–O bond becoming less ionic, with more electron density residing on the B-site vanadium compared to that in the rutile structure (site “A”). The detailed calculation of the electron occupancy using the Mulliken analysis gives the difference in charge (δ) between A-site and B-site vanadium to be 0.06.

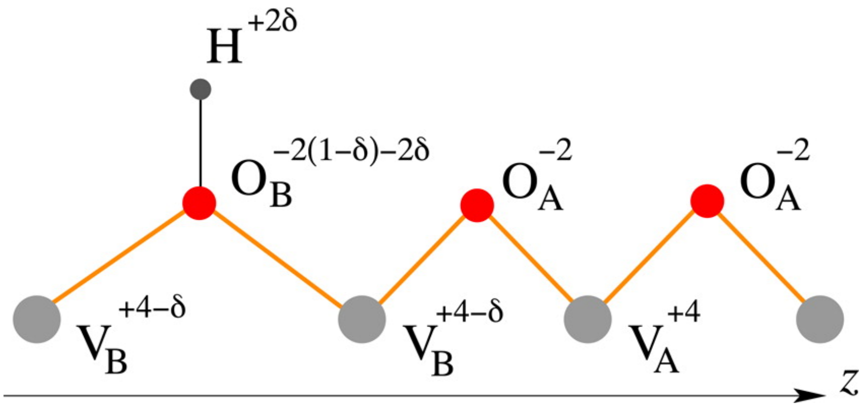

Figure 5.9 Schematic of charge redistribution due to hydrogen binding to B-site oxygens. This also results in the weaker $V_B \cdots O_B$ bonds and consequently, in dimerization, with the $V_B \cdots V_B$ distances being longer than the $V_A \cdots V_A$ distances. [56]

The less ionic $V_B \cdots O_B$ bond results in a longer $V_B \cdots O_B$ distance, compared to the $V_A \cdots O_A$ bond away from the hydrogen site. This in turn leads to the $V_B \cdots V_B$ distances being longer than the $V_A \cdots V_A$ distances (see Figure 5.9), explaining our experimental finding that the V⋯V distances are longer within the $V_2(OH)_2$ block of the O2 structure. We see that the periodic ordering of the H sites in the O2 structure thus leads to dimerization of the V⋯V distances, resulting in the doubling of the unit cell along the rutile c-axis. However, as mentioned earlier, the differentiation of V⋯V distances is less pronounced in the O2 phase than in the monoclinic phase of pristine VO2, likely because of the overall expansion of the unit cell due to hydrogen absorption. We note that while theoretically, the O1 phase is also dimerized, in an experiment the disorder on hydrogen site results in only one inequivalent O position and the V⋯V dimerization is thus quenched.

The increase in the d-level occupancy on B-site vanadium is reflected in the partial density of states (PDOS), so that the spectral weight shifts below the Fermi level, developing a pronounced peak (see Figure 5.10a). By contrast, the A-site vanadium has PDOS reminiscent of the rutile structure, with a shoulder rather than a peak below the Fermi level. It is this increase in vanadium d-level occupancy that is responsible for the suppression of the MIT in hydrogenated VO_2. Theory unambiguously predicts that both the O1 and O2 structures are metallic. Note however that despite the shift of the spectral weight below the Fermi level on B-site vanadium, the total DOS at the Fermi level actually decreases with increasing H doping (see Figure 5.8b). This is explained in part by the lattice expansion upon hydrogenation, which ought to decrease the DOS, and is consistent with the transport measurement in previous chapter (like figure 4.5b) which shows that the conductance of hydrogenated VO_2 is slightly lower than that of a pristine metallic one.

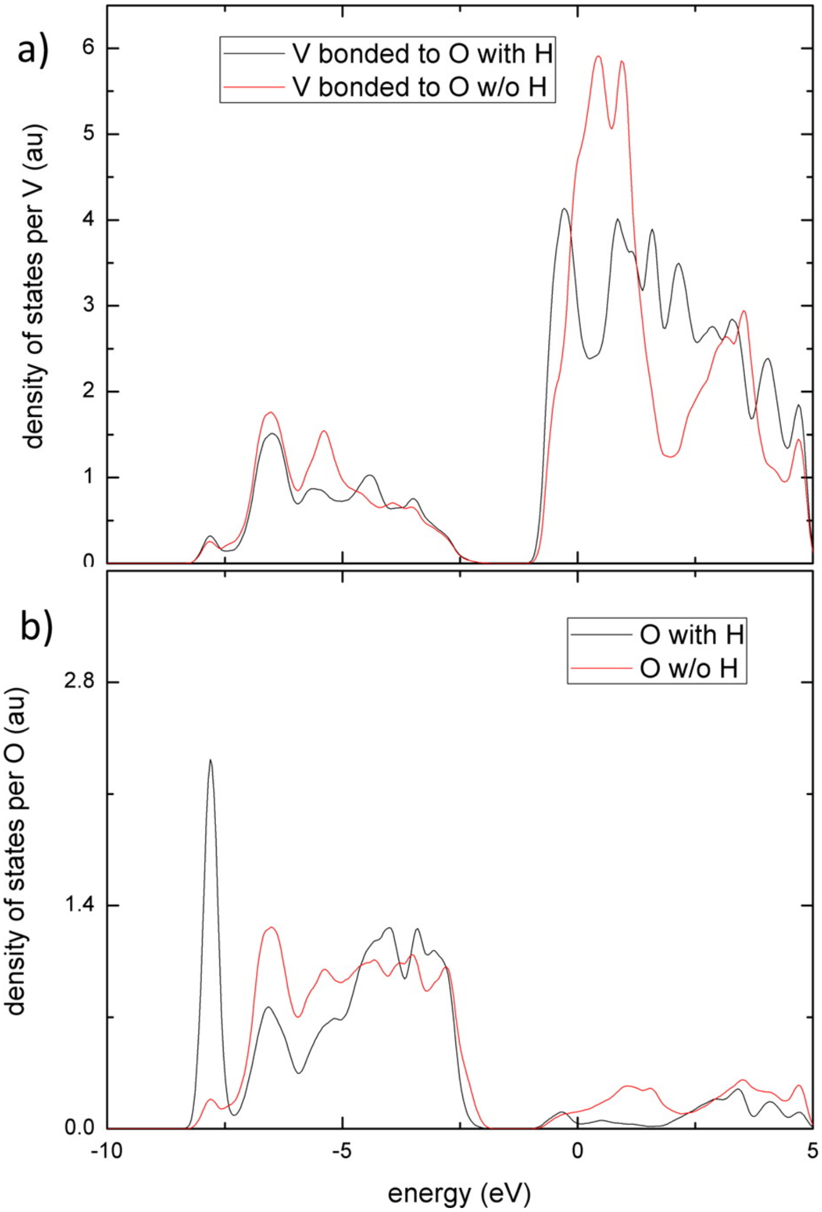

Figure 5.10 Calculated partial densities of states for (a) vanadium (3d band) and (b) oxygen (2p band) atoms. Results for A-site atoms (no hydrogen proximal to the relevant oxygen) are in red; results for B-site atoms (hydrogen proximal to the relevant oxygen) are in black. Note that hydrogen binding to oxygen results in a transfer of spectral weight below the Fermi level for the B-site vanadium 3d band. [56]

5.6. Conclusions

In this chapter we present the stable structures adopted by vanadium dioxide as it accommodates atomic hydrogen as an intercalant. These phases were found through extensive variable temperature synchrotron powder diffraction experiments by our collaborators that examine the evolution of the VO_2 crystal structure *in situ* as it accommodates intercalated atomic hydrogen. We also report our collaborators' neutron powder diffraction of D_xVO_2/Pd material. None of these experiments show evidence of oxygen removal from the lattice. In addition to the previously identified structural phases, Dr. Filinchuk identifies a new orthorhombic (O2) phase of *Fdd*2 symmetry (with a 2a,2b,2c supercell with respect to the *Pnnm* structure). Using orthorhombicity as a proxy for hydrogen concentration, calibrated via the neutron measurements of $D_{0.460(8)}VO_2$, he constructs the phase diagram for the H_xVO_2 system.

In addition to discovering the O2 phase, these experiments and their theoretical analysis give insight into the physics of the long-discussed MIT in VO_2. First-principles calculations confirm that one key effect of hydrogen doping is to increase the d occupancy of the vanadium ions bound to oxygen atoms that are coupled to hydrogen atoms. This transfers spectral weight below the Fermi level in the electronic density of states, and thus favors metallicity. It is worth noting that the O2 phase, with its doubled unit cell, has a certain amount of dimerization of the one-dimensional vanadium chains that run along the c_R-axis. However, despite this dimerization, the O2 phase remains metallic, showing that Peierls physics and the resulting dimerization are not the dominant factors in determining the electronic structure of this phase. First principles calculations further confirm that at high x the O2 phase is expected to be energetically favored over the O1 phase.

Chapter 6

6. Low temperature transport measurement of VO_2

6.1. Introduction:

In previous chapters, we have systematically studied and discussed the hydrogenation process of VO_2, the crystal structure of hydrogenated VO_2, and the possible role played by intercalated hydrogen atoms in VO_2. Although the temperature dependence of resistance of VO_2 before and after the hydrogenation process has been shown in these studies, a detailed low temperature transport characterization has not been performed yet. Since we have known that hydrogen dopants at high enough concentrations can stabilize VO_2 in a conducting state, with no phase transition, it will be interesting to see how this new system will behave in a low temperature condition, especially with regard to its electronic properties. Previously, such measurement could not be carried out due to the phase transition of VO_2, which results in an insulating phase with exponentially suppressed conductance at low temperature. However, the discovery of the fully hydrogenated conducting VO_2 sample provides, for the first time, a chance for people to study the low temperature transport properties of VO_2 in a structure (orthorhombic) close to that of the pristine rutile phase (tetragonal).

In this chapter, I will present the transport properties of this hydrogenated VO_2 as an analogue of the pristine metallic VO_2, and discuss the extremely small Hall signal and positive/negative magneto-resistance responses observed in different samples. Repeated measurements on tens of different samples have been done to ensure the reproducibility of the results.

6.2. Sample preparation

Three kinds of single-crystal VO_2 samples were used for hydrogen doping and the transport measurement. The first was VO_2 thin film grown by molecular beam epitaxy (MBE) on TiO_2 substrates. Our colleagues Hanjong Paik and Professor Darrell Schlom at Cornell University generously provided the samples to us. In their growth setup, vanadium and distilled ozone were co-deposited onto the (001) TiO_2 substrate held at 250 °C under a distilled ozone background pressure of 1.0×10^{-6} Torr. The vanadium flux was calibrated to be in the range of $2\text{-}3 \times 10^{12}$ atoms/cm^{2}sec, a very small value, resulting a film growth rate at about 0.012-0.015 Å/sec. They also noticed that the hydrogen partial pressure must be very low (less than 4 × 10^{-9} Torr) to achieve a sharp metal-to-insulator transition, implying the influence of hydrogen in the VO_2 material. Through shadow masking, we were able to deposit six contacts (5nm vanadium and 35nm gold) on the four edges of a 0.5cm *0.5cm VO_2 film sample to form a Hall bar structure (figure 6.1a).

The other two kinds of samples were VO_2 nanobeams and micron-scale flakes, both grown by physical vapor deposition on Si/SiO_2 substrates as described in section 1.2. The length of wires could be up to 100 μm, and the width and thickness ranged from 50 nm to 1 μm. As for the flakes, the thickness was between 50 nm to 100 nm, and the lateral size was tens of microns by tens of microns. Usually, both wires and flakes could be achieved on one substrate from the same batch of growth, implying the similarity of their properties. We used electron-beam lithography to define the four-contact patterns, and deposited 5nm vanadium and 35 nm gold as contacts (figure 6.1b, c). Devices with 4 contacts were made for 4-terminal transport measurement to minimize the effects of contact resistance. We intentionally chose beams and flakes less than 200 nm thick, so that the gold contacts could keep good connection across the side of the VO_2 samples.

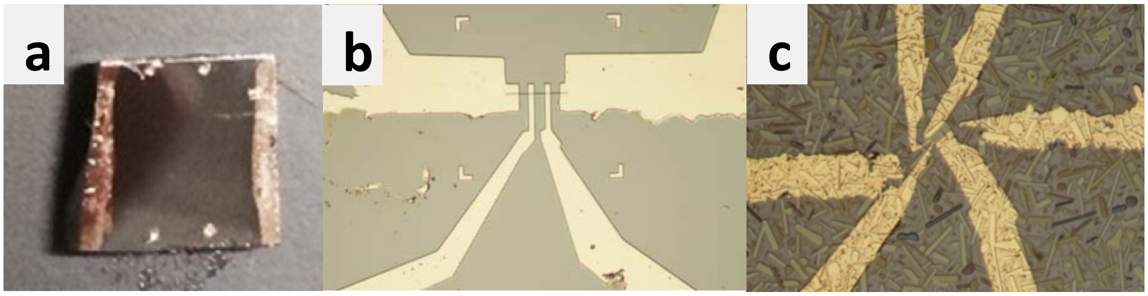

Figure 6.1 Image of three kinds of samples: (a) The VO_2 film device with 6 contacts to form a Hall bar structure. (b) The VO_2 nanobeam device with 4 contacts. (c) The VO_2 micro flake device with 4 contacts. (The additional two gold leads are from scratch marks.)

After an initial temperature-dependent resistivity measurement (from 200K to 400K) of the pristine samples, all devices were then treated by the atomic hydrogenation process introduced in section 4.2. The reason we used atomic hydrogenation instead of the catalytically assisted method is that these catalysts (e.g. Au or Pd) could affect the transport measurement. Even though the existence of sparse and non-continuous metal particles on top of VO_2 samples will not reduce the resistance dramatically, the extra surface effects like spin-orbital scattering could affect the magneto-resistance. Since the VO_2 film on TiO_2 substrate had a phase transition temperature at about 290K, due to the compressive strain, the atomic hydrogenation process could happen readily at room temperature. The c_R-axis of the film, which is the preferred diffusion axis of hydrogen, was perpendicular to the substrate, so the length of the c_R-axis was equal to the thickness of the film, 30nm. Thus the process took no more than 2 minutes to complete. On the other hand, for the wires and flakes, the hydrogenation furnace had to be turned on to lift the ambient temperature to 425K, so that the VO_2 samples could turn into the rutile structure. Also, because the c-axis was along the longitudinal direction of the wires or along the long side of the flakes, it usually took 15 minutes for the VO_2 samples to be (apparently) fully hydrogenated.

All the transport measurements were done in a Quantum Design Physical Property Measurement System (PPMS), with a base temperature of 1.8K, and magnetic field up to 9T. A typical 4-terminal measurement setup was applied for all the temperature-dependent resistivity and magneto-resistance measurements. A low frequency (17Hz) AC signal was provided and measured by two lock-in amplifiers (Signal Recovery model 7270 and model 7265), one current pre-amplifier (Stanford Research System model SR570) and one voltage pre-amplifier (Stanford Research System model SR560). For Hall measurements, one additional voltage pre-amplifier was used to monitor the Hall voltage. In all the transport measurements, except the one of pristine VO_2 in the insulating phase, a current source of less than 1 μA was used to minimize the effect of Joule heating.

6.3. Weak localization and related effects

6.3.1. Weak localization (WL)

Before discussing the transport measurements of VO_2 film, I want to give a brief introduction to weak localization (WL), which will be used to explain some of our later data. Weak localization is a theory used to explain some abnormal temperature dependent resistance and magneto-resistance observed in weakly disordered electronic systems (e.g., polycrystalline metals, doped semiconductors) at low temperature. Gerd Bergmann wrote a good review article in 1983 [57] to describe its existence and effect in 2D systems. Here, I will briefly describe the physical picture of WL based on conventional understanding.

In an ordinary metal or n-type semiconductor, the low energy electronic excitations are electron-like quasiparticles with spin ½ and charge $-e$. These quasiparticles are typically separated from the filled electronic states of the Fermi sea by an energy $\sim k_B T$ and can be described in momentum space as having a well-defined wavevector $\boldsymbol{k}$, with $|\boldsymbol{k}| \cong k_F$. These conduction electrons move under the influence of an external electric field and experience different kinds of scattering, broadly divided into two classes, elastic scattering and inelastic scattering, evaluated by their scattering times τ_e and τ_i respectively. During elastic scattering, electrons change $\boldsymbol{k}/|\boldsymbol{k}|$ (i.e. direction of motion), but not $|\boldsymbol{k}|$ and therefore energy. Purely potential scattering can introduce a well-defined shift to the quantum phase of the propagating quasiparticle (otherwise given by $\boldsymbol{k}\cdot\boldsymbol{L}$, where $\boldsymbol{L}$ is the distance propagated), but maintains phase coherence. Elastic scattering is usually caused by deviations from the lattice symmetry by impurities or grain boundaries in the material; therefore, τ_e has little temperature dependence. On the other hand, inelastic scattering changes the energy of electrons. Since different quasiparticles can end up with differing $|\boldsymbol{k}|$ and differing scattering phase shifts, phase coherence is disrupted by inelastic scattering. Inelastic scattering at high temperature is mostly caused by phonons, while at lower temperatures electron-electron scattering can contribute significantly, so τ_i generally obeys the temperature dependence law $\tau_i \propto T^{-P}$, where P is determined by the scattering mechanism and the dimensionality of the system. At high temperature where τ_i is smaller than τ_e, nothing exciting happens, and the Drude formula gives the model of conductivity $\sigma = (ne^2\tau_i)/m$, where n is conduction electron density and m is the effective mass of the electronic quasiparticle. However, when the temperature decreases to a point where $\tau_i >> \tau_e$, weak localization appears. In this situation, electrons can experience a series of elastic scattering events without losing their phase, leading to an enhanced possibility of backscattering (i.e. direction of motion flipped by 180 degrees) or localization.

In quantum mechanics, the sum of the probabilities of two states without phase coherence is found by adding up the intensities of their amplitude, i.e. $|A|^2+|A|^2=2|A|^2$, assuming the two states each have the amplitude A. However, when the two states have the same phase, the sum is calculated by adding up their amplitudes, leading to a new state with amplitude equal to $2A$, and thus the intensity of the new state is $|2A|^2$, i.e. $4|A|^2$. Because of quantum interference due to cross terms, phase coherence can lead to total probabilities that differ strongly from the classical results. Statistically, any backscattering trajectory built by a series of elastic scattering events from static disorder can be reproduced by another series of scattering events with the opposite order, and both of these scattering paths should have the same probability for carriers to experience. Figure 6.2a shows the scheme of backscattering in momentum space. As a result, the possibility of the backscattering, which is the intensity of the summed states of the two backscattering paths, is doubled relative to the classical sum-of-probabilities result by the constructive interference. Increased backscattering relative to the classical result means greater difficulty for electrons to move in real space along the direction of the electric field, causing a decrease of the conductance of the material. This result can be depicted in real space, which considers the doubled probability of an electron staying at the origin point, instead of backscattering. In this model (figure 6.2b), the electron can move back to its origin point after propagating along a loop. The clockwise movement and counterclockwise movement have the same probability, which leads to an enhanced intensity of the summed state, which is the probability of the electron staying at point 0 in figure 6.2b. This localization effect decreases the mobility of electrons, thus decreasing the conductance.

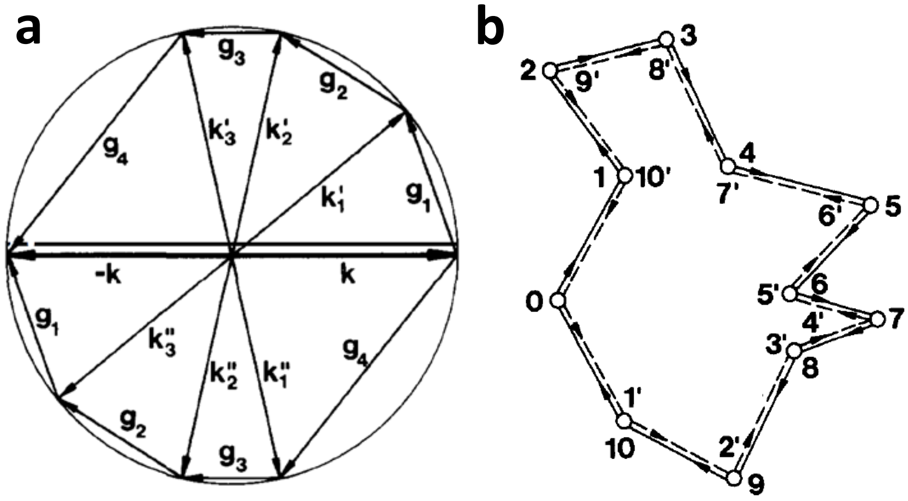

Figure 6.2 Schemes of weak localization. (a) is in momentum space, and (b) is in real space. [57]

Provided these explanations, it is easy to answer the question why weak localization is usually observed in a weakly disordered metal thin film at low temperatures. First, disorder provides enough elastic scattering to bring down the value of $\tau_{e.}$ Second, the thin film, a 2D system, limits the scattering direction, resulting in more chances of backscattering. Note that low temperatures are required to observe this effect, because inelastic scattering must be sufficiently suppressed that the electron's phase remains well-defined while traversing such loop trajectories.

At low temperature, the weak localization can cause an upturn of resistance as a function of temperature (figure 6.3a) and a negative magneto-resistance (top part of figure 6.3b). The former phenomenon is easy to understand after the previous explanation. The latter one is a result of the breakdown of the phase coherence, induced by the magnetic field. After passing along the loop (figure 6.2b) in the presence of an external magnetic field, the clockwise and counterclockwise movements now have a phase difference of $2e\varphi/\hbar$ caused by the electron's coupling to the magnetic field via the Aharonov-Bohm effect [58], where $\varphi = A$ (area of the loop) * B (strength of the field) is the magnetic flux. Therefore, the constructive interference is restrained, leading to a reduced resistance in the existence of magnetic field.

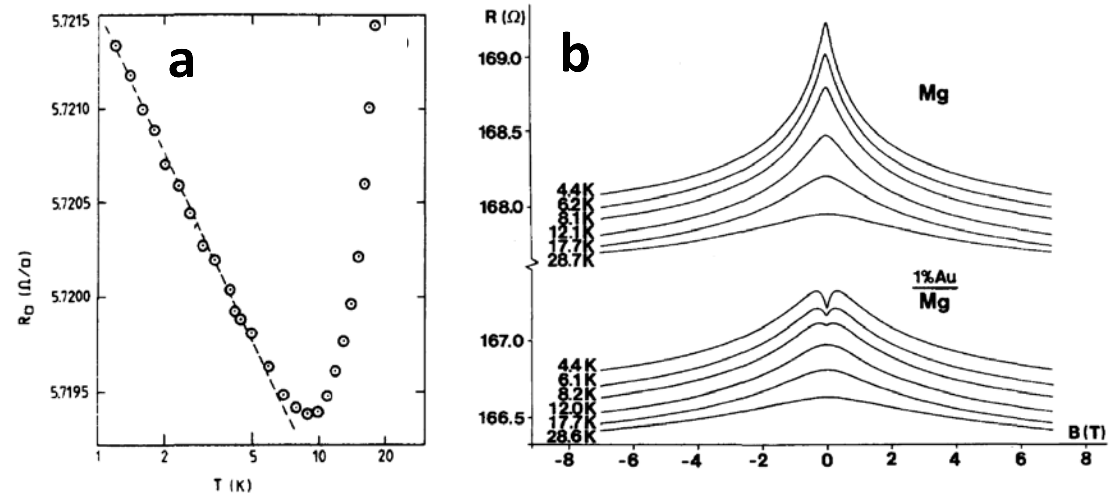

Figure 6.3 Effect of weak localization [57]. (a) Temperature dependent resistance measurement. The resistance of a Cu film increases as temperature decreases below 5K. (b) Magneto-resistance measurement. The MR of a Mg film shows a negative response (top part), however, when 1% Au is doped, a little positive response shows up at 4.4K when magnetic field is below 0.5 T.

6.3.2. Weak anti-localization (WAL)

With slight modification, the same physical picture can be used to interpret weak *anti*-localization (WAL). In a case where the two states have a phase difference of half of the period (for example π, if the period is 2π), the new state will vanish due to the resulting amplitude equal to A – A = 0. In this situation backscattering is suppressed due to destructive interference. In an electronic system with strong spin-orbit scattering, the previously constructive phase difference, 2π, between two paths becomes destructive in terms of spin state. Therefore, the sign of both temperature dependence of resistance and the magneto-resistance (small field region of the Au/Mg curve in figure 6.3b) are opposite from the ones in weak localization. Usually, the elements with larger atomic number Z have stronger spin-orbit coupling: for example, in this case, the spin-orbit coupling of Au (Z=79) is much larger than that of Mg (Z=12). Even a small amount of Au contamination (1%) is enough to cause significant spin-orbit scattering. For a pure Au film, the positive magneto-resistance can extend to a much larger magnetic field (not shown here).

6.3.3. Mott-Ioffe-Regel limit

In 1960, Ioffe and Regel [59], followed by Mott in 1972 [60], discussed transport properties of quasiparticles in the situation when the mean free path (l) was comparable to or even shorter than the lattice constant (a), and provided a criteria of $k_F l \sim 1$ (or 2π) to judge the applicability of Boltzmann transport model. This Mott-Ioffe-Regel limit (MIRL) then gives a maximum resistivity of metals in conventional model: $a\hbar/e^2$ ($\sim 41a$ μΩ·cm, where a is in unit of Å). However, the violation of MIRL has been observed in some transition metal oxides, like VO_2 [61], and some high-T_c superconducting oxides, like Sr_2RuO_4 [62], at high temperature. In the case of Sr_2RuO_4, its resistivity goes beyond 1000 μΩ·cm without saturation, and the inferred l shrinks down to less than 1 Å, when the temperature is reaching 1300 K. The high-temperature transport properties of these materials were discussed by Emery and Kivelson [63], who defined them as "bad metal", however the mechanism has not been completely understood yet.

The reason I mentioned MIRL here is that our hydrogenated VO_2 sample can maintain the resistivity on the order of 10^3 μΩ·cm from 300 K to 2 K. Considering the fact that few observation of violation of the MIRL at low temperature has been reported, the behavior of this conducting VO_2 at low temperature is intriguing. It is important to note that the perturbative theories of WL/WAL are derived assuming $k_F l >>1$. The quantitative analysis of apparent WL/WAL in the $k_F l$ <~ 1 regime in is then not trivial, since that regime is theoretically expected to show a crossover to strong Anderson localization.

6.4. Results of VO_2 film

6.4.1. Temperature dependence of resistivity

Before hydrogen doping, VO_2 film shows a typical phase transition behavior (figure 6.2a) with transition temperature at around 290K, instead of 340K. This phenomenon has been reported before, and can be well explained by a compressive strain along the c_R-axis [64]. After the room-temperature atomic hydrogenation process, the film stays in a conducting state with a resistivity similar to that of the pristine metallic state. Although, unlike a typical metal, the temperature dependence of resistivity shows a negative slope, the total change of resistivity is less than an order of magnitude from 300K to 2K (figure 6.4). This could also be due to a strain effect according to the discussion we have in section 3.4 and figure 3.8.

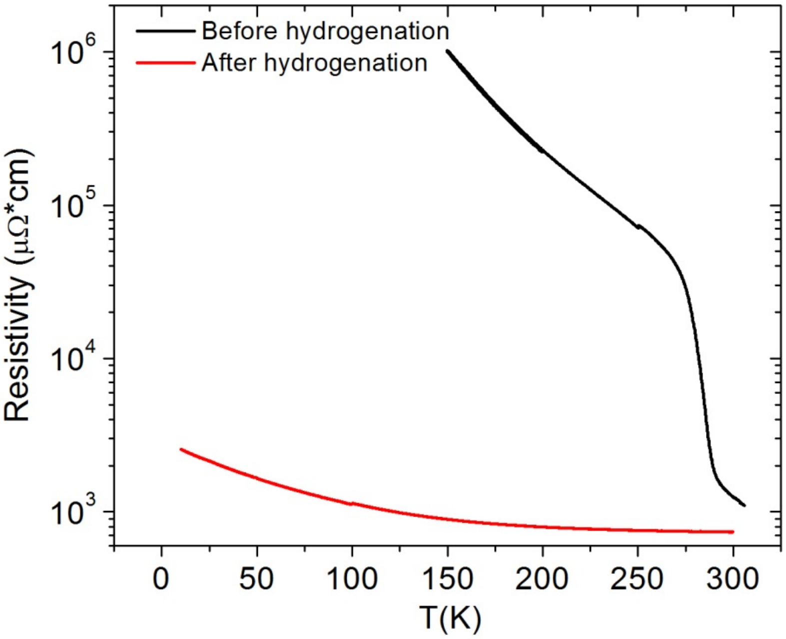

Figure 6.4 Temperature dependence of resistivity of VO_2 film before and after hydrogenation.

For VO_2, the lattice constant *a* is 2.85 Å [61] along c_R-axis. Based on the introduction in section 6.3.3, MIRL gives a maximum resistivity at around 100 μΩ·cm. Even considering a possible factor of 2π, this criteria is at most 600 μΩ·cm. However, in our measurement, the resistivity of the hydrogenated VO_2 film is larger than 700 μΩ·cm throughout the temperature range from 300 K to 2K, implying an unconventional conducting mechanism in VO_2.

6.4.2. Magneto-resistance measurement

We performed magneto-resistance measurements as a function of temperature (figure 6.5a). Clearly, a negative MR gradually appears when the temperature decreases below 25K. Figure 6.5b shows the relative percent change of resistance $(R(H)\text{-}R_0)/R_0$, where R_0 is the resistance in zero field. At 2K this relative change can reach 1% with a 7T magnetic field.

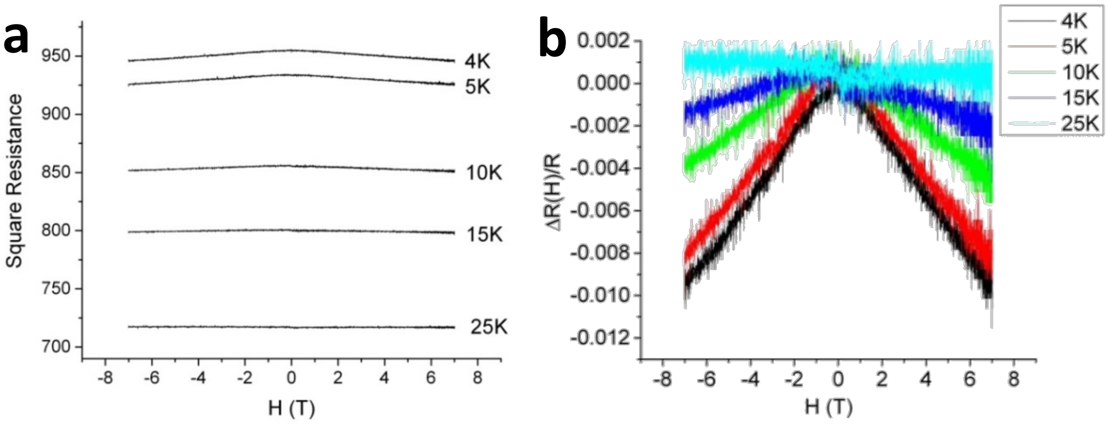

Figure 6.5 Magneto-resistance of VO_2 film in (a) absolute value and (b) relative value.

This magnitude of modulation can be well explained by the weak localization effect described above. Based on the model of weak localization in a 2D system provided by Hikami [65], MR is a useful tool to estimate the various scattering times in a conducting system. Equation 6.1 gives their relationship:

$$\frac{\Delta R(H)}{R^2} = \frac{e^2}{2\pi^2\hbar}\left[\psi\left(\frac{1}{2}+\frac{H_1}{H}\right)+\frac{1}{2}\psi\left(\frac{1}{2}+\frac{H_3}{H}\right)-\frac{3}{2}\psi\left(\frac{1}{2}+\frac{H_2}{H}\right)\right] \qquad \text{equation 6.1}$$

, where R is square resistance of the film, $\psi()$ is digamma function, and $H_{1,2,3}$ is defined as:

$$\mathrm{H}_1 = \mathrm{H}_\mathrm{e} + \mathrm{H}_\mathrm{so} + \mathrm{H}_\mathrm{s}\ ,$$

$$\mathrm{H}_2 = \mathrm{H}_\mathrm{i} + \frac{4}{3}\mathrm{H}_\mathrm{so} + \frac{2}{3}\mathrm{H}_\mathrm{s}\ ,$$

$$\mathrm{H}_3 = \mathrm{H}_\mathrm{i} + 2\mathrm{H}_\mathrm{s}\ ,$$

$H_{e,so,s,i}$ is inversely proportional to the respective scattering time: $H_x=\hbar/(4eD\tau_x)$, where D is the electronic diffusion constant. Here τ_e and τ_i are the elastic and inelastic scattering times respectively, τ_{so} is the spin-orbit scattering time, and τ_s is the magnetic impurity scattering time.

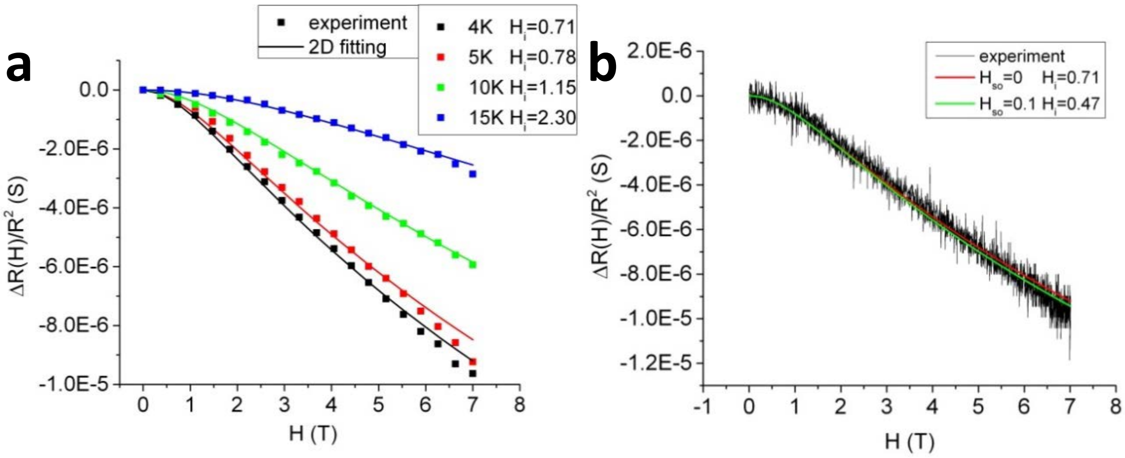

Figure 6.6 (a) Experimental MR data (squares) at different temperature and their corresponding fitting curves (line). (b) Two fitting curves of the raw MR data at 4K using two sets of parameters.

After smoothing the raw data, 20 data points were extracted from each MR curve (only the positive magnetic field side) at each temperature. Then, equation 6.1 was used to fit the experimental result (figure 6.6a). The H_{so} and H_i parameters were set to 0, since no weak anti-localization behavior is observed. H_e has little effect to the shape of the curve once it is much larger than H_i, so it is set to be 20T for all the fitting. H_i was the only parameter adjusted here, varying from 0.71 T (at 4K) to 2.3 T (at 15K). The fitting curves matched the experimental data very well for external fields below 5 T, but gradually deviated at high magnetic field.

We also found that different combinations of parameters could achieve similar fitting quality. The raw MR data at 4K was fitted by two sets of parameters (figure 6.6b). Even with very different spin-orbit scattering time and inelastic scattering time, the curves do not differ from each other very much, and both sit within the range of the noise of the raw data. Generally, an increasing value of H_{so} will decrease the value of H_i (and later in section 6.5, we will find H_{so} should not be 0 in hydrogenated VO_2). Considering the uncertainty of the measurement due to signal-to-noise, it is difficult to confidently pick a perfect set of fitting parameters; however, it is physically reasonable to set H_{so} as a constant, because then the trend of the temperature dependence of inelastic scattering time will be monotonic. A clear increase of τ_i with temperature decreasing agrees well with the prediction of the model of a disordered metal, though the value is smaller.

There is also a critical thickness that determines the applicability of the 2D weak localization model, which requires the thickness of the sample

$$d \ll \sqrt{\hbar/(4eH_i)} = \sqrt{D\tau_i}$$

In our case, the smallest H_i deduced previously is around 0.47 T when the temperature is 4 K. As a result, the critical thickness $\sqrt{\hbar/(4eH_i)}$ is at most 19 nm, meaning the thickness of our film sample (30 nm) is larger than this critical thickness even when T is as low as 2K. Therefore, our VO_2 film is actually in the 3D limit, and the 2D model we use here may not accurately reflect the properties of the system.

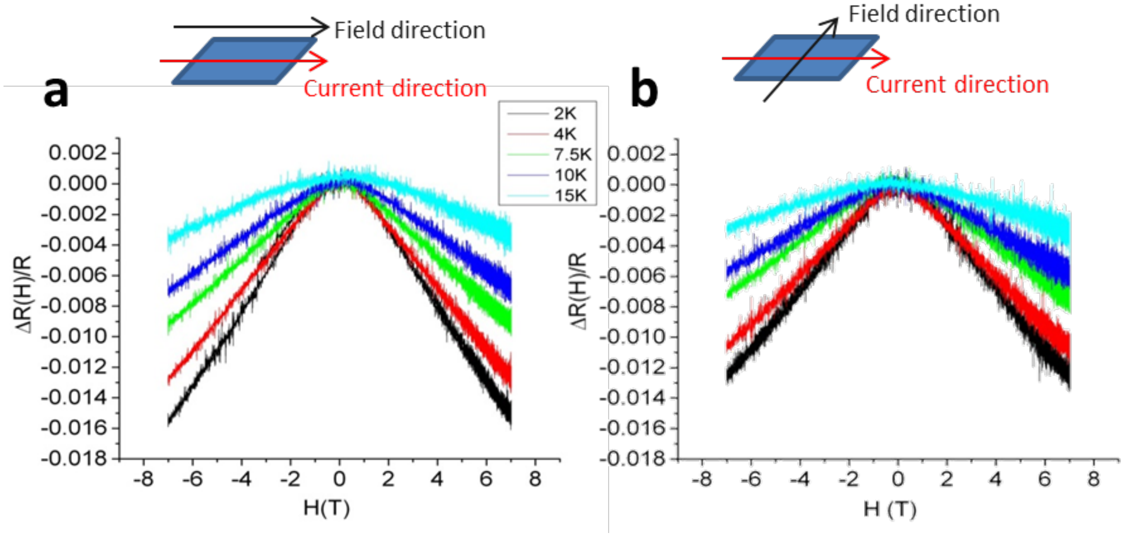

Figure 6.7 MR measurements with in-plane magnetic field. (a) Field parallel to the current, (b) field perpendicular to the current.

Further MR measurements with in-plane magnetic field support this conclusion. Figure 6.7 shows the MR measurements of VO_2 film with an in-plane field (a) parallel to the current and (b) perpendicular to the current. The magnitude of the change of resistance is similar to the result seen when applying an out-of-plane field. Since all the VO_2 films we have with a thickness smaller than 30 nm show a relatively poor phase transition (less than 2 orders of magnitude in change of resistance), implying a lower quality, we do not further investigate the dimensionality dependence of the weak localization in VO_2 films. However, considering the fact that the sample thickness is larger than the 2D critical thickness, an upper limit of the inelastic scattering time τ_i can been achieved for temperature as low as 4K: $\tau_i < d^2/D \approx 2 \times 10^{-12}$ s, where d is 30 nm, and D is chosen to be 5 cm^2/s according to ref [66]. This value is still much smaller than expected for a normal metal (10^{-11} s) [67]. The theoretical analysis in 3D limit is still ongoing, and will be presented in the future publication.

6.4.3. Hall measurement

We also did Hall measurements on hydrogenated VO_2 films. Similar to the results for pristine VO_2 films in the metallic state reported by other groups [68], a very small Hall signal is observed here at room temperature (figure 6.8). As temperature decreases, the Hall voltage becomes larger. Conventionally, this implies a decrease in carrier density. No matter how the temperature changes, the sign of the Hall coefficient stays the same, indicating the dominance of n-type carriers (electrons).

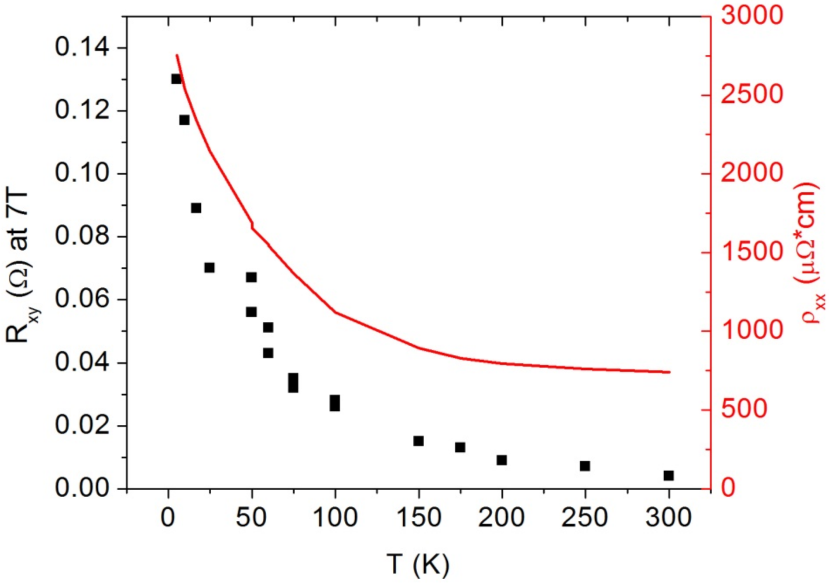

Figure 6.8 Hall resistance $R_{xy}=V_H/I$ as a function of temperature. Temperature dependence of resistivity (the same as the red curve in figure 6.4) is also plotted here for comparison.

Assuming that the system is dominated by n type carriers, we are able to deduce the Hall carrier density n and mobility μ from the Hall measurements and the resistivity, according to the equations:

$$n = \frac{IB}{V_H ed} \qquad \text{equation 6.2}$$

$$\mu = \frac{1}{en\rho} \qquad \text{equation 6.3}$$

, where *I* is the current, *B* is the magnetic field, V_H is the Hall voltage, *d* is the thickness of the sample, and ρ is the resistivity.

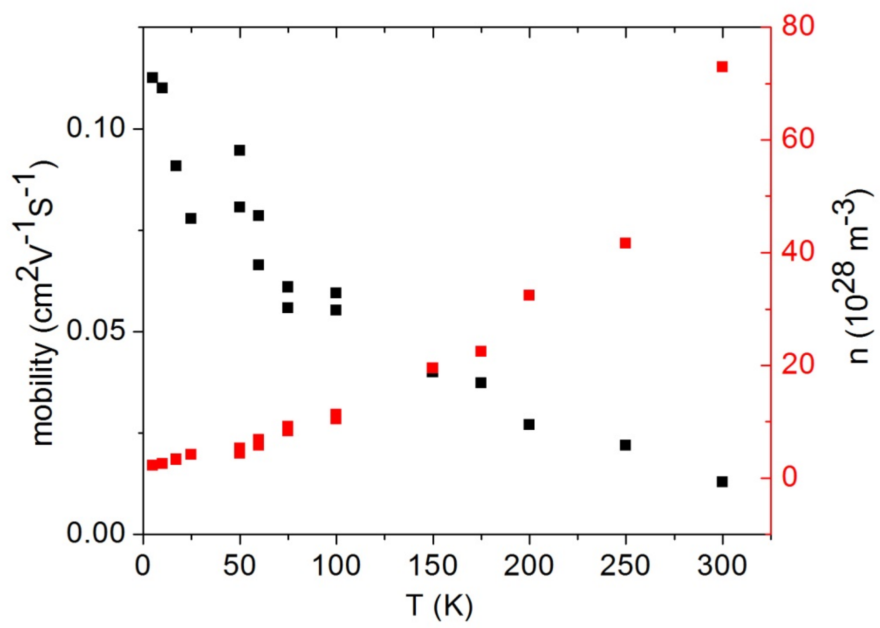

Figure 6.9 Temperature dependence of mobility μ and carrier density n deduced from the Hall measurements.

The temperature dependence of deduced n and μ is presented in figure 6.9. The extremely small Hall voltage leads to an extraordinarily high calculated carrier density, further resulting in an extremely small calculated value of mobility. At room temperature, the deduced n is about 73×10^{28} m^{-3}, much larger than the density of vanadium atoms (~3×10^{28} m^{-3}). Even at 2K where n reaches the minimum in the limit of our measurement setup, the value is still as large as 2×10^{28} m^{-3}. All these results suggest that our assumption of single carrier type is incorrect, and thus both n-type and p-type carriers are present in this system, with comparable contribution to the conductances. The Hall voltage in this case is given by [69]:

$$V_H = \frac{IB}{ed}\frac{(p{\mu_p}^2 - n{\mu_n}^2)}{(p\mu_p - n\mu_n)^2} \qquad \text{equation 6.3}$$

, where n (μ_n) and p (μ_p) are the density (mobility) of n-type and p-type carriers respectively. In our experiment, since there is no method to further measure and distinguish the two kinds of carriers, we cannot deduce their respective carrier densities. A similar conclusion is also reported recently by Dmitry Ruzmetov *et al.* [68]. The electronic structure of doped (or even conventionally metallic rutile) VO_2 remains a subject of debate.

6.5. Measurement of VO_2 nanobeams

As a comparison, the temperature dependence of resistance and the magneto-resistance of hydrogenated VO_2 nanobeams were also measured under the same conditions. The resistance of a representative sample shows a non-monotonic temperature dependence (figure 6.10a). The resistance gradually increases as the temperature decreases from 300K to 140K, and reaches a maximum point at 140K, however, the total change is less than 20%, and thus is quite different from the temperature dependence of resistance of a semiconductor. Below 140K, the resistance decreases with cooling, similar to the behavior of a metal. We believe that this transferred nanobeam is under tensile strain (due to direct contact with the substrate), in contrast to the VO_2 film grown on TiO_2 substrate, which has a much stronger compressive strain.

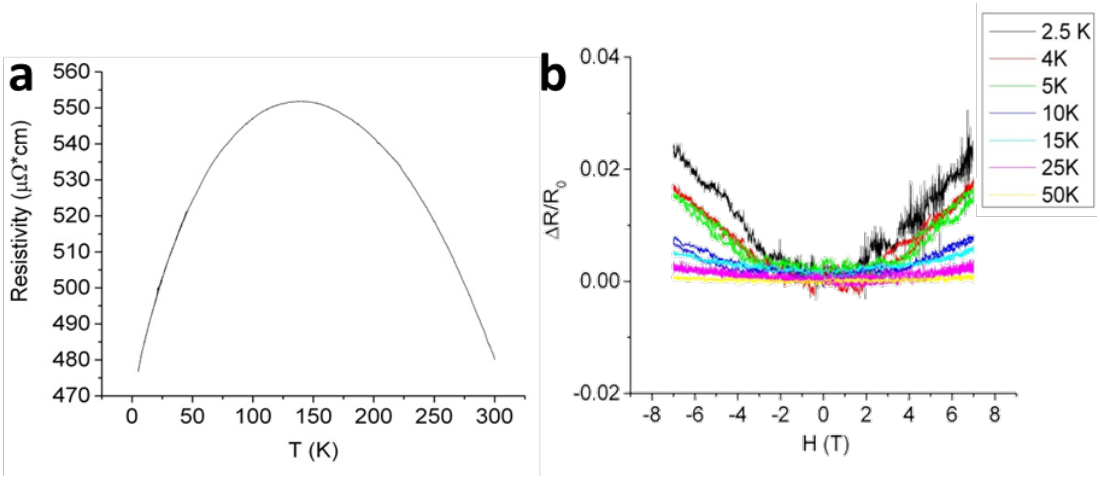

Figure 6.10 (a) Temperature dependence of resistivity of VO_2 nanobeam, (b) the MR measurement shown in relative change.

However, the magneto-resistance of the VO_2 nanobeam shown in figure 6.10b has a completely opposite response compared with the film case, as the resistance slightly goes up with the presence of magnetic field when the temperature is below 25K. Since the width and thickness of the nanobeam are both more than 50nm, it is reasonable to suspect that the nanobeam is a 3D system based on the criteria calculated previously in the film case. The MR measurement with the magnetic field parallel to the current indeed shows the same rough magnitude of change as the perpendicular case, confirming this guess (data is not shown here). A positive magneto-resistance has been reported before in VO_2 films at room temperature (in the insulating phase) [68], and also in some other vanadium oxide compounds at low temperatures [66]. However, these experiments cannot be taken as a convincing comparison or analog for our measurement. The former measurement performed by Dmitry Ruzmetov *et al.* is at room temperature where

VO_2 is in the insulating phase, thus the crystal structure and electronic properties of the sample are totally different from those of our hydrogenated VO_2 nanowires. Also, the positive MR they observed cannot be explained by weak anti-localization effect, which only shows up at low temperature. The latter experiment [66] shows a crossover from a positive MR to a negative MR when the temperature changes from 5K to 1.5K. Although this experiment is still quite different from ours, due to the unknown compound of the material measured, the appearance of positive MR at low temperature at least suggests the possibility of weak anti-localization, and implies that vanadium may possess strong enough spin-orbit scattering to observe WAL. This is not surprising, considering the positive MR observed in copper film [57] whose atomic number (Z=29) is only slight larger than that of vanadium.

Even though the positive MR of VO_2 nanobeams may be interpreted as a consequence of weak anti-localization, the reason for the opposite MRs observed in film and nanobeam samples is still unclear. There are two significant differences between these two kinds of samples: strain direction and current direction with respect to the c_R-axis. The difference of strain directions has been mentioned above, and is clear from the fact that the phase transition temperature shifts to opposite directions in these two samples. For the latter difference, it may be critical if the hydrogenated VO_2 has anisotropic electronic properties. We have seen plenty of evidence suggesting that the c_R-axis is a special direction in VO_2. For films, the current is in-plane, and the c_R-axis is perpendicular to the plane, therefore, the current is perpendicular to the c_R-axis. In nanobeams, however, the current is parallel to the c_R-axis. To investigate the possible existence of anisotropy, VO_2 flake samples are measured.

6.6. Measurement of VO_2 micro flakes.

The c_R-axis of the VO_2 micro flakes can be determined by optical microscopy, because the domains formed during the phase transition are always in a stripe shape perpendicular to the c_R-axis (discussed in section 1.4.1). Generally, the c_R-axis is along the long side of rectangular VO_2 flakes. To fabricate the device, 4 V/Au contacts were deposited along the short side of the flake, so that the current would be perpendicular to the c_R-axis, in contrast to the nanobeam measurement (inset in figure 6.11a). Although the VO_2 flakes remain on their growth substrate, and thus are supposed to have larger strain than transferred VO_2 nanobeams, the hydrogenated flake sample shows a monotonic positive temperature dependent resistance (figure 6.11a), similar to a metal.

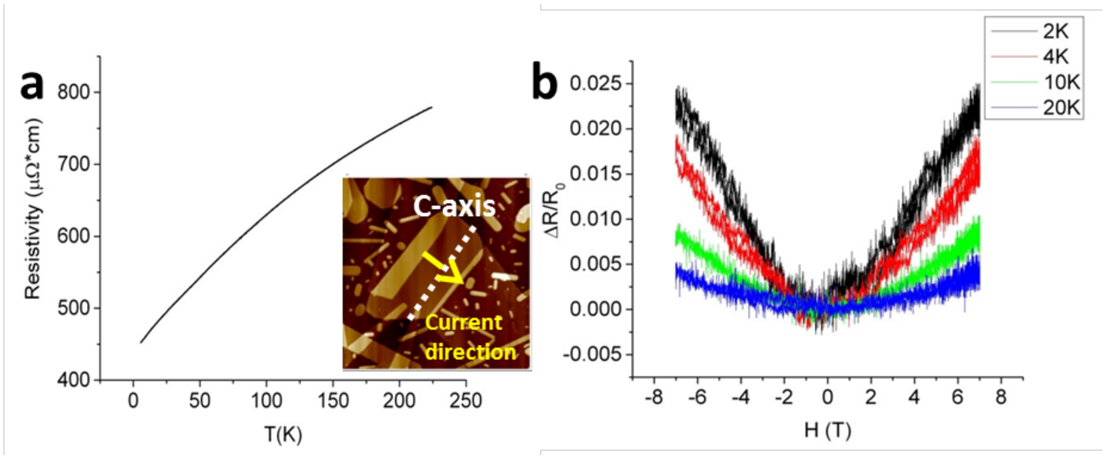

Figure 6.11 (a) Temperature dependence of resistivity of VO_2 micro flake. The inset is the AFM image of the device, marked with its c_R-axis and current direction. (b) The MR measurement shown in relative change.

The MR measurement of the flake sample shows a positive response again (figure 6.11b), similar to the nanobeam device. Because now the current direction is perpendicular to the c_R-axis, it essentially rules out the possibility that the different MR response is caused by anisotropy.

6.7. Conclusion

In this chapter, we studied the low temperature transport properties of hydrogenated VO_2 grown by different methods. The VO_2 films grown by MBE on TiO_2 (001) substrates show a negative magneto-resistance when T<25K, and the magnitude of the change persists no matter how the direction of the magnetic field changes. Using a weak localization model, we are able to deduce an upper limit for the inelastic scattering time τ_i at 4K to be ~10^{-12} sec, based on the fact that the 30nm thick film is actually a 3D system from a weak localization point of view. On the other hand, the MR measurements of VO_2 nanobeams and micro flakes grown by PVD on Si/SiO_2 substrates show a positive response, opposite to the measurement of the film sample. This positive MR could be explained by weak anti-localization as a result of the appearance of spin-orbit scattering, however, it remains uncertain what causes such difference. Excluding the anisotropy, the most probable reason is the opposite strain produced in the two growth methods. At the same time, the Hall measurements of the hydrogenated VO_2 film sample at different temperatures confirm the extremely small Hall coefficient reported before [68], suggesting the co-existence of both n-type and p-type carriers.

Chapter 7

7. Final remarks and future directions

Though our work on VO_2 did not provide an explicit answer to the debate of Peierls or Mott transition, we found a new hydrogenation method to modulate the electronic and structural properties of VO_2, and contributed on other aspects of this material, like hydrogen concentration diagram and low-temperature electronic transport properties.

Potential applications can be developed based on this easily ~~occurred~~ achieved hydrogen doping process, such as hydrogen sensors and hydrogen storage.

Moreover, this hydrogen doping technique can be applied on other rutile structure materials or layered materials with somewhat large layer-to-layer spacing for hydrogen intercalation. My colleague Will Hardy has attempted to treat some materials, like $TiSe_2$, using this technique, and has gotten some preliminary results. We expect a broader usage of this technique.

H-doped VO2 is an example of a peculiar system that exhibits low temperature transport in a regime with $k_F l$ <~ 1, yet without obvious signs of a crossover to strong localization or a new phase with magnetic or superconducting order. Quantum transport in such "bad" or "strange" metals is essentially unexplored. Future experiments in this regime may shed light on how we should think about the long-lived, low energy excitations of systems where the ordinary $k_F l$ >> 1 view of quasiparticles is no longer applicable.

References

1. Morosan, E., et al., *Strongly Correlated Materials.* Advanced Materials, 2012. **24**(36): p. 4896-4923.
2. Morin, F.J., *Oxides Which Show a Metal-to-Insulator Transition at the Neel Temperature.* Physical Review Letters, 1959. **3**(1): p. 34-36.
3. Rini, M., et al., *Photoinduced phase transition in VO2 nanocrystals: ultrafast control of surface-plasmon resonance.* Optics Letters, 2005. **30**(5): p. 558-560.
4. Guiton, B.S., et al., *Single-Crystalline Vanadium Dioxide Nanowires with Rectangular Cross Sections.* Journal of the American Chemical Society, 2005. **127**(2): p. 498-499.
5. Eyert, V., *The metal-insulator transitions of VO2: A band theoretical approach.* Annalen der Physik, 2002. **11**(9): p. 650-704.
6. Goodenough, J.B. and H.Y.P. Hong, *Structures and a Two-Band Model for the System V1-xCrxO2.* Physical Review B, 1973. **8**(4): p. 1323-1331.
7. Gu, Q., et al., *Current-Driven Phase Oscillation and Domain-Wall Propagation in WxV1-xO2 Nanobeams.* Nano Letters, 2007. **7**(2): p. 363-366.
8. Marezio, M., et al., *Structural Aspects of the Metal-Insulator Transitions in Cr-Doped VO2.* Physical Review B, 1972. **5**(7): p. 2541-2551.
9. Pouget, J.P., et al., *Electron Localization Induced by Uniaxial Stress in Pure VO2.* Physical Review Letters, 1975. **35**(13): p. 873-875.
10. Park, J.H., et al., *Measurement of a solid-state triple point at the metal-insulator transition in VO2.* Nature, 2013. **500**(7463): p. 431-434.
11. Mott, N., *On metal-insulator transitions.* Journal of Solid State Chemistry, 1990. **88**(1): p. 5-7.
12. Zylbersztejn, A. and N.F. Mott, *Metal-insulator transition in vanadium dioxide.* Physical Review B, 1975. **11**(11): p. 4383-4395.
13. Peierls, R., *Quantum Theory of Solids.* Oxford University Press, 1955.
14. Rice, T.M., H. Launois, and J.P. Pouget, *Comment on "VO2: Peierls or Mott-Hubbard? A View from Band Theory".* Physical Review Letters, 1994. **73**(22): p. 3042-3042.
15. Laverock, J., et al., *Photoemission evidence for crossover from Peierls-like to Mott-like transition in highly strained VO2.* Physical Review B, 2012. **86**(19): p. 195124.
16. Kim, H.-T., et al., *Monoclinic and Correlated Metal Phase in VO2 as Evidence of the Mott Transition: Coherent Phonon Analysis.* Physical Review Letters, 2006. **97**(26): p. 266401.
17. Biermann, S., et al., *Dynamical Singlets and Correlation-Assisted Peierls Transition in VO2.* Physical Review Letters, 2005. **94**(2): p. 026404.
18. Eyert, V., *VO2: A Novel View from Band Theory.* Physical Review Letters, 2011. **107**(1): p. 016401.
19. Gatti, M., et al., *Understanding Correlations in Vanadium Dioxide from First Principles.* Physical Review Letters, 2007. **99**(26): p. 266402.

20. Lin, J., et al., *Hydrogen Diffusion and Stabilization in Single-Crystal VO2 Micro/Nanobeams by Direct Atomic Hydrogenation.* Nano Letters, 2014. **14**(9): p. 5445-5451.
21. Ji, H., J. Wei, and D. Natelson, *Modulation of the Electrical Properties of VO2 Nanobeams Using an Ionic Liquid as a Gating Medium.* Nano Letters, 2012. **12**(6): p. 2988-2992.
22. Wilk, G.D., R.M. Wallace, and J.M. Anthony, *High-κ gate dielectrics: Current status and materials properties considerations.* Journal of Applied Physics, 2001. **89**(10): p. 5243-5275.
23. Ruzmetov, D., et al., *Three-terminal field effect devices utilizing thin film vanadium oxide as the channel layer.* Journal of Applied Physics, 2010. **107**(11): p. 114516.
24. Yang, Z., et al., *Dielectric and carrier transport properties of vanadium dioxide thin films across the phase transition utilizing gated capacitor devices.* Physical Review B, 2010. **82**(20): p. 205101.
25. Shimotani, H., et al., *Insulator-to-metal transition in ZnO by electric double layer gating.* Applied Physics Letters, 2007. **91**(8): p. 082106.
26. Ueno, K., et al., *Electric-field-induced superconductivity in an insulator.* Nat Mater, 2008. **7**(11): p. 855-858.
27. UenoK, et al., *Discovery of superconductivity in KTaO3 by electrostatic carrier doping.* Nat Nano, 2011. **6**(7): p. 408-412.
28. Yang, Z., Y. Zhou, and S. Ramanathan, *Studies on room-temperature electric-field effect in ionic-liquid gated VO2 three-terminal devices.* Journal of Applied Physics, 2012. **111**(1): p. 014506.
29. Yuan, H., et al., *High-Density Carrier Accumulation in ZnO Field-Effect Transistors Gated by Electric Double Layers of Ionic Liquids.* Advanced Functional Materials, 2009. **19**(7): p. 1046-1053.
30. Tran, C.D., S.H. De Paoli Lacerda, and D. Oliveira, *Absorption of Water by Room-Temperature Ionic Liquids: Effect of Anions on Concentration and State of Water.* Applied Spectroscopy, 2003. **57**(2): p. 152-157.
31. Sato, T., G. Masuda, and K. Takagi, *Electrochemical properties of novel ionic liquids for electric double layer capacitor applications.* Electrochimica Acta, 2004. **49**(21): p. 3603-3611.
32. Yuan, H., et al., *Hydrogenation-Induced Surface Polarity Recognition and Proton Memory Behavior at Protic-Ionic-Liquid/Oxide Electric-Double-Layer Interfaces.* Journal of the American Chemical Society, 2010. **132**(19): p. 6672-6678.
33. Andreev, V.N., V.M. Kapralova, and V.A. Klimov, *Effect of hydrogenation on the metal-semiconductor phase transition in vanadium dioxide thin films.* Physics of the Solid State, 2007. **49**(12): p. 2318-2322.
34. Kingsbury, P.I., W.D. Ohlsen, and O.W. Johnson, *Defects in Rutile. II. Diffusion of Interstitial Ions.* Physical Review, 1968. **175**(3): p. 1099-1101.
35. Nakano, M., et al., *Collective bulk carrier delocalization driven by electrostatic surface charge accumulation.* Nature, 2012. **487**(7408): p. 459-462.

36. Jeong, J., et al., *Suppression of Metal-Insulator Transition in VO2 by Electric Field–Induced Oxygen Vacancy Formation.* Science, 2013. **339**(6126): p. 1402-1405.
37. Wei, J., et al., *Hydrogen stabilization of metallic vanadium dioxide in single-crystal nanobeams.* Nat Nano, 2012. **7**(6): p. 357-362.
38. Panayotov, D.A. and J.T. Yates, *Spectroscopic Detection of Hydrogen Atom Spillover from Au Nanoparticles Supported on TiO2: Use of Conduction Band Electrons.* The Journal of Physical Chemistry C, 2007. **111**(7): p. 2959-2964.
39. Chippindale, A.M., P.G. Dickens, and A.V. Powell, *Synthesis, characterization, and inelastic neutron scattering study of hydrogen insertion compounds of VO2(rutile).* Journal of Solid State Chemistry, 1991. **93**(2): p. 526-533.
40. Wu, C., et al., *Hydrogen-Incorporation Stabilization of Metallic VO2(R) Phase to Room Temperature, Displaying Promising Low-Temperature Thermoelectric Effect.* Journal of the American Chemical Society, 2011. **133**(35): p. 13798-13801.
41. Zhang, S., J.Y. Chou, and L.J. Lauhon, *Direct Correlation of Structural Domain Formation with the Metal Insulator Transition in a VO2 Nanobeam.* Nano Letters, 2009. **9**(12): p. 4527-4532.
42. Srivastava, R. and L.L. Chase, *Raman Spectrum of Semiconducting and Metallic VO2.* Physical Review Letters, 1971. **27**(11): p. 727-730.
43. Demeter, M., M. Neumann, and W. Reichelt, *Mixed-valence vanadium oxides studied by XPS.* Surface Science, 2000. **454–456**(0): p. 41-44.
44. Silversmit, G., et al., *Determination of the V2p XPS binding energies for different vanadium oxidation states (V5+ to V0+).* Journal of Electron Spectroscopy and Related Phenomena, 2004. **135**(2–3): p. 167-175.
45. Mendialdua, J., R. Casanova, and Y. Barbaux, *XPS studies of V2O5, V6O13, VO2 and V2O3.* Journal of Electron Spectroscopy and Related Phenomena, 1995. **71**(3): p. 249-261.
46. Tang, Y.M. and C.W. Ong, *Elemental and phase composition analysis of hydrogen-sensitive Pd/Mg–Ni films.* Applied Physics A, 2008. **91**(4): p. 701-706.
47. Kačiulis, S., et al., *Surface analysis of biocompatible coatings on titanium.* Journal of Electron Spectroscopy and Related Phenomena, 1998. **95**(1): p. 61-69.
48. Philippin, G., J. Delhalle, and Z. Mekhalif, *Comparative study of the monolayers of CH3□(CH2)n□SiCl3 and CH3□(CH2)n□PO(OH)2, n = 4 and 13, adsorbed on polycrystalline titanium substrates.* Applied Surface Science, 2003. **212–213**(0): p. 530-536.
49. Terakura, K., et al., *Band theory of insulating transition-metal monoxides: Band-structure calculations.* Physical Review B, 1984. **30**(8): p. 4734-4747.
50. Yamashita, J. and S. Asano, *Cohesive Properties of Alkali Halides and Simple Oxides in the Local-Density Formalism.* Journal of the Physical Society of Japan, 1983. **52**(10): p. 3506-3513.

51. Koudriachova, M.V., S.W. de Leeuw, and N.M. Harrison, *First-principles study of H intercalation in rutile TiO2.* Physical Review B, 2004. **70**(16): p. 165421.
52. Bates, J.B., J.C. Wang, and R.A. Perkins, *Mechanisms for hydrogen diffusion in TiO2.* Physical Review B, 1979. **19**(8): p. 4130-4139.
53. Johnson, O.W., S.H. Paek, and J.W. DeFord, *Diffusion of H and D in TiO2: Suppression of internal fields by isotope exchange.* Journal of Applied Physics, 1975. **46**(3): p. 1026-1033.
54. Spahr, E.J., et al., *Giant Enhancement of Hydrogen Transport in Rutile TiO2 at Low Temperatures.* Physical Review Letters, 2010. **104**(20): p. 205901.
55. Warnick, K.H., B. Wang, and S.T. Pantelides, *Hydrogen dynamics and metallic phase stabilization in VO2.* Applied Physics Letters, 2014. **104**(10): p. 101913.
56. Filinchuk, Y., et al., *In Situ Diffraction Study of Catalytic Hydrogenation of VO2: Stable Phases and Origins of Metallicity.* Journal of the American Chemical Society, 2014. **136**(22): p. 8100-8109.
57. Bergmann, G., *Weak localization in thin films: a time-of-flight experiment with conduction electrons.* Physics Reports, 1984. **107**(1): p. 1-58.
58. Aharonov, Y. and D. Bohm, *Significance of Electromagnetic Potentials in the Quantum Theory.* Physical Review, 1959. **115**(3): p. 485-491.
59. Ioffe, A. and A. Regel, *Non-crystalline, amorphous and liquid electronic semiconductors.* Prog. Semicond, 1960. **4**: p. 237-291.
60. Mott, N., *Conduction in non-crystalline systems IX. the minimum metallic conductivity.* Philosophical Magazine, 1972. **26**(4): p. 1015-1026.
61. Qazilbash, M.M., et al., *Correlated metallic state of vanadium dioxide.* Physical Review B, 2006. **74**(20): p. 205118.
62. Tyler, A., et al., *High-temperature resistivity of Sr 2 RuO 4: Bad metallic transport in a good metal.* Physical Review B, 1998. **58**(16): p. R10107.
63. Emery, V.J. and S.A. Kivelson, *Superconductivity in Bad Metals.* Physical Review Letters, 1995. **74**(16): p. 3253-3256.
64. Muraoka, Y. and Z. Hiroi, *Metal–insulator transition of VO2 thin films grown on TiO2 (001) and (110) substrates.* Applied Physics Letters, 2002. **80**(4): p. 583-585.
65. Hikami, S., A.I. Larkin, and Y. Nagaoka, *Spin-Orbit Interaction and Magnetoresistance in the Two Dimensional Random System.* Progress of Theoretical Physics, 1980. **63**(2): p. 707-710.
66. Meikap, A.K., et al., *Low temperature transport properties of thin disordered vanadium oxide films.* Journal of Low Temperature Physics, 1991. **85**(3-4): p. 295-309.
67. Lin, J.J. and N. Giordano, *Localization and electron-electron interaction effects in thin Au-Pd films and wires.* Physical Review B, 1987. **35**(2): p. 545-556.
68. Ruzmetov, D., et al., *Hall carrier density and magnetoresistance measurements in thin-film vanadium dioxide across the metal-insulator transition.* Physical Review B, 2009. **79**(15): p. 153107.
69. Kun Huang, X.X., *Semiconductor Physics.* Science Publisher, Beijing, 1958.